Search for the $p_{1/2^-}$ Resonance in ^{7}He with the ^{7}Li(d,^{2}He) Reaction and Measurement of the Deuteron Electrodisintegration under 180° at the S-DALINAC

Vom Fachbereich Physik
der Technischen Universität Darmstadt

zur Erlangung des Grades
eines Doktors der Naturwissenschaften
(Dr. rer. nat.)

genehmigte

Dissertation

angefertigt von

Natalya Ryezayeva
aus Polyarny (Russland)

Juli 2006

Darmstadt
D 17

Referent:	Professor Dr. rer. nat. Dr. h.c. mult. A. Richter
Korreferent:	Professor Dr. rer. nat. J. Wambach
Tag der Einreichung:	18.07.2006
Tag der Prüfung:	06.11.2006

Zusammenfassung

Die vorliegende Arbeit enthält zwei Teile. Beide beschäftigen sich mit der Untersuchung von leichten Kernen.

Im ersten Teil wird die Struktur des exotischen Kerns ^{7}He studiert. Jüngste Experimente geben widersprechende Aussagen über die mögliche Existenz des $p_{1/2}$-Spin-Bahnpartners des ^{7}He Grundzustands mit einem dominanten $p_{3/2}$- Einteilchen-Charakter. Zur Klärung dieser Frage wurde die Reaktion ^{7}Li(d,^{2}He)^{7}He bei einer Einschussenergie von 171 MeV am Kernfysisch Versneller Insituut (KVI) in Groningen untersucht. Das Experiment fand im April 2003 statt. Mit dem experimentellen Aufbau am KVI wurde eine Energieauflösung von $\Delta E \approx 150$ keV in den gemessenen Spektren erreicht, die geringer ist als die natürliche Linienbreite des ^{7}He-Grundzustands. Das ungebundene ^{2}He-System wurde identifiziert durch die Koinzidenzmessungen der beiden Protonen mit kleiner relativer Energie. Die Messungen erstrecken sich über einen Winkelbereich von $\Theta_{cm} = 0°$ - $11.3°$. Für die Entfaltung des Spektrums wurden bekannte Resonanzen, das Aufbruchverhalten von ^{7}He und quasifreie Ladungsaustauschbeiträge verwendet, unter Berücksichtigung der Cluster-Struktur von ^{7}Li. Dabei weisen die experimentellen Ergebnisse auf eine mögliche niedrigliegende Resonanz bei $E_{\mathrm{x}} = (1.45^{+0.7}_{-0.5})$ MeV mit einer Breite $\Gamma = (2.0^{+1.0}_{-1.1})$ MeV hin. Die Gamow-Teller Stärke für die Übergänge zu den niedrigsten Zuständen in ^{7}He stimmen mit theoretischen Vorhersagen eines *ab initio* Quantum Monte-Carlo Modells überein. Weiterhin wurde der spektroskopische Faktor $S_n = 0.64 \pm 0.09$ des ^{7}He Grundzustands (^{7}He = ^{6}He$\otimes$n) mit einer R-matrix Analyse extrahiert.

In dem zweiten Teil der Arbeit wird der Deuteronaufbruch in der ^{2}H(e,e$'$) Reaktion unter einem Streuwinkel $\Theta = 180°$ untersucht. Die Messungen wurden am supraleitendem Darmstädter Elektronenlinearbeschleuniger S-DALINAC bei Einschussenergien E_0 von 27.8 MeV und 74 MeV im März und April 2006 durchgeführt. Bei niedrigen Impulsüberträgen ($q = 0.28$ fm^{-1} bzw. 0.73 fm^{-1}) dominieren magnetische Übergänge den Aufbruchwirkungsquerschnitt. Daher kann man aus den gemessenen Wirkungsquerschnitten an der Aufbruchschwelle die Wirkungsquerschnitte für den Einfangprozess $np \longrightarrow d\gamma$ extrahieren unter Verwendung des *Prinzips des detaillierten Gleichgewichtes*. Die genaue Information über diesen Prozess ist von großem Interesse für die Big-Bang Nukleosynthese

(BBN). Die experimentellen Daten sind in guter Übereinstimmung mit theoretischen Vorhersagen unter Verwendung eines Nukleon-Nukleon Potentials (Bonn-B) und unter Einschluss von Mesonaustausch-Ströme und Isobarkonfigurationen.

Summary

The present work contains two parts, both devoted to the investigation of light nuclei.

In the first part of the thesis the structure of the exotic ^{7}He nucleus is studied. The disappearance of the usual magic numbers in extremely neutron-rich nuclei implies a considerable modification in the spin-orbit interaction. Recent experiments yield contradictory results about a possible existence of the $p_{1/2^-}$-spin-orbit partner of the ^{7}He ground state with a dominant $p_{3/2^-}$ single-particle character. In order to clarify this question a study of the ^{7}Li(d,^{2}He)^{7}He reaction has been performed using a 171 MeV deuteron beam provided by the cyclotron at Kernfysisch Versneller Insituut (KVI) in Groningen. The experiment was carried out in April 2003. The setup at KVI offers a resolution $\Delta E \approx 150$ keV (FWHM) in the measured spectra, better than the line width of the ground state of ^{7}He. The unbound ^{2}He system was identified by detecting coincidences between two protons with small relative energy. The data were taken over the angular range $\Theta_{cm} = 0° - 11.3°$. A possible resonance at an excitation energy $E_{\mathrm{x}} = (1.45^{+0.7}_{-0.5})$ MeV with a width $\Gamma = (2.0^{+1.0}_{-1.1})$ MeV is suggested by a decomposition of the spectrum using known resonances, the breakup behaviour of ^{7}He and quasifree charge-exchange contributions, taking into account the cluster structure of ^{7}Li. Gamow-Teller strengths for transitions to the lowest states in ^{7}He are in remarkable agreement with results from *ab initio* Quantum Monte Carlo calculations. The neutron spectroscopic factor $S_n = 0.64 \pm 0.09$ of the ^{7}He ground state (^{7}He $=$ ^{6}He$\otimes$n) is extracted by an R-matrix analysis.

In the second part of the thesis the deuteron breakup has been studied in the ^{2}H(e,e$'$) reaction at $\Theta = 180°$. The present measurements were performed in March and April 2006 at the superconducting Darmstadt electron linear accelerator S-DALINAC at an incident electron energy $E_0 = 27.8$ MeV and 74 MeV. At low momentum transfer ($q = 0.28$ fm^{-1} and 0.73 fm^{-1}, respectively) magnetic transitions are expected to give the dominant contributions to the breakup cross sections. Thus, the measured deuteron-electrodisintegration cross section at threshold can be used to obtain the cross section for the $np \longrightarrow d\gamma$ reaction applying the *principle of detailed balance*. The accurate information about this process is of great interest in nuclear astrophysics, specifically with regard to Big-Bang nucleosynthesis. The experimental data are in excellent agreement with theoretical calculations based on a nucleon-nucleon potential model (Bonn-B), under the inclusion of meson-exchange and isobar effects.

Contents

PART I:
Search for the $p_{1/2^-}$ Resonance in ^{7}He with the ^{7}Li(d,^{2}He) Reaction

1 Introduction

In recent years the study of the structure and the reaction mechanisms involving light exotic nuclei has lead to the development of new theoretical models based on *ab initio* methods [1,2] and also on refined operator methods like unitary correlation operator method UCOM [3]. Due to novel experimental techniques and the rapid progress in the production of radioactive beams various unexpected phenomena have been observed at the drip lines which can not be explained within the traditional models used for stable nuclei. As an example, nuclear halo states have been found in a number of light nuclei close to the nucleon drip lines. In simple words, nuclear haloes are clouds of nucleons extending well beyond the surface of a bound core with protons and neutrons. But there is no precise definition when a nuclear state should be called a halo state. For example, the matter radius for such systems should be significantly larger than the standard nuclear radius, and a halo system should divide into clusters that have a larger distance from each other than in usual nuclei. The pairing is very important in loosely bound systems. This is most remarkably seen in the helium isotopes. Adding one neutron to ^{4}He yields ^{5}He which is unbound. However, adding two neutrons to the ^{4}He ^{6}He will be formed which is a bound, two neutron halo nucleus. Continuation towards the neutron dripline, the story repeats itself with ^{7}He and ^{8}He. Continuing even further ^{9}He is reached and the doubly magic nucleus ^{10}He. Thus, thorough investigations of the neutron-rich He isotopes have demonstrated their dominant α - cluster structure [4], leading to a two-neutron halo in ^{6}He and a peculiar 4n + α structure in ^{8}He while the odd-mass isotopes ^{5,7}He are particle-unbound. Still many open questions regarding the structure of the unstable proton and neutron rich nuclei have to be answered [5]. The investigations, that are presented in this

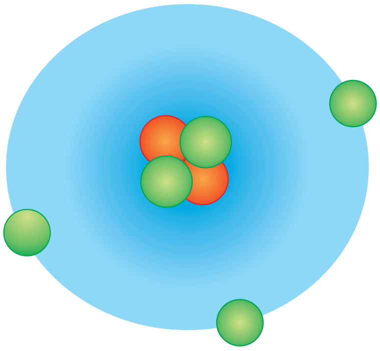

Fig. 1.1: Simplified view of the ^{7}He halo nucleus consisting of two protons (dark) and five neutrons (light grey).

work, focus on the experimental study of the unbound ^{7}He system. A simplified view of the ^{7}He nucleus can be seen in Fig. 1.1.

The main reason for investigating ^{7}He has been a recent very interesting observation which was reported by Meister *et al* [6]. In this work a $J^\pi = 1/2^-$ resonance at excitation energy $E_\mathrm{x} = 0.56(10)$ MeV with a width $\Gamma = 0.75(8)$ MeV was observed. This state, assumed to be the spin-orbit partner of the ^{7}He ground state, was populated in a ^{8}He breakup reaction on a ^{12}C target at 227 MeV/nucleon. Such a low value for the spin-orbit splitting is at variance with typical values of 5 - 6 MeV observed in heavier nuclei like ^{15}O, ^{17}O or ^{39}Ca. Even in case of ^{5}He, the spin-orbit splitting is believed to be significantly larger at around 4 MeV. The strength of the spin-orbit force is measured by the energy splitting of spin-orbit partners. For halo-nuclei in general little is known about the spin-orbit splitting, except that one could argue that the large radial extent of the excess nucleons might significantly reduce the spin-orbit interaction ($V_{s.o.} \sim \frac{1}{r}\frac{\partial V(r)}{\partial r}$). The observation of the spin-orbit partner in ^{7}He could thus shed light upon the spin-orbit interaction in neutron-halo nuclei with important consequences for the understanding of their structure.

The ^{7}He nucleus has been studied in various experiments. The ground state (g.s.) is fairly well known and was for the first time observed by Stokes and Young in 1967 in a (t,^{3}He) reaction [7]. This is a comparatively long-lived resonance with a total width $\Gamma \approx 160$ keV which is situated at about 440 keV above the (^{6}He + n) threshold. It was more than 30 years later when an excited state was found in this exotic nucleus. The state was observed in the p(^{8}He,d)^{7}He reaction by

Korsheninnikov *et al.* [8] at $E_{\mathrm{x}} = 2.9$ MeV with a width of $\Gamma = 1.9$ MeV. It was also found that it predominantly decays to the first excited state of ^{6}He ($J^\pi = 2^+$). This led to a spin assignment of $J^\pi = 5/2^-$ for the new resonance. Another broad state at $E_{\mathrm{x}} = 2.9$ MeV and evidence for a further resonance at 5.8 MeV excitation energy with a large width between 3 and 5 MeV were found in [9]. The work of Meister *et al.* [6] prompted a number of new measurements. Studies of the ^{7}He structure through the neutron-transfer reaction d(^{6}He,p)^{7}He [10] contradict the finding of Ref. [6]. No resonances except the ground state have been seen in the excitation energy region up to 8 MeV. Moreover, in recent experiment [11, 12] investigating isobaric analog states of the ^{7}He in ^{7}Li through the p(^{6}He,n) compound nucleus reaction no evidence for a low-lying $1/2^-$ resonance was found. The authors suggest a broad $1/2^-$ state above $E_{\mathrm{x}} \approx 2.3$ MeV in ^{7}He, the highest energy accessible in their experiment. However, based on continuum shell-model calculations it has been pointed out [13] that the resonance with the parameters of Ref. [6] would not be detectable in the particular kinematics chosen in Ref. [12]. On the other hand, in a rather recent work [14] the results of the p(^{8}He,d)^{7}He experiment also indicated the low-lying excited state with parameters $E_{\mathrm{x}} = 0.9 \pm 0.5$ MeV, $\Gamma = 1.0 \pm 0.9$ MeV. Finally, the recent d(^{6}He,p)^{7}He experiment performed at Argonne National Laboratory [15] is not consistent with the result of Meister *et al.* [6] since it suggests a broad resonance structure between 2 and 3 MeV excitation energy with $\Gamma = 2$ MeV, which could correspond to a $1/2^-$ state.

The present work provides an alternative access to this important question by utilizing the ^{7}Li(d,^{2}He)^{7}He charge-exchange reaction at zero degrees, where Gamow-Teller (GT) transitions are selectively excited. This reaction at intermediate energies has been developed recently as a high-resolution spectroscopic tool for the study of GT strength distributions [16]. Like the ^{7}He ground state, the $J^\pi = 3/2^-$ g.s. of the ^{7}Li is also interpreted as $1p_{3/2}$ single-particle state. Gamow-Teller transitions populating spin-orbit partners - like the $1p_{3/2}$ and $1p_{1/2}$ state - should have similar strengths. This is also predicted by Green's Function Monte Carlo (GFMC) calculations. Since the g.s. is sufficiently populated in a charge-exchange reaction [7], a low-lying resonance in ^{7}He with parameters from Ref. [6] should give a clear signal. The unbound diproton system is referred to as ^{2}He, if the two protons couple to an $^1S_0$, $T = 1$ state. Thus, because of the quantum numbers of the initial and final particles (d and ^{2}He, respectively), the (d,^{2}He) reaction induces exclusively pure spin-isospin excitations. Experimentally, the $^1S_0$ state is selected by limiting the relative energy of the two-proton system to 1 MeV in their detection.

The measurement of the (d,^{2}He) reaction requires the coincident detection of the outgoing protons with small opening angle, close to the direction of the incident deuteron. In this case the use of a magnetic spectrometer with a large momentum-acceptance and with a detector system capable of simultaneously detecting both protons is needed. With this type of setup a rather high resolution can be achieved. However, the difficulty of such measurements resides in the capability of the detection system to suppress the tremendous random background due to the breakup of the deuteron on the target and its ability to filter out the valid ^{2}He events. The (d,^{2}He) probe is of pure spin-flip nature and even more selective than (n,p) and (t,^{3}He) reactions, where non-spin-flip transitions can compete.

The Part I of this thesis is organized in the following way. In Chapter 2 some of the theoretical tools used for the interpretation of the present data are introduced. Chapter 3 is devoted to the description of the experimental setup and procedure. Chapter 4 deals with the analysis methods to extract observables from the measured quantities. The extraction of the Gamow-Teller strength for low-lying states in ^{7}He is discussed in Chapter 5. Chapter 6 gives the results of an R-matrix analysis that yields the spectroscopic factor of the ^{7}He ground state. Chapter 7 presents a short discussion about the higher-lying structure in the ^{7}He nucleus. A summary and outlook given in Chapter 8 conclude the first part. Main results of the present part are published in [17, 18].

2 Theoretical background

The following sections present the basic concepts for the theoretical calculations performed in this thesis. After a general approach towards the scattering formalism, the distorted wave description of nucleon-nucleus scattering is presented, which is then used for the calculations of the angular distributions. A more complete account of scattering theory and of the Distorted Wave Born Approximation (DWBA) can be found in [19–21]. Section 2.4 deals with a short introduction to the shell model. The one-body transition densities calculated within the shell model code can be used for the DWBA calculations. Chapter 2.6 gives an overview of the Quantum Monte Carlo (QMC) model. The GT strengths obtained from the experimental data can be compared with *ab initio* QMC calculations. The description of the QMC model was extracted from the original papers [22–26].

2.1 Scattering formalism

The scattering of a particle from a potential $V(r)$ is described by the time-independent Schrödinger equation

$$(H - E)\,\psi(\vec{k}, \vec{r}) = 0, \tag{2.1}$$

where the Hamiltonian H can be divided into two parts

$$H = H_0 + V. \tag{2.2}$$

The first part H_0, describes the unperturbed motion of the system and the second, V, the interaction, which disappears for sufficiently large separation of the interacting particles of the system. The energy in the center-of-mass system is denoted by E. The particle is represented by a wave function ψ that has to be a solution of equation (2.1). The solution has to be found with the boundary condition that the total wave function must have the asymptotic behavior of an incoming plane wave and an outgoing spherical wave

$$\psi(\vec{k},\vec{r}) \longrightarrow \phi + f(\Theta)\frac{e^{ikr}}{r}, \tag{2.3}$$

where r is the relative distance between the particles in the entrance channel, k is the wave vector, ϕ is a plane wave and $f(\Theta)$ is the scattering amplitude which is connected to the differential cross sections by

$$\frac{d\sigma}{d\Omega}(\Theta) = |f(\Theta)|^2. \tag{2.4}$$

The Schrödinger equation (2.1) can also be expressed in integral form. In this case the formal solution is usually called the Lippmann-Schwinger equation and can be represented as

$$\Psi^{(\pm)} = \Phi + G_0^{\pm} V \Psi^{\pm}, \tag{2.5}$$

or in Dirac notation

$$|\psi^{\pm}\rangle = |\phi\rangle + G_0^{\pm} V |\psi^{\pm}\rangle, \tag{2.6}$$

where the G_0 is the Green's function of the unperturbed equation

$$G_0^{\pm} = \frac{1}{E - H_0 \pm i\varepsilon}. \tag{2.7}$$

Thus, rewriting (2.5) using the relation (2.7) for the Green function one gets

$$\Psi^{(\pm)} = \Phi + \frac{1}{E - H_0 \pm i\varepsilon} V \Psi^{\pm}. \tag{2.8}$$

In general the Lippmann-Schwinger equation has two solutions. The first consists of a plane wave and an outgoing scattered wave and is usually indicated with a '+'. The second solution is a plane wave plus an ingoing scattered wave denoted with a '−'. The Green's function operator G_0 can be used to define the T transition operator as

$$T^{\pm} = V + V G_0^{\pm} T^{\pm}, \tag{2.9}$$

with the transition matrix element

$$T_{fi} = \langle\phi|T^{+}|\phi\rangle = \langle\phi|V|\psi^{+}\rangle, \tag{2.10}$$

where i and f are used to label the initial and final scattering wave functions. The state vector $|\psi^{\pm}\rangle$ in (2.6) and the T matrix operator in (2.9) can be seen as a series expansion in V. Their iterated forms are

$$|\psi^{\pm}\rangle = |\phi\rangle + G_0^{\pm}V|\phi\rangle + G_0^{\pm}VG_0^{\pm}V|\phi\rangle + ... \tag{2.11}$$

and

$$T^{\pm} = V + VG_0^{\pm}T^{\pm} + VG_0^{\pm}VG_0^{\pm}V + ..., \tag{2.12}$$

respectively. The two series can be approximated by taking only the first n terms into account, which is called Born approximation to n^{th} order. In the second series $G_0^{\pm}$ propagates the particle from scattering to scattering point. Taking only the first n terms into account, one limits the nuclear reaction to a n-step scattering process. The matrix element T_{fi} defined in (2.10) can be related to the scattering amplitude

$$f(\Theta) = -\frac{\mu}{2\pi\hbar^2}T_{fi} \tag{2.13}$$

with μ being the reduced mass of the system.

2.2 Distorted wave Born approximation and optical potential

For the treatment of the charge-exchange reaction the Distorted Wave Born Approximation is used. This takes into account the elastic scattering of the incident particles before the reaction, and of the emergent particles afterwards [27,28]. To treat the scattering process in DWBA, the potential V is usually split into two parts

$$V = U + W. \tag{2.14}$$

The optical potential U describes the elastic scattering and is responsible for the distortion of the incoming and outgoing waves. The potential W contains the residual interaction and accounts for the inelasticity. The scattering problem with the potential U alone has a known solution χ which fulfils the equation

$$(H_0 + U)\chi^{\pm} = E\chi^{\pm}. \tag{2.15}$$

Thus, replacing the plane wave in equation (2.6) by the distorted wave one can express the wave state vector $|\psi^{\pm}\rangle$ in terms of the wave functions $|\chi^{\pm}\rangle$

$$|\psi^{\pm}_{DW}\rangle = |\chi^{\pm}\rangle + G^{\pm}_{U} W |\psi^{\pm}_{DW}\rangle, \tag{2.16}$$

where $G^{\pm}_{U}$ belongs to the Hamiltonian $H_U = H_0 + U$. Applying equations (2.11) and (2.12) the transition matrix element can be than written as

$$T_{fi} = \langle \phi | U | \chi^{+} \rangle + \langle \chi^{-} | W | \psi^{+} \rangle, \tag{2.17}$$

where i and f are used to label the initial and final scattering wave functions, respectively. In the DWBA the state vector $|\psi^{+}\rangle$ is replaced by the distorted wave state vector $|\psi^{+}_{DW}\rangle$ defined in (2.16) and is approximated to the first order in the series expansion. This allows to calculate the transition matrix in DWBA as

$$T^{fi}_{DWBA}(post) = \langle \chi^{-} | W | \psi^{+}_{DWBA} \rangle. \tag{2.18}$$

The form of the transition matrix derived in (2.18) is called *post* representation. The *prior* representation of the transition matrix, which is derived from the time-reversed reaction, can be calculated to be

$$T^{fi}_{DWBA}(prior) = \langle \psi^{-}_{DWBA} | W | \chi^{+} \rangle. \tag{2.19}$$

It can be shown that the *post* and the *prior* form are identical

$$T^{fi}_{DWBA} = \langle \chi^{-} | W | \psi^{+}_{DWBA} \rangle = \langle \psi^{-}_{DWBA} | W | \chi^{+} \rangle. \tag{2.20}$$

The distorted waves $\chi^{\pm}$ are obtained from solving the Schrödinger equation (2.15) with the optical potential U from the relation (2.14). The conventional form of this potential contains real and imaginary parts of central and spin-orbit type. In analogy with optics the real part of the potential describes the scattering in the dispersive medium, while the imaginary part corresponds to the absorption. The standard form of the optical potential is parameterized as

$$\begin{aligned} V(r) &= -V_R f(r, r_0, a_0) + i4a_I W_D \frac{d}{dr} f(r, r_I, a_I) - iW_S f(r, r_I, a_I) \quad (2.21) \\ &+ V_{LS} \left(\frac{\hbar}{m_\pi c} \right)^2 (\vec{L} \cdot \vec{S}) \frac{1}{r} \frac{d}{dr} f(r, r_{LS}, a_{LS}) + V_{Coul}. \end{aligned}$$

Usually for the description of the real part of the potential the Woods-Saxon shape for the central term V_R and the Thomas form for the spin-orbit term V_{LS} is chosen. The imaginary part is split into two parts named volume and surface, where the volume term W_S has the Woods-Saxon form and the surface term W_D is described by the derivative of the Woods-Saxon form. The radial form factors of Woods-Saxon type in equation (2.21) can be written as

$$f(r, r_x, a_x) = \frac{1}{1 + \exp((r - r_x A^{1/3})/a_x)} \quad (2.22)$$

with radius r, diffuseness a and $x = 0, I, LS$. The Coulomb potential V_{Coul} is assumed to be the potential generated by a uniformly charged sphere of radius $r_c A^{1/3}$, where A is the mass number of the nucleus.

Ordinary DWBA calculations may give rise to ambiguities in the interpretation of the experimental differential cross sections for the A(d,^{2}He)B reaction, where A is the target and B is the residual nucleus. The ^{2}He system is in reality a pair of protons coupled to the $^1S_0$ state. The disagreement of the theoretical calculations with experimental data can be explained by the fact that the optical potential of two fragments in a three-body channel does not resemble elastic optical potentials obtained in a two-body channel. Furthermore, no phenomenological information is available on the ^{2}He-nucleus interaction.

Instead of treating both, the incident and the exit channel, in DWBA, in the present work, the adiabatic approximation method [29–31] is applied that uses a three-body wave function in the exit channel rather than using an artificial final state distorting interaction between ^{2}He and the final nucleus. The transition amplitude for (d,^{2}He) reaction looks like

$$T^{fi}_{DWBA} = \langle \chi^-_{^2He}(\vec{r}) \psi_{^2He}(\vec{x}_{1-2}) \Psi_f | V | \Psi_i \phi_d \chi^+_d(\vec{r}) \rangle, \quad (2.23)$$

where the projectile and ejectile wave functions of the incident and exit channels are denoted by ϕ_d and $\psi_{^2He}$, the target wave functions by Ψ_i and Ψ_f and the distorted waves by χ_d^+ and $\chi_{^2He}^-$, respectively. The relative coordinate between projectile and target is represented by $\vec{r}$ and the relative distance between two protons by $\vec{x}_{1-2}$. The incident channel wave function is generated using the conventional optical potential whereas the exit channel wave function is treated in the adiabatic approximation. The three-body wave function $|\psi^+\rangle = |\chi_{^2He}^- \psi_{^2He}\rangle$ in the exit channel satisfies the Schrödinger equation

$$\left[-\frac{\hbar^2}{2\mu_{B-12}} \nabla_r^2 + \sum_{i=1,2} V_{iB}(\vec{r}, \vec{x}_{1-2}) + H_{12} - E \right] \psi^+(\vec{k}_{B-12}, \vec{k}_{1-2}; \vec{r}, \vec{x}_{1-2}) = 0, \tag{2.24}$$

with the reduced mass μ_{B-12} in the final state. If the condition $E \gg \epsilon_{pp}$ is fulfilled, where ϵ_{pp} is the relative energy between two protons, the excitation within the 1-2 system ^{2}He can be neglected, i.e. the sub-Hamiltonian H_{12} is replaced by its eigenvalue ϵ_{pp}. This is known as adiabatic or sudden approximation. Similar to common DWBA the interaction V_{iB} of protons $i = 1, 2$ with the residual nucleus B is approximated by an optical potential evaluated at $\frac{1}{2}(E - \epsilon_{pp})$. The DWBA technique adapted to the (d,^{2}He) reaction is used to calculate angular distributions of differential cross sections. The calculations require the definition of the transition, an effective interaction, a deuteron optical potential for the entrance channel and a proton optical potential for the exit channel.

2.3 Effective interaction

In order to calculate the transition matrix element T^{fi}, an effective interaction between the nucleons of the projectile and the target is needed. This effective interaction is, in general, very complicated. It depends on the incident energy and on specific properties of projectile and target. The simplest method for the description of the cross section is based on the impulse approximation (IA) with plane or distorted waves (PWIA/DWIA, respectively). This approach is valid at incident energies above $\sim$ 100 MeV/nucleon and assumes that the interaction takes place between only one nucleon of the projectile and one of the target in a single collision. Furthermore, the effective interaction is assumed to be the free nucleon-nucleon interaction. The effective interaction used in this work is the T-matrix interaction parameterized by Love and Franey [32, 33].

The effective nucleon-nucleon (NN) interaction is a sum of central (C), spin-orbit (LS) and tensor (T) terms and usually has a form

$$V_{ip} = V_{ip}^{C}(r) + V_{ip}^{L}S(r)\vec{L}\cdot\vec{S} + V_{ip}^{T}(r)\vec{S}_{ip}. \tag{2.25}$$

The three parts can be split up again into their spin and isospin dependence

$$V_{ip}^{C}(r) = V_{0}^{C}(r) + V_{\sigma}^{C}(r)\vec{\sigma_i}\cdot\vec{\sigma_p} + V_{\tau}^{C}(r)\vec{\tau_i}\vec{\tau_p} + V_{\sigma\tau}^{C}(r)\vec{\sigma_i}\cdot\vec{\sigma_p}\vec{\tau_i}\cdot\vec{\tau_p}, \tag{2.26}$$

$$V_{ip}^{LS} = V^{LS}(r) + V_{\tau}^{LS}(r)\vec{\tau_i}\cdot\vec{\tau_p}, \tag{2.27}$$

$$V_{ip}^{T} = V^{T}(r) + V_{\tau}^{T}(r)\vec{\tau_i}\cdot\vec{\tau_p}, \tag{2.28}$$

where p is referred to a projectile nucleon and i to a target nucleon, $r = r_{ip}$ is the distance between participating nucleons, and $\vec{S}_{ip}$ is the tensor operator.

For small momentum transfer q and large E_{cm} values the simplest approach to construct an effective NN-interaction can be used, i.e. using the free transition matrix element t_{NN}^{0} as zero-range effective interaction

$$V_{ip} = t_{NN}^{0}(E, q)\delta(\vec{r}_{ip}). \tag{2.29}$$

The NN scattering amplitude is usually expressed in a form

$$M(E_{cm}, \Theta) = A + B\vec{\sigma_i}\cdot\vec{n}\vec{\sigma_p}\cdot\vec{n} + C(\vec{\sigma_i}\cdot\vec{n} + \vec{\sigma_p}\cdot\vec{n}) + E\vec{\sigma_i}\cdot\vec{q}\vec{\sigma_p}\cdot\vec{q} + F\vec{\sigma_i}\cdot\vec{Q}\vec{\sigma_p}\cdot\vec{Q}, \tag{2.30}$$

where the coefficients A,B,C,E, and F are functions of the center-of-mass energy E_{cm}, of the scattering angle Θ, and of the two-body isospin, e.g. $A = A_0 + A_1\vec{\tau_i}\vec{\tau_p}$. The unit vectors $\vec{q}, \vec{Q}, \vec{n}$ can be calculated from

$$\vec{n} = \vec{k}\times\vec{k'}, \qquad \vec{q} = \vec{k} - \vec{k'}, \qquad \vec{Q} = \vec{k} + \vec{k'}. \tag{2.31}$$

An approximation of the effective interaction can be obtained by assuming a local finite-range form of effective nucleon-nucleon interaction. In this case the parameters of V_{ip} have to be adjusted until the NN transition matrix element is reproduced in momentum space [32]

$$t^0_{NN} = \frac{-4\pi(\hbar^2 c)^2}{E_{cm}} M = \int e^{-i\vec{k}\vec{r}} V_{ip}(1 - \vec{P}_{ip}) e^{i\vec{k}\vec{r}} d\vec{r}, \tag{2.32}$$

where the operator $\vec{P}_{ip}$ is the exchange operator which generates antisymmetrization.

Since only the spin-isospin components are involved in the (d,^{2}He) reaction, the interaction from (2.25) is given by

$$V_{ip} = [V^C_{\sigma\tau}(r_{ip})(\vec{\sigma_i} \cdot \vec{\sigma_p}) + V^T_{\sigma\tau}(r_{ip})\vec{S}_{ip}]\vec{\tau_i} \cdot \vec{\tau_p}. \tag{2.33}$$

An explicit representation for the interaction coefficients as a sum of Yukawa terms for the central part and as a sum of $r^2\times$ Yukawa terms for the tensor part is given in [32].

2.4 Shell model and one-body transition densities

The nuclear shell model was discovered in the late 40's and has provided a successful approach to the microscopic description of nuclear structure. For instance, one-body transition densities can be calculated from model wave functions of the nuclear states using shell model codes like OXBASH [34]. The basic assumption of the nuclear shell model is that, to first order, each nucleon moves independently in an average field. Thus, the nuclear interaction can be approximated by an average central potential. Because of the special character of the interaction, namely being a short-range attractive force, and because of the Pauli principle, the shell-model potential is essentially constant at the center of the nucleus and goes quickly to zero at the nuclear surface. An important representation of this behaviour is given by the Woods-Saxon potential

$$V(r) = -V_0 f(r, r_0, a_0) \tag{2.34}$$

where $f(r, r_0, a_0)$ is defined in Eq. (2.22), the well depth V_0 is of the order of 50 MeV. To the nuclear potential $V(r)$ one must add the Coulomb potential $V_{Coul}(r)$ and a spin-orbit part $V_{LS}(r)\vec{L} \cdot \vec{S}$, which is required to give a correct description of the observed shell closures and remove the degeneracy of states with the same orbital angular momentum L. In case of a Woods-Saxon potential the Schrödinger equation has to be solved numerically. Analytic forms of the nuclear wave functions can be obtained by using an easily tractable harmonic-oscillator potential

$$V(r) = -V_0 + m\omega^2 r^2/2 \tag{2.35}$$

and neglecting the spin-orbit force. Here, V_0 is the well depth, m is the mass of a nucleon and ω is the oscillator frequency of the simple harmonic motion of the particle. As r increases, the potential tends to infinity. The energy levels of the harmonic-oscillator potential are given by

$$E_{NL} = [2(N-1) + L + 3/2]\hbar\omega, \tag{2.36}$$

where N is the radial quantum number and L is the orbital angular momentum. The nuclear potential can be written as a sum of the two-body interactions V_{ij} which take place between the nucleons inside the nucleus

$$V = \sum_{i>j}^{A} V_{ij} = \sum_{i}^{A} V_i + \sum_{i>j}^{A} W_{ij}, \tag{2.37}$$

where V_i is the average mean-field potential the i^{th} nucleon feels as a result of the combined force of the rest of the nucleons and W_{ij} represents the residual interactions which can not be incorporated into the average potential. The mean-field potential V_i causes completely independent motion of the nucleons and leads to pure single-particle wave functions. The residual interactions perturb this picture and cause the nuclear wave function to become a superposition of the single-particle states. This situation is known as configuration mixing. Considering Eq. (2.37) the nuclear Hamiltonian becomes

$$H = \sum_{i}^{A} \frac{\hbar^2 p_i^2}{2m} + \sum_{i}^{A} V_i(\vec{r_i}) + \sum_{i>j}^{A} W_{ij}(\mid \vec{r_i} - \vec{r_j} \mid), \tag{2.38}$$

where the first term denotes the kinetic energy of the individual nucleons and the next two terms represent the potential. A schematic view of the ^{7}He nucleus

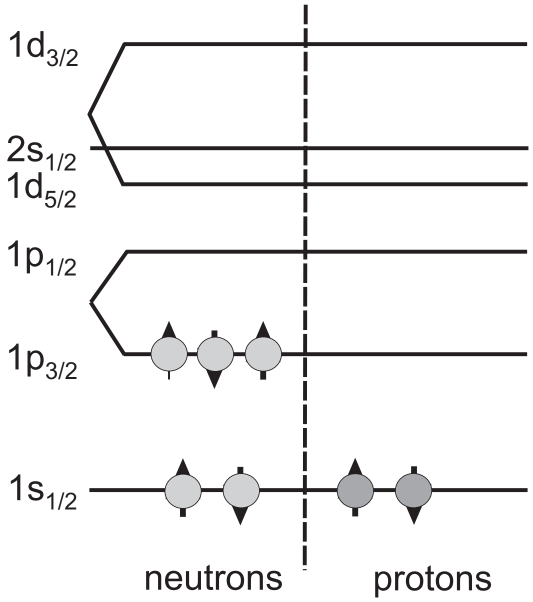

Fig. 2.1: Schematic representation of the ^{7}He nucleus in the shell model.

within the shell model can be seen in Fig. 2.1. When applying the approximation described in previous sections, the scattered particle plays the role of a one-body operator acting on the target nucleons. Thus, any inelastic nuclear transition can be written as a superposition of single-particle transitions taking target nucleons from an orbit j to an orbit $j\,'$ with amplitudes $S_J^{j\,'j}$.

The separation of nuclear-structure interaction contributions to the scattering amplitude is achieved by performing a multipole expansion of the effective interaction in momentum space [35], giving

$$T_{fi} = \frac{2}{\pi} \sum_{\alpha\,\beta JM} (-1)^M \int v_{\beta\alpha}(q,Q) \langle \chi_f | \hat{T}_{LSJ}^{-M(\beta)} | \chi_i \rangle \langle \Phi_{J_f}^{M_f} | \sum_{j=1}^{A} \hat{T}_{LSJ}^{M(\alpha)}(j) | \Phi_{J_i}^{M_i} \rangle q^2 dq \tag{2.39}$$

with parameters Q and q defined in equation (2.31), α and β represent the quantum numbers of the projectile and target, respectively, $v_{\beta\alpha}(q,Q)$ are Bessel transformations of the various parts of the effective interaction and $\hat{T}_{LSJ}^{M(\alpha,\beta)}$ are spherical tensor operators. Using the *Wigner-Eckart theorem* the nuclear matrix element can be written as

$$\langle \Phi_{J_f}^{M_f} | \sum_{j=1}^{A} \hat{T}_{LSJ}^{M}(j) | \Phi_{J_i}^{M_i} \rangle \tag{2.40}$$

$$= (-1)^{J_f - M_f} \begin{pmatrix} J_f & J & J_i \\ -M_f & M & M_i \end{pmatrix} \langle \Phi_{J_f} || \sum_{J=1}^{A} \hat{T}_{LSJ}(j) || \Phi_{J_i} \rangle .$$

The reduced matrix element in equation (2.40) can be expressed as a sum of single-particle matrix elements $\langle j\,' || \hat{T}_{LSJ} || j \rangle$ weighted with so-called one-body transition densities $S_J^{j\,'j}(J_f, J_i)$

$$\langle \Phi_{J_f} || \sum_{J=1}^{A} \hat{T}_{LSJ}(j) || \Phi_{J_i} \rangle = \sum_{j\,'j} S_J^{j\,'j}(J_f, J_i) \langle j\,' || \hat{T}_{LSJ} || j \rangle, \tag{2.41}$$

which are defined as

$$S_J^{j\,'j}(J_f, J_i) = -\frac{1}{\sqrt{2J+1}} \langle \Phi_{J_f} || [\beta^{\dagger}_{j\,'} \tilde{\beta}_j] || \Phi_{J_i} \rangle . \tag{2.42}$$

Here, $\beta^{\dagger}_{j\,'}$ is a creation operator producing a particle with angular momentum $j\,'$ and $\tilde{\beta}_j$ an annihilation operator creating a hole state with angular momentum j.

2.5 Cross sections and Gamow-Teller strength

The differential cross section of a scattering reaction A(a,b)B is connected to the transition matrix element via the following relation [28]

$$\frac{d\sigma}{d\Omega} = \frac{\mu_i \mu_f}{(2\pi\hbar^2)^2} \frac{k_f}{k_i} \frac{1}{2} \hat{J}_A^{-2} \sum_{M_A, M_B, m_a, m_b} |T(M_A, M_B, m_a, m_b)|^2 . \tag{2.43}$$

Here μ_i, μ_f are the reduced masses of the respective particles, $\hat{J} \equiv \sqrt{2J+1}$ is a spin factor and the sum is over the spin projections in the initial and final states respectively. According to the DWBA, the transition matrix element from Eq. (2.20) can be expressed as

$$T_{fi}^{DW} = \int \chi_f^{-*}(\vec{r}, \vec{k}\,') \langle \Phi_f | \sum_{j}^{A} t_{jp} | \Phi_i \rangle \chi_i^{+}(\vec{r}, \vec{k}) d^3 r, \tag{2.44}$$

where the transition operator t_{jp} in the momentum representation is identical to the NN t-matrix (Eq. 2.32) and can be written in the following way

$$t_{ip} = V_{ST}(r_{jp})(1 - \vec{P}_{jp}) \hat{\mathcal{O}}_j(ST) \hat{\mathcal{O}}_p(ST), \tag{2.45}$$

where $\vec{P}_{ip}$ interchanges target nucleon i and projectile, and operators $\hat{\mathcal{O}}$ are defined as

$$\hat{\mathcal{O}}(ST) = \begin{cases} \vec{\sigma}\vec{\tau} \quad S=1, T=1 \quad (GT) \\ \vec{\tau} \quad S=0, T=1 \quad (F). \end{cases} \tag{2.46}$$

The transition matrix is most useful in its momentum representation

$$T^{DW}_{fi} = \int t(q)\rho_{ST}(q)D(q,k,k\,')d^3q. \tag{2.47}$$

Here $t(q)$ is the Fourier transform of the interaction, $\rho_{ST}(q)$ is the transition density and D is the distortion factor

$$t(q) = 4\pi \int V(r)[j_0(qr) + (-1)^l j_l(kr)]r^2 dr = J_{ST}(q), \tag{2.48}$$

$$\rho_{ST}(q) = \langle \Phi_B | \sum_j^A \hat{\mathcal{O}}_j(ST)e^{i\vec{q}\vec{r}} | \Phi_A \rangle \cdot \langle b | \hat{\mathcal{O}}_a(ST) | a \rangle, \tag{2.49}$$

$$D(q,k,k\,') = \frac{1}{(2\pi)^3} \int \chi_f^{-*}(\vec{r}, \vec{k}\,')\chi^+(\vec{r}, \vec{k})e^{-i\vec{q}\vec{r}}d^3r, \tag{2.50}$$

where J_{ST} is the volume integral of the relevant interaction, l is the angular momentum transfer and j is the modified Bessel function.
The transition density ρ_{ST} reduces to a single term under the assumption that only angular momentum transfer $\Delta l = 0$ is important for small-angle scattering. Under this assumption

$$\begin{aligned} \rho_{ST}(q) &= I_0(q)M_{ST}\sqrt{2J_A+1}\sqrt{2S+1}\sqrt{8} \qquad (2.51) \\ &\times \sum_{M_s} \begin{pmatrix} J_A & J_B & S \\ M_A & -M_B & M_s \end{pmatrix} \begin{pmatrix} J_a & J_b & S \\ m_a & -m_b & M_s \end{pmatrix} (-1)^{J_B - M_a - M_s}, \end{aligned}$$

where, again under the assumption of the small momentum transfer,

$$I_0(q) = \int |R(r)|^2 j_0(qr)r^2 dr \simeq exp(-\frac{1}{6}q^2\langle r^2 \rangle_\rho). \tag{2.52}$$

Here $\langle r^2 \rangle_\rho$ is the mean-square radius of the transition density. The reduced matrix elements M_{ST} correspond to Gamow-Teller and Fermi strengths, respectively:

$$|M_{ST}|^2 = \begin{cases} \frac{1}{2J_A+1}|\langle J_B || \sigma\tau^{\pm} || J_A \rangle|^2 = B(GT) \quad S=1 \\ \frac{1}{2J_A+1}|\langle J_B || \tau^{\pm} || J_A \rangle|^2 = B(F) \quad S=0 \end{cases} \tag{2.53}$$

Using the *eikonal approximation* for the distorted waves an approximation for the distortion factor D can be obtained

$$\begin{aligned} D(q,k,k') &\simeq \exp\frac{1}{2}[-xA^{1/3}+p(\omega)]\delta(|\vec{k}'-\vec{k}|-\vec{q})e^{i\phi} \\ &= \sqrt{N_D}\delta(|\vec{k}'-\vec{k}|-\vec{q}). \end{aligned} \tag{2.54}$$

Here $p(\omega)$ is a second-order polynomial and $\omega = E_x - Q$ is the energy loss, ϕ and x come from the real and imaginary part of the optical potential, respectively. Inserting Eqs. (2.48) - (2.54) into the Eq. (2.47) and performing the integration, for $q = 0$ one can obtain a simple form of the transition matrix element [36]

$$\begin{aligned} |T_{fi}|^2(q=0) &= N_D B(ST)|J_{ST}|^2(2J_A+1)(2S+1) \\ &\times \left|\sum_{M_s}\begin{pmatrix} J_A & J_B & S \\ M_A & -M_B & M_s \end{pmatrix}\begin{pmatrix} J_a & J_b & S \\ m_a & -m_b & M_s \end{pmatrix}(-1)^{J_B-M_a-M_s}\right|^2. \end{aligned} \tag{2.55}$$

The relation between the cross section and the Gamow-Teller strength can be seen in the expression (2.43). Summation over projections of spin ($j_a = j_b = 1/2$), for a (n,p)- or (p,n)- reaction, provides the result [37]

$$\frac{d\sigma(q=0)}{d\Omega} = \left(\frac{\mu}{\pi\hbar^2}\right)^2 \frac{k_f}{k_i} N_D J_{\sigma\tau}^2 B(GT), \tag{2.56}$$

which is also a good approximation for the (d,^{2}He) reaction.

2.6 *Ab initio* Quantum Monte Carlo method

Since the standard shell model fails to describe many of the essential features of light exotic nucleus ^{7}He, the experimental results discussed in this thesis are compared with those from the *ab initio* Quantum Monte Carlo model. In the last decade, the QMC method has been developed into a powerful tool for description of light nuclei (up to A = 12) using realistic two-nucleon (NN) and three-nucleon (NNN) potentials. It gives precise spectroscopic information like radii, excitation energies, moments, transition strengths, binding energies, *etc.* The quantum Monte Carlo methods consist of variational Monte Carlo (VMC) and Green's function Monte Carlo (GFMC) methods. The VMC is an approximate method that is used as a starting point for the more accurate GFMC calculations. The GFMC method starts from the trial function, which is obtained by the VMC, and makes a Euclidean propagation that converges to the lowest energy for the investigated nuclear state with given quantum numbers J^π and T.

The Hamiltonian used in the calculations includes a nonrelativistic one-body kinetic energy K_i, the Argonne v_{18} two-nucleon potential [38] and the Urbana IX three-nucleon potential [39],

$$H = \sum_i K_i + \sum_{i<j} v_{ij} + \sum_{i<j<k} V_{ijk}. \tag{2.57}$$

The two-nucleon potential v_{ij} can be written as a sum of electromagnetic and one-pion exchange terms and a shorter-range phenomenological part [1]. The Urbana potential V_{ijk} is presented as a sum of two-pion-exchange and shorter-range phenomenological terms.

The variational method (VMC) can be used to obtain approximate solutions to the many-body Schrödinger equation for different nuclear systems. The method finds an upper bound, E_T, to an eigenenergy of H by evaluating the expectation value of H in a trial wave function Ψ_T. The parameters in Ψ_T are varied to minimize E_T, and the lowest value is taken as the approximate energy. A good variational trial function is defined as

$$|\Psi_T\rangle = \left[1 + \sum_{i<j<k} \hat{U}^{TNI}_{ijk}\right] \left[S \prod_{i<j} (1 + \hat{U}_{ij})\right] |\Psi_J\rangle. \tag{2.58}$$

Here $\hat{U}_{ij}$ and $\hat{U}^{TNI}_{ijk}$ are non-commuting two- and three-nucleon correlation operators, S is the symmetrization operator and the Ψ_J is the totally antisymmetric *Jastrow function* which determines the quantum numbers of the nuclear state being investigated. The correlation operator $\hat{U}_{ij}$ includes spin, isospin, and tensor terms induced by the two-nucleon potential, while $\hat{U}^{TNI}_{ijk}$ reflects the structure of the dominant parts of the three-nucleon interaction.

By using the GFMC method [40], one is able to determine binding energies and energies of low-lying excited states. In other words, the aim of the GFMC is to project out the exact lowest energy state, $|\Psi_0\rangle = \lim_{\tau\to\infty}\exp[-(H - E_0)\tau]|\Psi_T\rangle$, where τ is the imaginary time. The $|\Psi_0\rangle$ is associated with a chosen set of quantum numbers from the approximation $|\Psi_T\rangle$ given by Eq. (2.58). The eigenvalue

E_0 is calculated exactly while other expectation values are generally estimated neglecting terms of order $||\Psi_0\rangle - |\Psi_T\rangle|^2$ and higher. In contrast, the error in the variational energy is of order $||\Psi_0\rangle - |\Psi_T\rangle|^2$, and other expectation values calculated with $|\Psi_T\rangle$ have errors of order $||\Psi_0\rangle - |\Psi_T\rangle|$.

2.7 *R*-matrix theory

R-matrix theory [41] is one of the essential tools for reliable interpretation of nuclear reaction and scattering data. It is particularly important for the extraction of the resonance parameters of an investigated state. For instance, one can experimentally obtain the observed reduced width which is the decisive quantity for the determination of the spectroscopic factor. Spectroscopic factors are basic quantities characterizing the single-particle nature of nuclear excitations and therefore serve as an important test of wave functions calculated with recently developed *ab initio* methods. It can also be compared to the classical nuclear shell-model calculations. Using the (d,^{2}He) reaction with good energy resolution for a study of the structure of ^{7}He one gets new information about the g.s. resonance parameters and then in the frame of an R-matrix analysis one can obtain the neutron spectroscopic factor, assuming that the $J^\pi = 3/2^-$ ground state of ^{7}He might be described as a $^6\mathrm{He}\otimes\nu 1\mathrm{p}_{3/2}$ configuration. The neutron spectroscopic factor S_n is defined as

$$S_n = \frac{\gamma^2_{obs}}{\gamma^2_{sp}} \tag{2.59}$$

with γ^2_{obs} and γ^2_{sp} being the observed and single-particle reduced widths, respectively, where the former is provided by the resonance fit while the latter can be computed using a Woods-Saxon single-particle potential.

For description of the unstable $p_{3/2}$ single-particle ground state in ^{7}He a Woods-Saxon single-particle potential with spin-orbit interaction is used. The parameters are chosen to give an optimal fit to the experimentally known nuclear data in the ^{6}He-^{7}He mass region, such as matter and charge radii of ^{6}He, energy of the decaying ^{7}He ground state. The choice of a Woods-Saxon shape was inspired by the potential used by [42] for the reproduction of the experimental p-resonance

states in ^{5}He. The potential has been already defined in Eq. (2.34). The explicit form used here is:
central part

$$U(r) = -V_c/\exp(x(r)+1) \tag{2.60}$$

spin-orbit part

$$U_{ls} = V_{ls}\frac{d}{dr}\left[\frac{1}{\exp(x(r)+1)}\right][j(j+1) - l(l+1) - 3/4]/2 \tag{2.61}$$

and the centrifugal part

$$U_{cen}(r) = \frac{\hbar^2}{2m_{red}}l(l+1)/r^2 \tag{2.62}$$

with parameters for ^{7}He: $V_c = 28.13$ MeV; $V_{ls} = 12.22$ MeV fm; $x(r) = (r - R_c)/a$ where $R_c = 2.79$ fm and $a = 0.25$ fm; $m_{red}c^2 = 804.786$ MeV. The ground state energy resulting with these data is $E(p_{3/2}) = 0.446$ MeV which coincides with the experimental value of 0.445 MeV.

For the ^{6}He bound states E_s = -26.52 MeV and $E(p_{3/2})$ = -1.87 MeV. The depth of the central part is adopted to reproduce these values. This results in the matter rms radius $r_m = 2.64$ fm and the charge radius $r_{ch} = 2.01$ fm (the experimental value is 2.05 fm [43]). With the potential chosen the decaying ground state of ^{7}He is obtained as solution of the central part of the Schrödinger equation with the boundary condition of a purely outgoing wave at a radius R which is well outside the range of the potential $U(r)$. As long as this condition is fulfilled the result does not depend on a specific choice of R. From the solution follows the complex eigenvalue

$$E_{gs} = E_{real} - \frac{i}{2}\Gamma_{gs} \tag{2.63}$$

with $E_{real} = 0.446$ MeV and $\Gamma_{gs} = 0.258$ MeV.

The reduced single-particle width γ^2_{sp} depends on the choice of a matching radius r_{match}. According to R-matrix theory this is the channel radius at which the motion from inside the potential turns over into the free relative motion of the decaying particles. An indication for this is the matching of the logarithmic derivative of the potential motion with that of a free outgoing wave. In Fig. 2.2 the real part of the logarithmic derivatives Re$[f_l(r)]$ for both potential motion and a free outgoing wave is presented leading to an optimum value $r_{match} = 4.0$ fm.

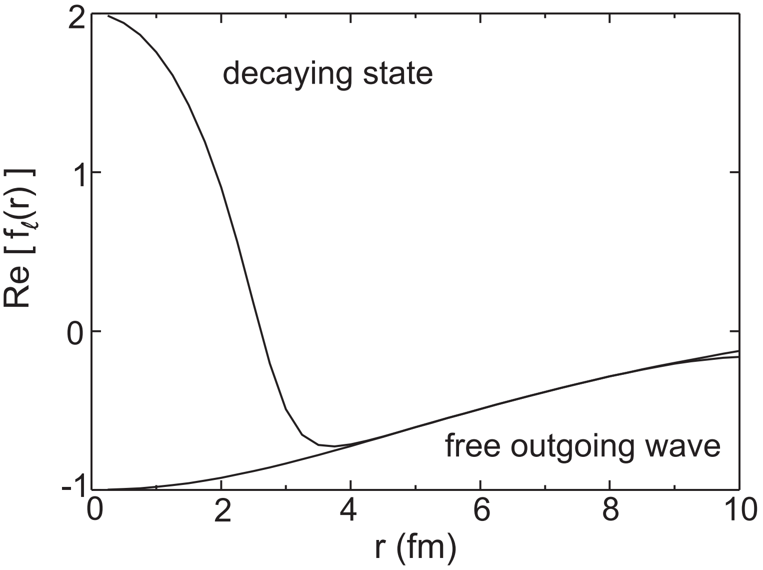

Fig. 2.2: Logarithmic derivatives of the potential motion of the ^{7}He g.s. and that of the free outgoing wave.

To determine the observed reduced width γ_{obs}^2 in (2.59), R-matrix theory in one-level approximation has been used [41]. For the neutron decay channel of ^{7}He the decay cross section is given by

$$\sigma_{c'c}(E) = \frac{\Gamma_{c'}\Gamma_c(E)}{\left[E - E_c + \Delta(E)\right]^2 + \frac{1}{4}\Gamma_c(E)^2} \ . \tag{2.64}$$

Here, c', c are channel numbers, $\Gamma_{c'}$ is the strength of the reaction channel ^{7}Li(d,^{2}He)^{7}He, and $\Gamma_c(E)$ denotes the energy dependent total width of the decay of the ^{7}He $1p_{3/2}$ ground state into ^{6}He + n. The quantity $\Delta(E)$ is the energy shift function, given by

$$\Delta(E) = -S_c(E, r_{match})\gamma_{obs}^2 \tag{2.65}$$

with the shift factor S_c. The relation between the energy dependent total width $\Gamma_c(E)$ and γ_{obs}^2 is given by

$$\Gamma_c(E) = 2P_c(E, r_{match})\gamma_{obs}^2 \ . \tag{2.66}$$

The quantities S_c and P_c are functions of the channel wave functions

$$S_c(E, r_{match}) = r_{match}\frac{F_c\frac{dF_c}{dr} + G_c\frac{dG_c}{dr}}{F_c^2 + G_c^2}, \tag{2.67}$$

$$P_c(E, r_{match}) = \frac{kr_{match}}{F_c^2 + G_c^2} \tag{2.68}$$

where F_c and G_c are the regular and irregular solutions of the radial part of the free wave equation. From the Eq. (2.64) follows the energy of the resonance level as the solution of

$$E_{res} = E_c + \Delta(E_{res}). \tag{2.69}$$

3 Experimental setup

3.1 AGOR cyclotron at KVI

The measurements were carried out at the Kernfysisch Versneller Instituut (KVI) Groningen. The heart of the facilities for experimental nuclear physics at KVI is the Accelerator Groningen Orsay (AGOR) cyclotron [44] which was built in collaboration between the Institut de Physique Nucleare d'Orsay and KVI. This compact machine is capable for accelerating both light and heavy ions. There are three different ion sources: *ECRIS-3* produces highly charged heavy ions, *POLIS* polarized protons and deuterons and *CUSP* unpolarized protons and light ions. The maximum energy limitation of the proton beams, 190 MeV, is imposed by the focusing properties of AGOR. The maximum energy for heavy ions depends on their charge-to-mass ratio Q/A, with a maximum energy of 95 MeV/nucleon for $Q/A = 0.5$. An overview of the experimental facilities at KVI is given in Fig. 3.1.

3.2 Big-bite spectrometer

Both protons from ^{2}He decay were momentum analyzed with the magnetic Big-Bite Spectrometer, so-called BBS [45]. It consists of two quadrupoles Q_1 and Q_2 for focusing the particles which enter the spectrometer, and a dipole D for selecting the particles according to their momentum. A layout of the BBS and of the related detector system used for this experiment is shown in Fig. 3.2.

There are three configurations which differ in the positions of the quadrupole doublet with respect to the scattering chamber, they are called mode A, B and C. In mode A the quadrupole doublet is moved towards the target and the solid-angle acceptance reaches 13 msr. At the same time the momentum-bite acceptance is 13%. Particles with a magnetic rigidity deviating less than 6.5% from the nominal one are accepted by the spectrometer. In mode C, where the doublet is moved away from the target towards the dipole magnet, the situation is reversed. The

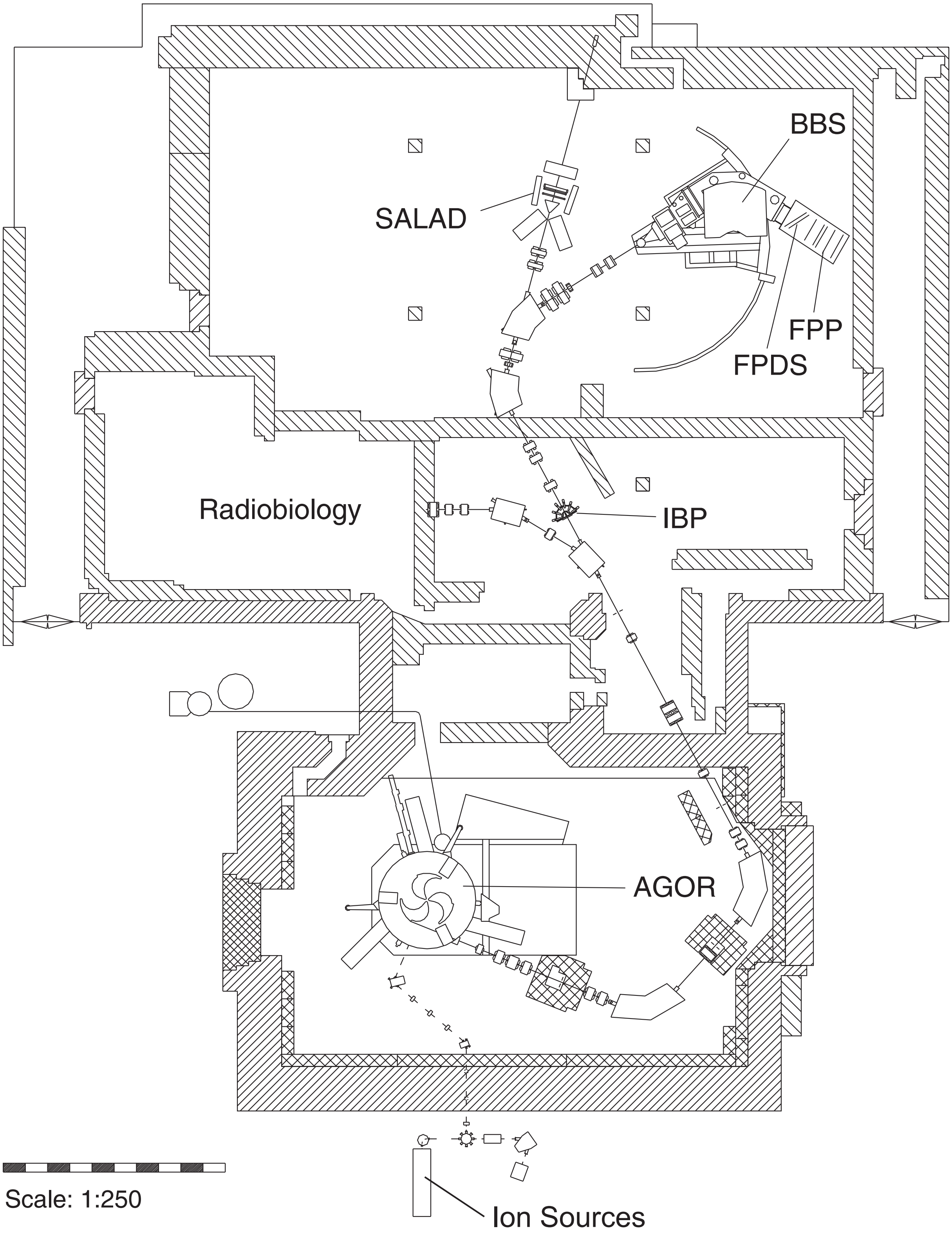

Fig. 3.1: Cyclotron and experimental halls at KVI.

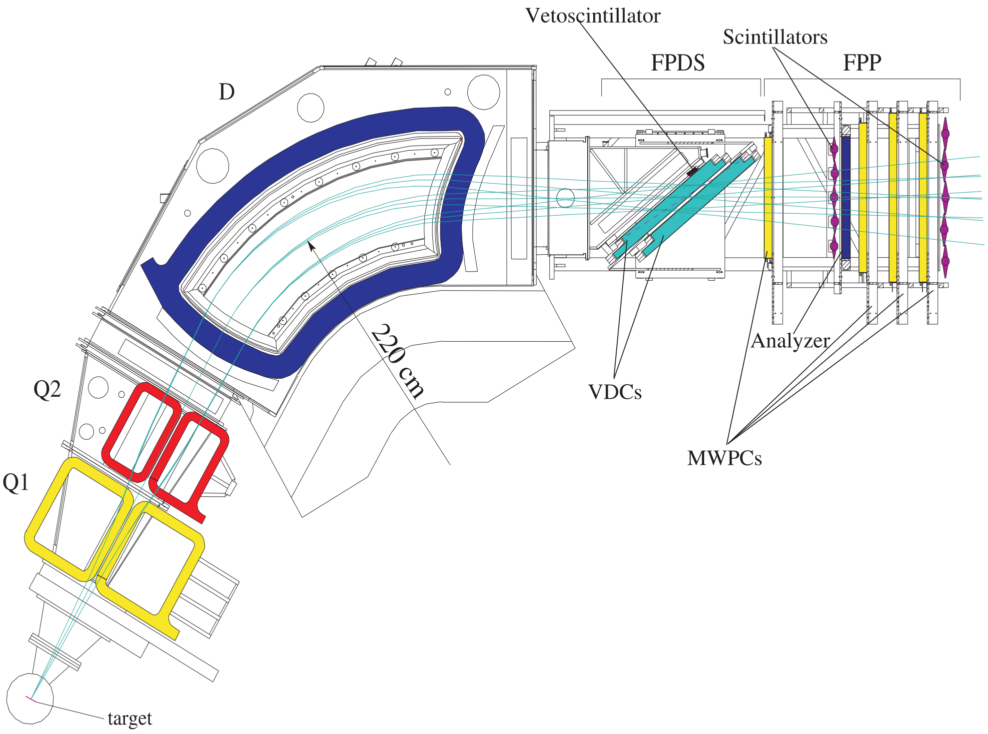

Fig. 3.2: Schematic drawing of the Big-Bite spectrometer and the attached detector systems.

solid angle decreases to 6.7 msr, and the momentum acceptance increases to 25%. Mode B was used in the present experiment, which is an intermediate setting to modes A and C. However, during the measurements the magnetic field of the first quadrupole was increased by 5% to improve the imaging properties of the spectrometer in the vertical direction. This leads to a reduction of the vertical opening angle of the BBS from 140 mrad to about 100 mrad and results in a solid angle of 6.6 msr (mode B*). The parameters of the BBS in the mode B* are given in Table 3.1. To achieve optimal momentum resolution the beam line to the spectrometer was adjusted for dispersion-matched beam transport.

3.2.1 Ray tracing

Both protons from the (d,^{2}He) reaction are measured at the focal plane of the BBS. In order to relate the measured quantities to parameters of the reaction at the target, the particles have to be transported through the spectrometer. The particle coordinates at the target (subscript t) are connected to those at the focal

Tab. 3.1: Design parameters for the BBS in mode B*.

Bending limit	430 MeV
Momentum bite $\frac{\Delta p}{p}$	19%
Solid angle $\Delta\Omega$	6.6 msr
Horizontal opening angle $\Delta\theta$	66 mrad
Vertical opening angle $\Delta\phi$	100 mrad

plane (subscript d) by a five-fold Taylor expansion

$$\alpha_t = \sum_{\mu,\nu,\lambda,\eta} (\alpha|x^\mu\theta^\nu y^\lambda\phi^\eta) x_d^\mu\theta_d^\nu y_d^\lambda\phi_d^\eta. \tag{3.1}$$

The target variables are denoted by α and can be θ, ϕ or δ. The coordinates x and θ describe positions and angles in the horizontal plane and y and ϕ similarly in the vertical plane. The deviation of the rigidity $B\rho$ of the particle with respect to a particle travelling along the central ray of the spectrometer is defined as δ

$$\delta = \frac{B\rho - B\rho_0}{B\rho_0}, \tag{3.2}$$

where B is the magnetic field and ρ_0 the bending radius of the central trajectory. The rigidity is linearly related to the momentum $p = mv$ via

$$B\rho = \frac{mv}{q}, \tag{3.3}$$

with q being the charge and m the relativistic mass of the particle. The coefficients of the Taylor expansion used to reconstruct the scattering variables at the target position were determined in a ^{11}B(p,p$'$) experiment [46] at $E_\mathrm{p} = 150$ MeV which is also suitable for the present experiment with lower energy protons (in this case $E_\mathrm{p} \leq 85$ MeV [47]). For a precise determination of the scattering angles near 0°, both horizontal and vertical scattering-angle components have to be measured with good accuracy. By adjusting the field strength of the quadrupole magnets, one can change the focusing properties of the spectrometer. At their nominal settings, the quadrupoles produce a crossover in the vertical focal-plane coordinate when going from the low- to the high-momentum side. Because not only the vertical position y_d but also the angle ϕ_d contain practically no information which would allow to reconstruct the vertical target angle ϕ_t, the field strength of the first quadrupole was adjusted to perform near point-to-parallel focusing over the region of the focal plane used during the experiments. This was achieved by increasing the magnetic field of the first magnet by 5%, as described above.

3.2.2 Recoil corrections

Due to the reaction kinematics particles transfer different recoil energies to the target nucleus at different scattering angles and thus arrive at different positions at the focal plane. This leads to the so called kinematic line broadening. This dependence is described in first order by a constant defined by

$$K = \frac{1}{p}\frac{dp}{d\Theta} \tag{3.4}$$

in [1/mrad] and can be calculated using a two-body kinematics code [48] like KINEMA. This effect can be compensated by software corrections and has been successfully applied in [46] to the focal-plane detection system used in the present experiment.

3.3 EUROSUPERNOVA detection system

For the detection of the outgoing protons from (d,^{2}He) reaction the focal-plane detector system [49] built by the EuroSuperNova collaboration has been used. It consists of two subsystems, the Focal-Plane Detection System (FPDS), and the Focal-Plane Polarimeter (FPP). A top view is shown in Fig. 3.3. The FPDS consists of a pair of gas-filled vertical drift chambers (VDC [50]) for momentum reconstruction of the protons. The FPP comprises multi-wire proportional chambers (MWPCs) and a pair of scintillator paddles S1 and S2 for time-of-flight and energy-loss measurements.

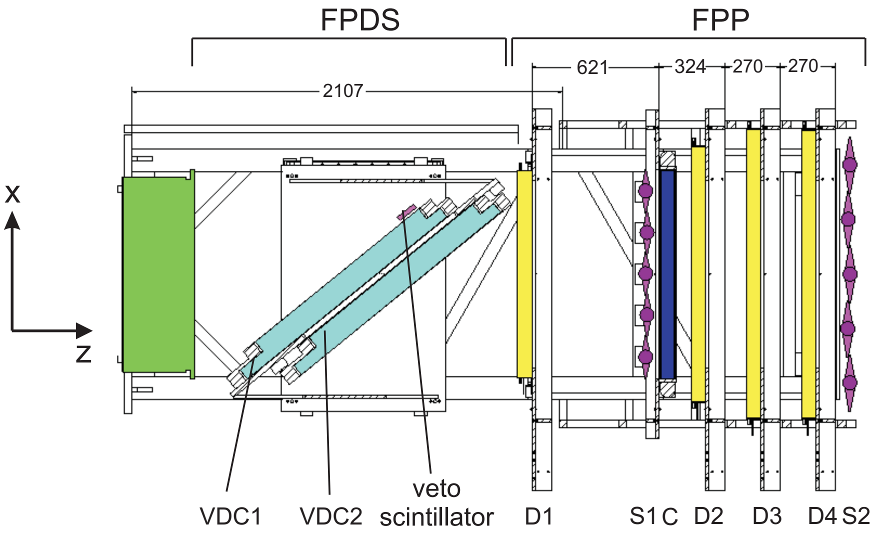

Fig. 3.3: Top view of the focal-plane detection system and the focal-plane polarimeter; dimensions are given in mm.

3.3.1 Focal-plane detection system

When a particle traverses the drift chambers, it ionizes the gas molecules contained in the chambers. The electrons then drift to the wires closest to the point of traversal. By measuring the arrival times of the pulses with respect to a common reference time, one gets a set of drift times. From the obtained drift times one can calculate the intersection point between the track and the wire plane.

The two pairs of Vertical Drift Chambers (VDCs) are positioned along the focal plane at an angle of 39° with respect to the beam direction. Each chamber has an X-plane and an U-plane with the wires of the U-plane titled by 32.86° against the vertical direction. Both drift chambers are filled with a gas-mixture consisting of 50% argon and 50% iso-butane. The active detection area of the VDCs is 1030×367 mm^2. The wire planes have alternating sense and guard wires, which act as anodes, whereas the VDC foils serve as cathodes. The number of sense wires in both chambers is 240. The wire pitch for the anode wires is 4 mm. The designed resolution of each VDC is 45 μm in the dispersive and 80 μm in the non-dispersive direction.

3.3.2 Focal-plane polarimeter

The Focal-Plane Polarimeter (FPP) consists of four MWPCs (Multi-Wire Propotional Chambers) D1-D4, which allow a precise and easy track reconstruction, and of two segmented scintillator planes S1 and S2 for time-of-flight and energy measurements. The FPP is placed perpendicularly to the central ray. A small *veto* scintillator can be mounted near the focal plane of the BBS allowing to suppress events from elastic scattering. Each MWPC consists of an X and Y plane with all together 2896 wires. The wire distance 2.5 mm defines the spatial resolution. Like the VDCs, the MWPCs are filled with a mixture of 50% argon and 50% iso-butane and a negative high voltage is applied to the cathode foils. The wires are kept at zero potential. If the detector is operated in the polarimeter mode, the polarization of scattered particles is deduced by measuring the asymmetry of secondary scattering in the graphite analyzer C which was removed during the (d,^{2}He) experiments.

3.3.3 Scintillators

As can be seen in Fig. 3.3, the S1 and S2 scintillator planes are located in front of the analyzer and behind the last MWPC, respectively. The coincidence between signals of the two planes defines the event trigger which starts the read-out of the front-end electronics and subsequent online event processing. Both scintillator planes consist of five overlapping scintillator paddles, which are read out from the top and bottom by photo-multipliers. The scintillating material used is NE102A. The thickness of the paddles of the second plane is 6 mm whereas it is only 2 mm in the first plane to reduce multiple Coulomb scattering.

3.4 Electronics

Figure 3.4 shows an overview of the read-out systems [46] of the focal-plane detection system and the focal-plane polarimeter consisting of preamplifiers, level converters, CAMAC-based read-out systems and VME-based real-time processing.

The timing information of the VDCs is digitized by two FERA (Fast Encoding Readout ADC) systems consisting of CAMAC based LeCroy 3377 drift chamber time-to-digital converters (TDC). Each TDC module contains 32 channels and is able to store up to 16 signals per channel with a digitizing resolution of 500 ps. The multi-hit capability of these TDCs is especially important in the case of the (d,^{2}He) measurement because two proton tracks per event have to be reconstructed in the detection system. The signals from the S1 and S2 scintillator planes are also read out by LeCroy 3377 TDCs. The MWPCs are read out using LeCroy PCOS (proportional chamber operating system) system which has been specially developed for wire chamber read-out. Instead of producing timing information PCOS only reports which wires have fired in an event, making it faster than TDC systems. As an example, the total read-out time in (p,p$'$) measurements amounts $t = 6.6$ μs and allows the system to handle read-out rates of 100 kHz at a dead-time of 67%. More detailed descriptions can be found in Refs. [46, 51].

3.4.1 Trigger logic

The event trigger is based on a coincidence of signals from the two scintillator planes in the absence of a signal from the *veto* scintillator. It initiates CAMAC read-out by distributing common stop and gate signals to the TDC and PCOS systems and allows to inhibit the generation of new trigger signals in case one of the systems is 'busy'. The signals of both photomultipliers from each scintillator are combined by a meantimer, which requires both signals to be present within a time interval of 30 ns. A logical OR of these signals is used to create the output signal for each scintillator array separately. The main trigger signal is generated as a logical AND of the signals of scintillator arrays S1 and S2. From the main trigger signal the gates for the different readout systems are generated via another logical AND. It suppresses the trigger signal, if the readout of the last event is not yet complete, i.e. some of electronic modules provide a 'busy' signal. The separation of the main trigger signal from the incorporation of the 'busy' signals has the advantage that the life time of the readout system can be determined directly as the quotient of the number of coincidences from the two logical ANDs.

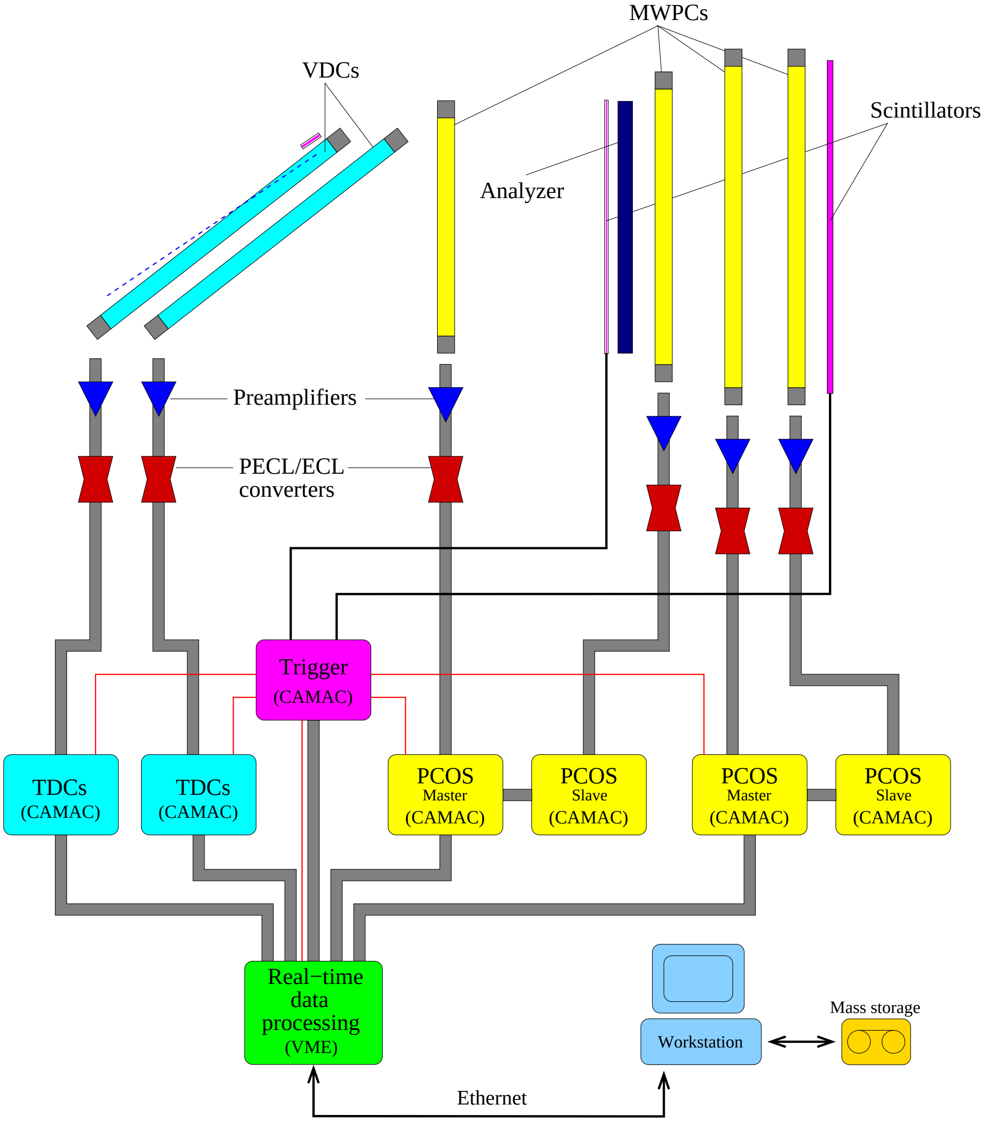

Fig. 3.4: Schematic view of the read-out system.

3.4.2 DSP-based online data processing system

The complete detector is then read out by a DSP (digital signal processor) system [52]. The DSPs STR 8090 act as an event filter, as they make the decision whether an event is recorded to tape or discarded. In either case the detector dead-time can be kept below 8 μs, thereby allowing high trigger rates. The DSP software checks if the data from the MWPCs are consistent with two coincident proton tracks. Only in this case, the data from the VDCs at the focal plane, together with all other detector data, are recorded on tape. The system shown in Fig. 3.5 consists of five first-in-first-out (FIFO) modules STR 7090 to buffer event

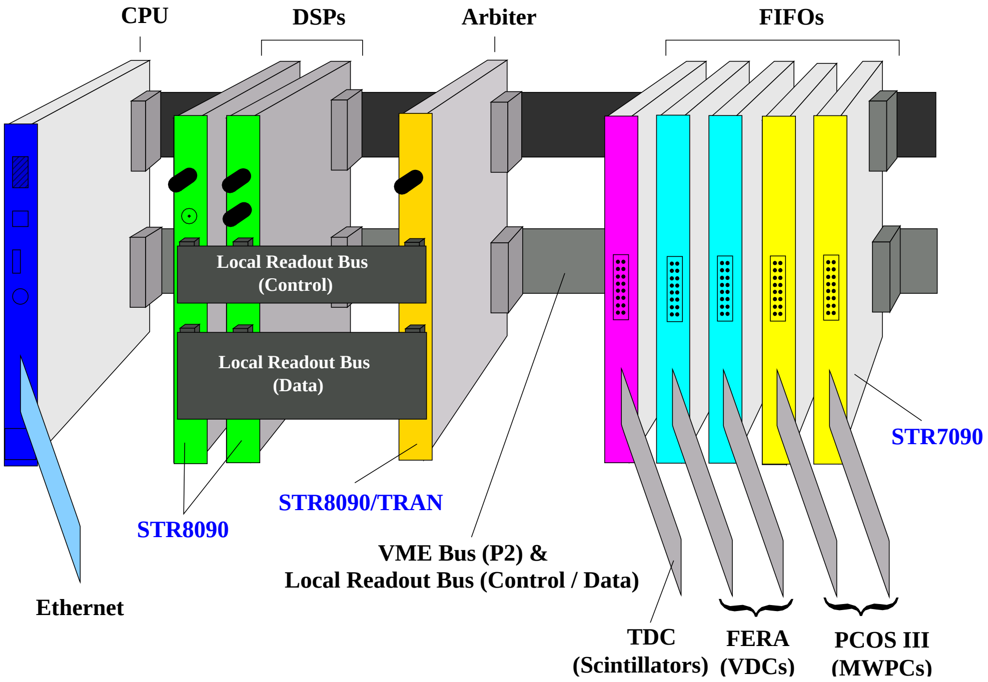

Fig. 3.5: VME-based real-time processing electronics.

data, an arbiter module STR 8090TRAN to distribute the data and a number of DSPs which perform the necessary tests. The data flow proceeds as follows: after receipt of a trigger signal and subsequent read-out of the detectors by the CAMAC systems, all data are transferred to VME FIFO modules. Additional trigger signals are inhibited by returning a 'busy' signal to the trigger logic until the data transfer has been completed or a time-out signal occurs. Once a complete event has been read, the 'busy' signal is removed to allow the next event to be read out by the front-end electronics. Complete events are transferred via an arbiter module to one of several DSP modules which perform the necessary calculations. The FIFO module is connected to the arbiter and the DSP modules by the VME-independent local readout bus (LRB).

The LRB provides a fast data transfer between the FIFO modules and the DSP section, which is controlled by the arbiter module using a dedicated token protocol. This allows the use of multiple parallel working DSP modules connected to the same LRB. Besides, the computing power of the system can always be increased by adding further DSP modules. The DSP software running during the (d,^{2}He) experiments can be subdivided into three main steps: data readout and data consistency checks, software trigger decision, and data output. To summarize the applied DSP event filter, at least one hit has to be recorded in each MWPC plane and there must be two wire chambers with at least 3 hits.

The overall dead-time of the complete system is kept below 10 μs which corresponds to a theoretical limit for the event throughput of 100 kHz. More information on the online processing system can be found in Refs. [52, 53].

3.5 Data acquisition and online analysis

The heart of the data acquisition [46] is an Alpha AXP-VME 4/288 Workstation operated with the system VxWorks. It connects electronics and network and runs the data acquisition software D2HEDAQ and the slow-control. The DAQ software one can use for both online and off-line analysis. It is based on the CDAQ library which was developed by Zwarts at KVI [54]. There are three processes which run during the experiment on different computers: processed data from the DSP system are read out by the first DAQ process on the VME CPU. The data are then transferred to a Linux PC in the control room via Ethernet where it is picked up by a second process. The second process stores all data on DLT tape and sends a load-dependent percentage of the data via the KVI network to a third process on another Linux PC which is used for online analysis and visualization. All these modules are controlled via TCP/IP connections by a graphical user interface FPPGUI.

To be able to continuously monitor and control the most important experimental parameters of the detector systems a slow-control software has been developed [47]. The slow-control consists of two components: slowserver which runs on the VME workstation and slowclient on one of the Linux PCs. Via the graphical user interface it is possible to display scaler data, set and monitor the wire chamber high voltages and change preamplifier thresholds.

Data visualization in the online and further treatment of the data in the off-line case is realized using the PAW package [55] from the CERN library. During the experiments the results of the online analysis are booked into histograms in a shared-memory region. Using PAW one can access and display these histograms.

For off-line analysis the resulting variables are written on event-per-event basis to a file in NTUPLE format. This format is understood directly by PAW and allows an effective further analysis of the data.

3.6 ^{2}He event reconstruction

The analysis is divided into few different steps. First, using the D2HEDAQ analysis the raw data are unpacked and then sent to the interpretation routine, which extracts the relevant information including signals from scintillator detectors and wire chambers. The most complex part of the interpretation resides in the determination of the VDC intercepts, since two correlated tracks (protons from ^{2}He decay) have to be reconstructed out of several drift times. These two tracks are almost simultaneous (less than 10 ns of time difference) and can only be resolved because of the multi-hit capability of the TDCs used, which register more than one time per channel before a stop signal is set by the trigger. The VESNA^{n}(**V**DS **E**uro**S**uper**N**ova **A**nalysis for **n** particles) software developed by Schmidt [56] was applied in the present experiment for the track reconstruction. Having the intercepts from the VDCs data, the focal-plane variables like horizontal and vertical positions and angles can be determined. Then the kinematic recoil correction has to be done (see Section 3.2.2). Finally, using the ray-tracing information (see Section 3.2.1), the target variables for each proton are calculated. Thus, all the information characterizing the ^{2}He particle like kinetic energy, scattering angle and internal energy can be extracted. The details of the analysis can be found in Chapter 4.

3.7 Experiment

The present experiment was performed in April 2003 at KVI in Groningen. Deuterons from the *CUSP* ion source were accelerated to a kinetic energy of 171 MeV. The deuteron beam was incident on a ^{7}Li target isotopically enriched to 99.9% and having a thickness of 9 mg/cm^2. Measurements were made at four different spectrometer angle settings corresponding to center-of-mass angles $\Theta_{cm} = 0° - 11.3°$. The two protons from ^{2}He were momentum analyzed by the BBS and detected by the ESN-detection system. The beam current varied between 0.3 nA and 1.5 nA, dependently on the spectrometer angle. As a test, for each angle, measurements on ^{12}C were performed as this nucleus has been studied extensively with the (d,^{2}He) reaction [47, 51]. Measurements on a 9.4 mg/cm^2 thick natural carbon target served for the determination of the experimental energy resolution $\Delta E \simeq 150$ keV (FWHM). The test measurements provide also a possibility to verify the correct operation of the detector system and of the analysis procedure applied in this work.

4 Data analysis

In this chapter, the different steps performed during the data analysis will be described. First, the determination of the scattering variables needed to obtain the excitation energy spectra will be outlined. The acceptance and background correction procedures will be given in Sections 4.2 and 4.3. Then the extraction of the experimental cross sections will be described. Finally, the quasifree continuum background will be determined and resulting fit of the ^{7}He spectra will be shown. The last two Sections discuss the decomposition of the spectra, aiming at a possible identification of a low-lying resonance in the ^{7}He nucleus.

4.1 Reconstruction of the scattering variables

The reconstructed VDC intercepts from the drift-time information using a sophisticated algorithm (shortly described in Section 3.6) are related to the focal plane coordinates by simple geometry. The horizontal position at the focal plane is directly given by the crossing point of the X-plane of the first VDC. The determination of the remaining coordinates like the vertical position, the horizontal and vertical detector angles is then straightforward using the information from the three other VDC planes. As explained in Section 3.2.1, the target variables were obtained using a ray-tracing procedure. The horizontal scattering angle $\theta_{t,1(2)}$, the vertical scattering angle $\phi_{t,1(2)}$ and the momentum $p_{1(2)}$ are determined for both protons, denoted by subscripts 1 and 2. The kinetic energy is calculated first for each proton separately, the ^{2}He total energy follows from the sum of these two proton energies. The momentum of the protons can be calculated from the BBS dipole field B and relative magnetic rigidity (given in %)

$$p = \frac{qB\rho_0(1+\delta)}{3.3356 \times 10^{-3}} \tag{4.1}$$

where $B\rho_0$ is the magnetic rigidity of the central ray in Tm, q is the charge of the particle and δ is defined in the Section 3.2.1. The kinetic energy of each proton is calculated as

$$E_{kin,1(2)} = \sqrt{m^2c_p^4 + p_{1(2)}^2} - mc_p^2, \tag{4.2}$$

where m_p is the rest mass of the proton. The direction vectors $\hat{r}_{1(2)}$ of the protons can be obtained from the target coordinates according to

$$\hat{r}_{1(2)} = \begin{pmatrix} \sin(\Theta_{BBS} + \theta_{1(2),zx,t}) \cdot \cos(\phi_{1(2),zy,t}) \\ \sin(\phi_{1(2),zy,t}) \\ \cos(\Theta_{BBS} + \theta_{1(2),zx,t}) \cdot \cos(\phi_{1(2),zy,t}). \end{pmatrix} \tag{4.3}$$

The relative angle between two protons (opening angle) in the laboratory system, the total momentum and the scattering angle for d → ^{2}He in the laboratory system can be expressed in the following way

$$\Theta_{pp} = \arccos(\hat{r_1}, \hat{r_2}), \tag{4.4}$$

$$\vec{p} = \hat{r_1} \cdot p_1 + \hat{r_2} \cdot p_2, \tag{4.5}$$

$$\Theta = \arccos \frac{p_z}{p}. \tag{4.6}$$

Using the kinematics library KINEMA [48] one can convert scattering variables into the center-of-mass system and calculate the excitation energy E_x from the difference between beam energy E_d, kinetic energy $E_{^2\mathrm{He}}$, recoil energy E_R and the Q-value of the reaction. Finally, the relative energy ϵ of the two protons can be obtained from kinetic energies of the protons and from the opening angle

$$\epsilon = \frac{E_1 + E_2}{2} - \sqrt{E_1 E_2} \cos \Theta_{pp}. \tag{4.7}$$

4.2 Acceptance correction

Due to the limited momentum and angular acceptance of the BBS spectrometer and the diparticle nature of ^{2}He, the experimental spectra need to be folded with an acceptance function [57]. This correction function takes the settings of all BBS magnets and the reaction kinematics into account and is obtained by a Monte-Carlo simulation [51]. The easiest way to do the acceptance correction is to calculate the detection probability of two correlated protons as a function of the solid angle and the excitation energy in the residual nucleus for a given

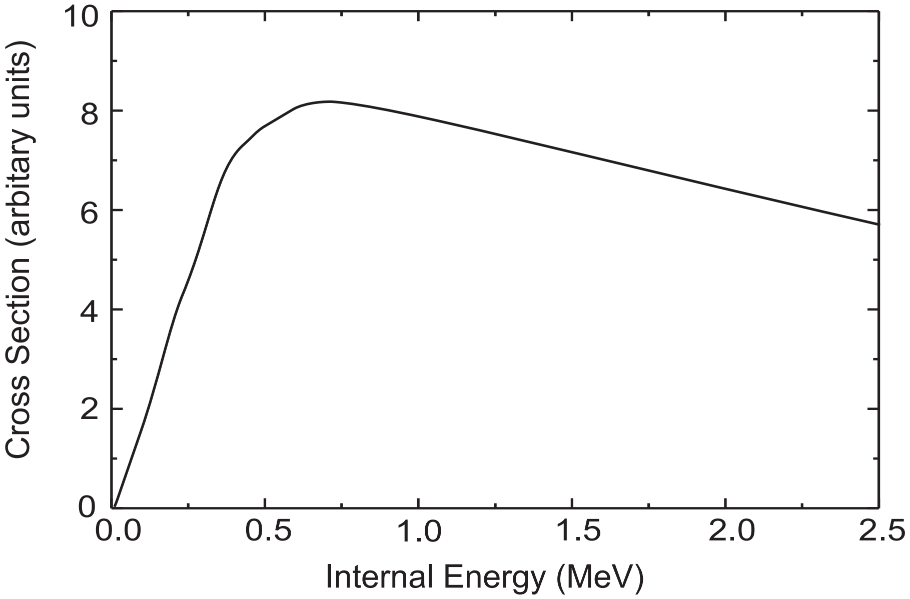

Fig. 4.1: Calculated internal energy spectrum of the two protons in ^{2}He from Watson-Migdal FSI theory [58, 59].

range of internal energies ϵ. In the present work the limits for ϵ were chosen to be $0< \epsilon <1$ MeV, because the maximum relative proton energy which can be observed with the BBS+ESN system is about 1 MeV.

To determine the acceptance function, the (d,^{2}He) reaction is simplified to two independent two-body reactions. In the first step of the scattering reaction the ^{2}He particle is treated like a bound particle

$$\mathrm{d} + \mathrm{A} \rightarrow ^2 \mathrm{He} + \mathrm{B}\ . \tag{4.8}$$

The ^{2}He system decays into two protons in the second step. This is the so-called final-state interaction (FSI)

$$^2\mathrm{He} \rightarrow \mathrm{p} + \mathrm{p}. \tag{4.9}$$

The first step is governed by two-body kinematics and only needs the random generation of an excitation energy of the residual nucleus, an internal energy for ^{2}He, polar and azimuthal scattering angles. The internal energy ϵ, computed using input data from the FSI theory of Watson [58] and Migdal [59] is shown in Fig. 4.1. In the second step it is assumed, that the ^{2}He nucleus decays isotropically into two protons in the center-of-mass system. A Lorentz transformation brings the center-of-mass coordinates of the two protons to the laboratory frame.

After the simulation of the ^{2}He decay, the full set of kinematic parameters is available for both protons at the reaction point (target), such as horizontal $\Theta_{zy,i}$ (i = 1, 2) and vertical coordinates $\Phi_{zy,i}$ ($i = 1, 2$), and the single-proton momentum $\Delta p/p_{0,i}$ (i = 1, 2) coordinates. This allows to calculate the transport of the two protons from the target through the spectrometer to the focal plane using the ray-tracing technique described in Section 3.2.1, yielding the coordinates of each proton at the detector surface. The same gates as used in the analysis of measured data are applied on the detector coordinates in a simulation procedure. To include resolution effects the detector positions are convoluted with Gaussian peaks with appropriate widths. As the next step, new target coordinates of both protons are calculated by transporting then back through the spectrometer from its focal plane to the target, using again the ray-tracing technique. Finally, one obtains a set of variables for each initial proton and a set of variables after its transport from target to detector and back, without any constraints on solid-angle acceptance, detector acceptance and gates. From the set of variables belonging to the protons that have been transported through the spectrometer, one calculates the excitation energy spectrum.

The same two-dimensional cuts that used in the experiment, are applied to obtain the acceptance-correction function. As an example the experimental gates for all acceptance-relevant variables as momentum, y-coordinate and scattering angles $\Theta_{zy,i}$ (i = 1, 2) and $\Phi_{zy,i}$ (i = 1, 2) are displayed in Fig. 4.2. On the l.h.s. of the Fig. 4.2 the cuts indicated as solid lines for $\Theta_{BBS} = 0°$ without an aperture at the entrance of the BBS and on the r.h.s. for $\Theta_{BBS} = 7.8°$ with an aperture are shown. The offset for Y_d can be determined when using the aperture. As the opening angle of the di-proton system varies event by event in a (d,^{2}He) reaction, the single-proton coordinates in the focal-plane are broad distributions as shown in Fig. 4.2. The simulated acceptance-correction function $F(\Delta\Omega, \Delta E)$ for a certain solid angle is determined by calculating the ratio between hypothetically non-decaying ^{2}He particles and di-protons from the ^{2}He decay reaching the detector. A typical example is shown in Fig. 4.3 for the ^{7}Li(d,^{2}He) reaction at c.m. angles between 0° and 1°. The shape is triangular with an indication of a flat top and can be parameterized by two Gaussians. Since the acceptance function depends on the central momentum of the magnetic spectrometer it needs to be reevaluated each time the field is changed. The ^{2}He detection probability is taken

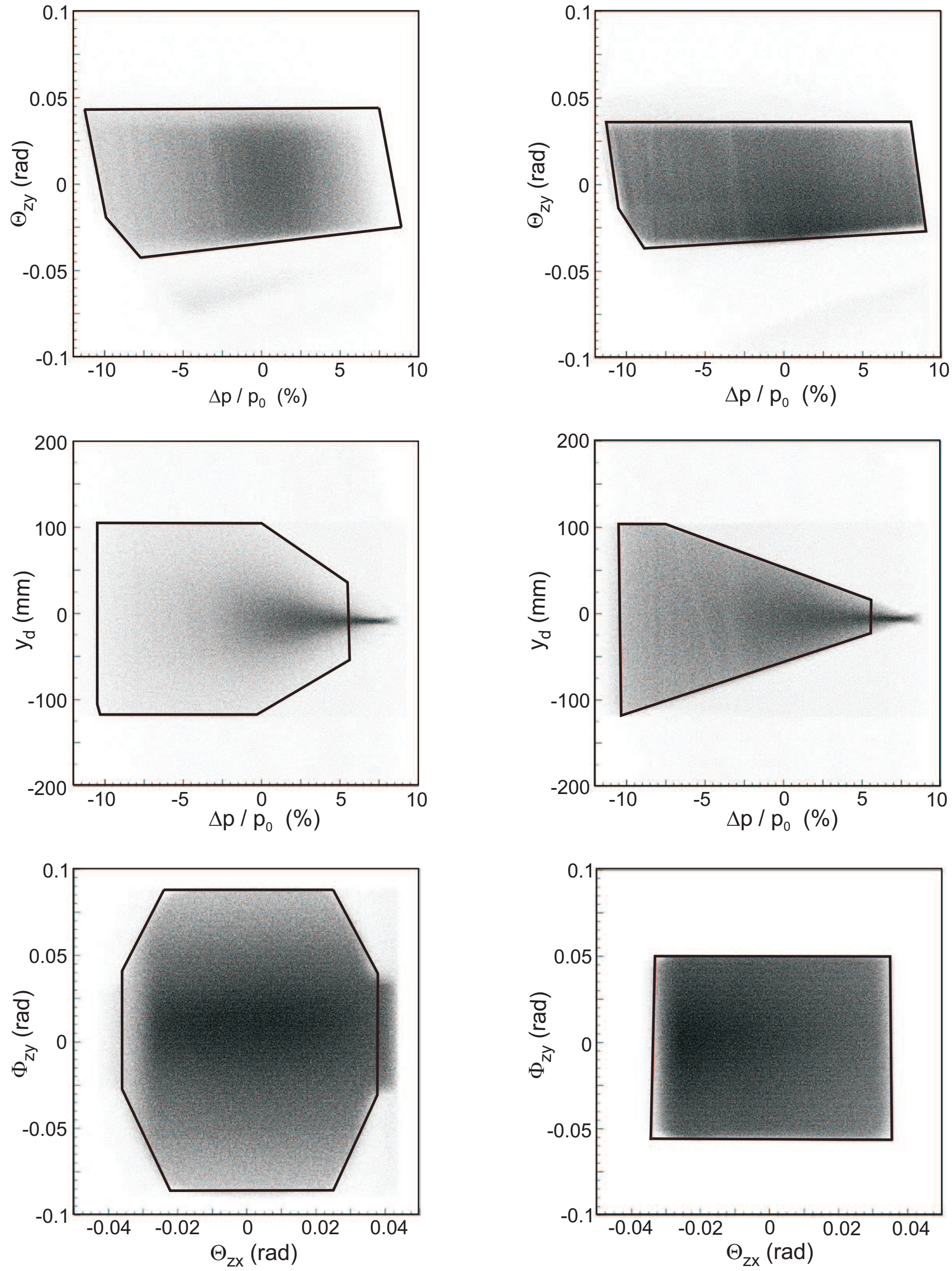

Fig. 4.2: Focal-plane spectra of protons from the ^{7}Li(d,^{2}He)^{7}He measurement at $\Theta_{BBS} = 0°$ (left panel) and $\Theta_{BBS} = 7.8°$ (right panel). The different forms in the left and right panels result from the use of an aperture at the entrance of the BBS for the latter. Experimental cuts used for the determination of the acceptance-correction function are shown as full lines. See text for further explanations.

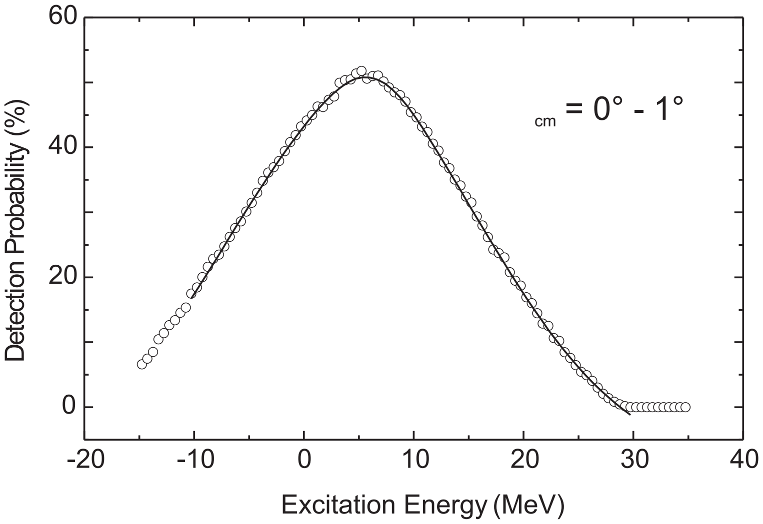

Fig. 4.3: Simulated acceptance-correction function for the ^{7}Li(d,^{2}He) reaction at Θ_{cm} = 0° - 1° and the result of the fit by two Gaussians.

into account by defining an effective solid angle $\Delta\Omega_{eff} = F(\Delta E)\Delta\Omega$ which is then used (see Section 4.4) to calculate the experimental double-differential cross section. Systematic errors due to the uncertainties in the determination of the effective solid angle are of the order of 15%.

4.3 Instrumental background subtraction

The background in the measured raw spectra is due to uncorrelated protons detected within the coincidence window in the FPDS and comes mainly from the deuteron breakup reaction on the target nucleus. The first step in the background subtraction procedure is the experimental separation of protons originating from different beam bunches of the cyclotron. The interval between two beam bunches was as small as 23 ns (repetition rate of the cyclotron). A typical example of the time difference between two protons measured at the focal plane of the spectrometer is shown in Fig. 4.4. As can be seen, the prompt peak at 0 ns, stemming from two protons of the same beam bunch, is well separated from random peaks (coincidences between two protons from different beam bunches). Small contribution of random protons within the prompt peak can be subtracted by applying

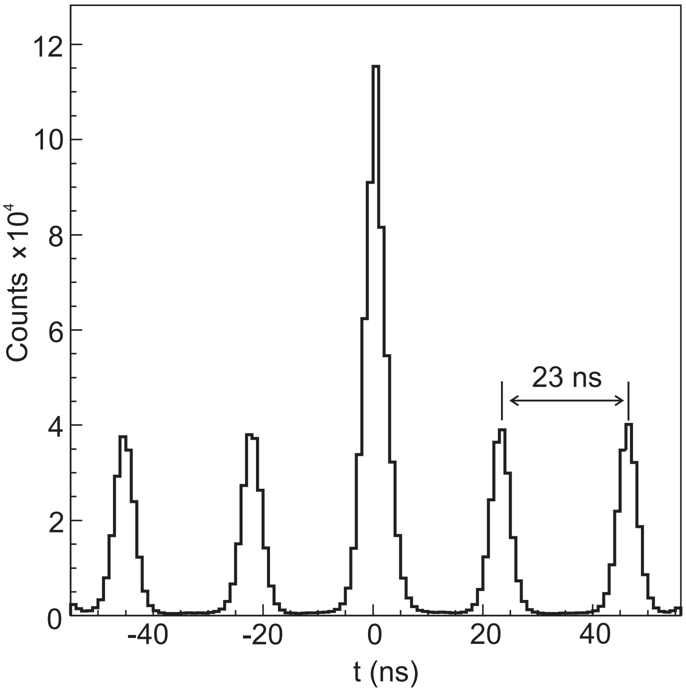

Fig. 4.4: Spectrum of the time difference between two protons at the focal plane of the BBS. A prompt and four random peaks are visible. The time interval between two peaks is equivalent to the inverse of the beam repetition rate of 43 MHz (i.e. 23 ns).

gates on the random and the prompt peak, respectively. Figure 4.5 presents the background spectrum obtained after gating on the random peak. To minimize the statistical variation of the random distribution and to smooth it, the random excitation energy spectrum was fitted with a fourth-order polynomial function before subtraction from the prompt one. The background subtraction procedure is shown in Fig. 4.6. There is a small contamination from the ^{12}C(d,^{2}He)^{12}B observed in the spectrum. Besides the ^{12}B ground state, the contribution to the spectrum is very small. In order to remove this contribution, the measured ^{12}C(d,^{2}He) spectrum has been scaled by a normalization factor which is calculated from the ratio between the ^{12}B g.s. peak area in the ^{7}He spectra and those of the measurements using a ^{12}C target. As can be seen by comparison of Fig. 4.7 and Figs. 4.8,4.9, after this procedure the boron peaks can be subtracted from the ^{7}He spectrum.

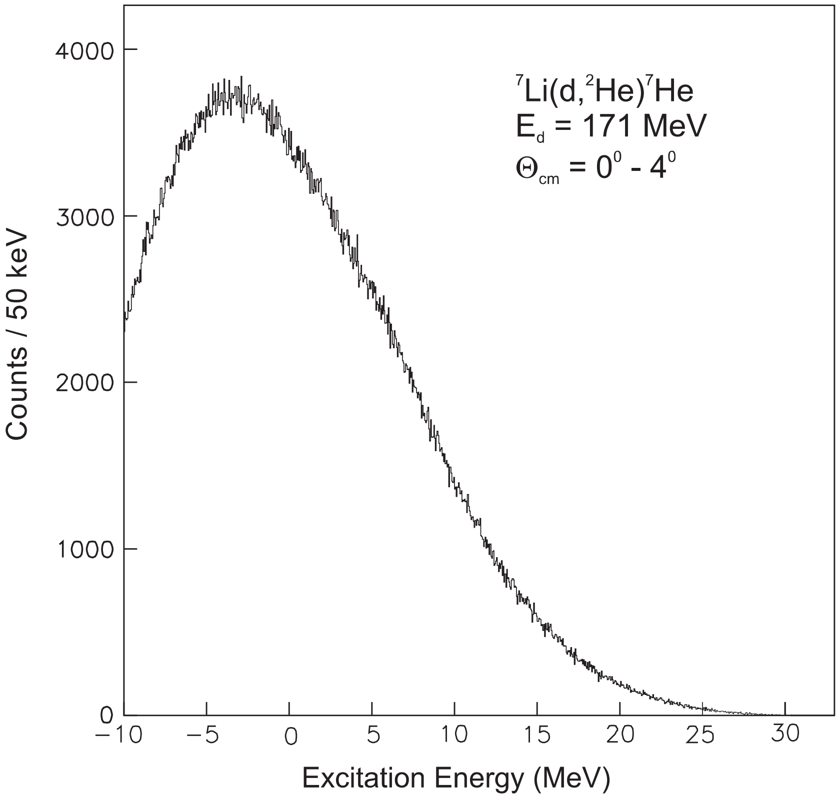

Fig. 4.5: Excitation energy spectrum produced by gating on the random peak of the time difference distribution between two protons.

4.4 Angular bins and experimental cross sections

Data, measured at different BBS settings, have to be divided into angular bins in order to obtain angular distributions. Each setting of the spectrometer angle was split into two or three bins, depending on the statistics, with a width of $\Delta\Theta_{cm} = 1°$ as is shown in the Tab. 4.1. A Monte-Carlo simulation has been performed for every experimental setting of the spectrometer and for different bins in scattering angle.

The experimental double-differential cross section in the excitation energy bin ΔE_x and the solid-angle bin $\Delta\Omega$ is calculated according to

$$\frac{d^2\sigma}{d\Omega dE_\mathrm{x}} = 0.266\,\frac{A}{Tk}\,\frac{1}{Q(1-\tau)\alpha^2}\,\frac{N_{\Delta E_\mathrm{x},\Delta\Omega}}{\Delta E_\mathrm{x}\Delta\Omega_\mathrm{eff}} \qquad \left[\frac{\mathrm{mb}}{\mathrm{srMeV}}\right] \tag{4.10}$$

with

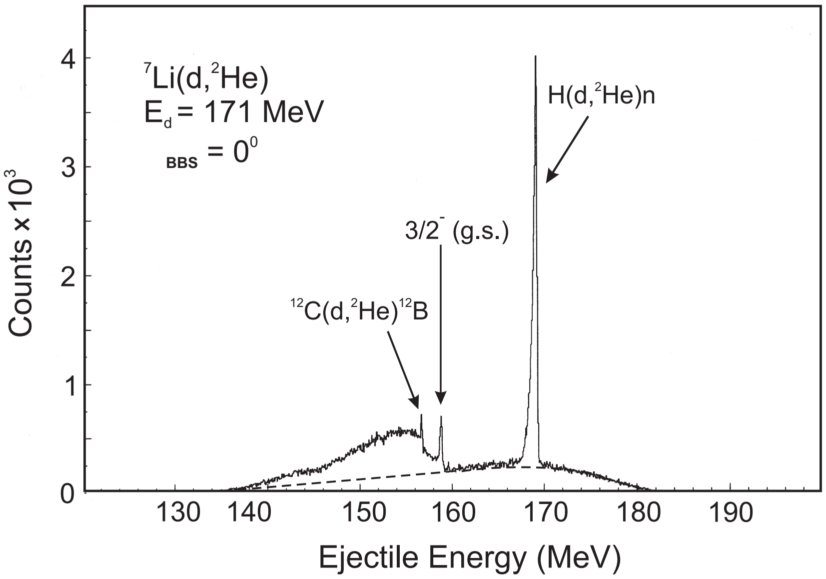

Fig. 4.6: Spectrum of ^{7}He after gating on the prompt and the random peaks of the time difference distribution between two protons. The dashed line is the result of the fourth-order polynomial fit applied to the random spectrum shown in Fig. 4.5.

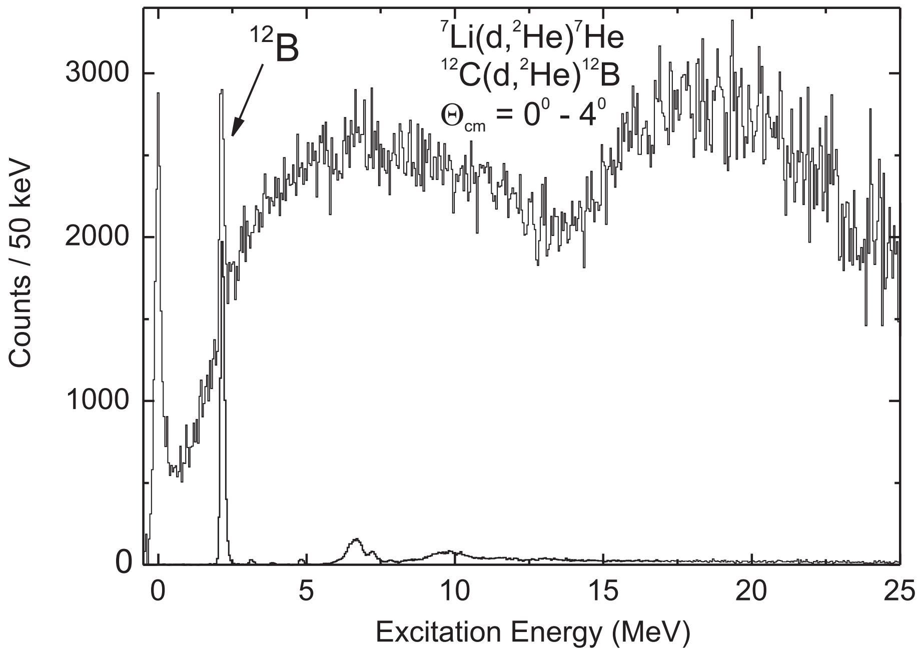

Fig. 4.7: Subtraction of ^{12}B from the ^{7}He spectrum after background and acceptance correction.

Tab. 4.1: Angular bins created in the data analysis.

Θ_{lab}(BBS)	$\Delta\Theta_{cm} = 1°$		
0°	0° - 1°	1° - 2°	2° - 3°
3°	3.7° - 4.7°	4.7° - 5.7°	
5°	5.9° - 6.9°	6.9° - 7.9°	
7.8°	9.3° - 10.3°	10.3° - 11.3°	

A : target mass [g/mol],
T : target thickness [mg/cm^2],
k : isotopic enrichment,
Q : integrated charge in [nC],
τ : dead time,
α : detector efficiency,
$N_{\Delta E_x,\Delta\Omega}$: number of counts in the bin $\Delta\Omega$ ΔE_x,
$\Delta\Omega_{\text{eff}}$: effective solid angle [sr] (see Section 4.2),
ΔE_x : energy bin [MeV].

The acceptance and background-corrected double-differential cross sections at excitation energies up to 25 MeV are shown in Figs. 4.8 and 4.9 and listed in the table in Appendix. The data can also be found in World Wide Web [60].

4.5 Quasifree continuum background

Quasifree charge-exchange is a major source of nonresonant continuum background. The quasifree scattering (QFS) refers to reactions in which the neutron scatters from a single proton in the target, essentially as if the rest of the nucleus was not present. In this context the term QFS means the single-step quasifree nucleon knockout reaction. The struck proton is emitted from the target nucleus and is detected in the spectrometer. In particular, the (d,^{2}He) charge-exchange

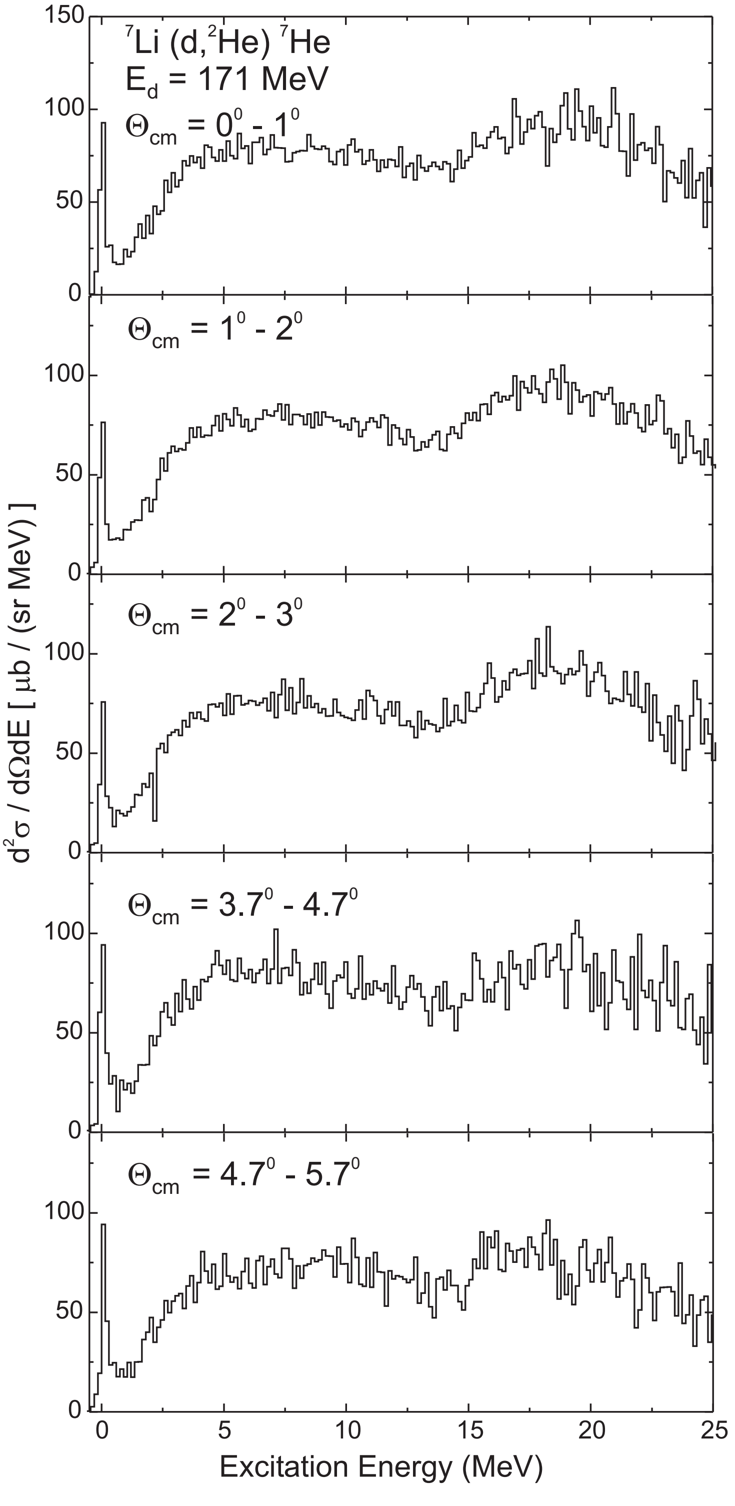

Fig. 4.8: Double-differential cross sections for the ^{7}Li(d,^{2}He) reaction measured at various scattering angles $\Theta_{\mathrm{c.m.}} = 0° - 5.7°$.

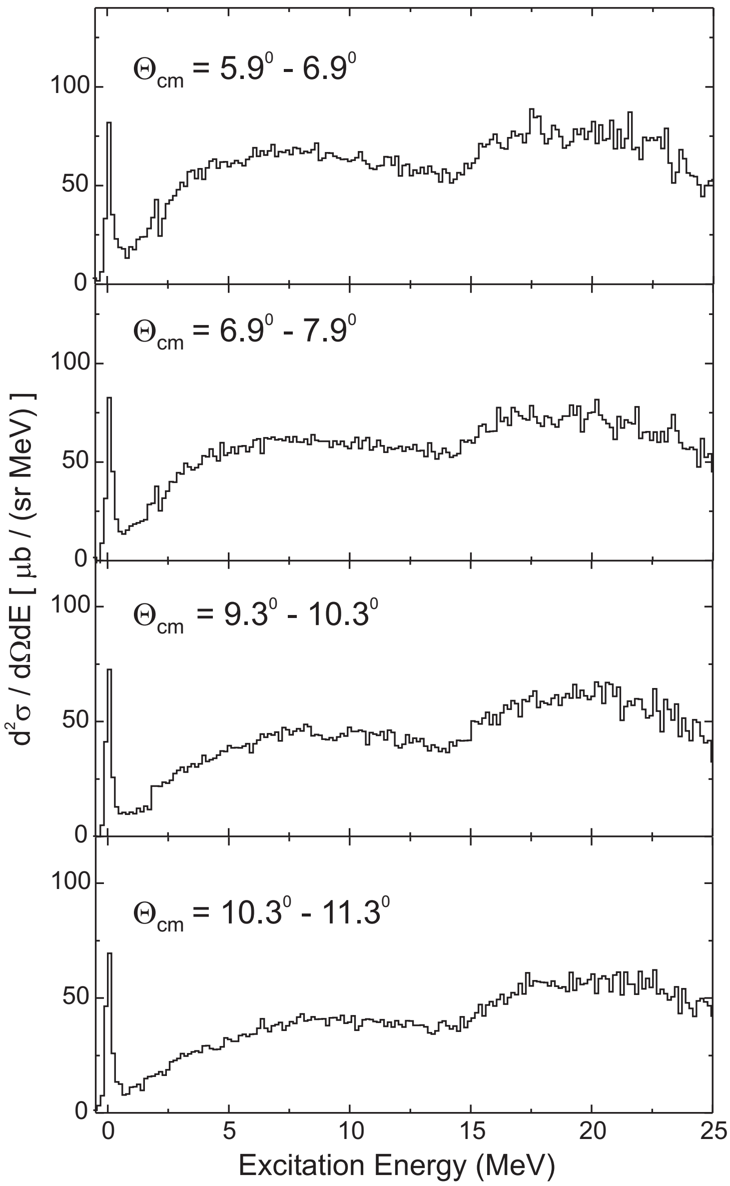

Fig. 4.9: Double-differential cross sections for the ^{7}Li(d,^{2}He) reaction measured at various scattering angles $\Theta_{\rm c.m.} = 5.9° - 11.3°$.

reaction on a bound proton leads to the ejection of the charge-exchanged neutron from the residual nucleus in its ground state or excited state. To deal with the QFS in the analysis, the technique developed by Erell *et al.* [61] in a study of pion charge-exchange reaction is used. This semi-phenomenological parametrization has been applied successfully to intermediate-energy charge-exchange

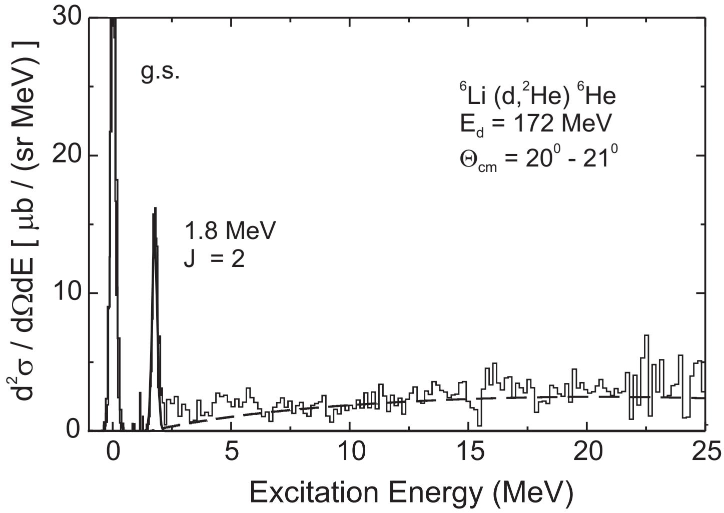

Fig. 4.10: Spectrum of the ^{6}Li(d,^{2}He) reaction at E_d = 171 MeV and Θ_cm = $20° - 21°$ (from an analysis of Ref. [67]). The long-dashed line is a fit of a semi-phenomenological model [61] for the quasifree scattering cross section.

reaction spectra [62–66]. The shape of the background is described by

$$\frac{d^2\sigma}{d\Omega dE} = N \frac{1 - \exp\left(\frac{E - E_0}{T}\right)}{1 + \left[\frac{E - E_\mathrm{QF}}{W_\mathrm{L}}\right]^2} , \tag{4.11}$$

where E, E_QF and E_0 denote the outgoing ^{2}He energy, the maximum of the quasifree peak approximated by a Lorentz function and a cutoff energy due to Pauli blocking, respectively. The cutoff energy E_0 represents the threshold for three-body breakup

$$E_0 = E_{^2\mathrm{He}}(^7\mathrm{He}_\mathrm{g.s.}) - S_\mathrm{n} . \tag{4.12}$$

The quasifree peak energy is determined from the comparison of the quasifree (d,^{2}He) reaction on the target with the analogous elementary reaction on the proton

$$E_\mathrm{QF} = E_{^2\mathrm{He}}(^1\mathrm{H}) - S_\mathrm{n}. \tag{4.13}$$

Here, $E_{^2\mathrm{He}}$ denotes the kinetic energy of the ^{2}He particles for the ^{1}H(d,^{2}He) reaction and S_n = -0.445 MeV the neutron separation energy in ^{7}He. In other words, the centroid energy E_QF of the quasifree process is shifted relative to that of the charge-exchange reaction on a free proton by the neutron binding energy in residual nucleus. Unlike with (p,n) - type reactions no shift due to a Coulomb barrier needs to be included [63]. The Lorentzian width W_{L} depends on the momentum transfer q

$$W_{\mathrm{L}} = W_{\mathrm{L}_0} \left[1 + \alpha \left(\frac{q}{k_{\mathrm{F}}} \right)^2 \right] . \tag{4.14}$$

The scaling parameter $T = 4.0$ MeV and the parameters $W_{\mathrm{L}_0} = 16.26$ MeV, $\alpha / k_{\mathrm{F}}^2 = 0.363\ \mathrm{fm}^{-2}$ from Eq. (4.14) were determined by a measurement of the ^{6}Li(d,^{2}He)^{6}He reaction [67] under the same kinematical conditions as the present experiment at large scattering angles, where the quasifree cross section should dominate. It may be noted, that the results of Ref. [67] obtained independently at different momentum transfers indicate, that the normalization factor N is q-independent. This is also consistent with findings of Wang *et al.* [68] for the quasifree cross sections in the (p,n) reaction on p-shell nuclei. As demonstrated in Fig. 4.10 for the example of the angular bin $\Theta_{\mathrm{cm}} = 20^\circ - 21^\circ$, the approach of [61] provides a good description ^{6}Li(d,^{2}He)^{6}He data. The background parameters for the ^{7}Li(d,^{2}He) reaction as a function of angle, are listed in Tab. 4.2

Tab. 4.2: Angle-dependent parameters for the quasifree background parametrization of Eq. (4.11).

Θ_{cm}	q_{cm} (fm^{-1})	W_{L} (MeV)	E_{QF} (MeV)	E_0 (MeV)
$0^\circ - 1^\circ$	0.039	16.27	168.744	158.719
$1^\circ - 2^\circ$	0.087	16.30	168.618	158.702
$2^\circ - 3^\circ$	0.140	16.38	168.367	158.667
$3.7^\circ - 4.7^\circ$	0.233	16.58	167.651	158.568
$4.7^\circ - 5.7^\circ$	0.288	16.75	167.060	158.486
$5.9^\circ - 6.9^\circ$	0.354	17.00	166.187	158.365
$6.9^\circ - 7.9^\circ$	0.409	17.25	165.313	158.244
$9.3^\circ - 10.3^\circ$	0.541	17.99	162.721	157.886
$9.3^\circ - 10.3^\circ$	0.597	18.36	161.430	157.707

4.6 Fit of the spectra

The next step of the analysis after background subtraction, acceptance correction, and extraction of the experimental cross section was a decomposition of the resulting spectra. The computer program FIT [69] was used in this procedure.

4.6.1 Decomposition of the spectrum

Figure 4.11 displays examples of the resulting double-differential cross sections as a function of the excitation energy in ^{7}He for three angular bins. The g.s. transition is resolved in all spectra. The low threshold energy (besides the already open ^{6}He(g.s.)+n channel) for α+3n decay at $E_{\mathrm{th}} = 0.53$ MeV leads to a broad distribution of strength even at low excitation energies. Two previously observed resonances in ^{7}He at $E_{\mathrm{x}} = 2.9(1)$ and 5.8(3) MeV with widths $\Gamma = 1.99(11)$ and 4(1) MeV, respectively, found in reactions [8, 9] where they provide a clear signal, are not excited selectively in the present experiment. The prominent structure around $E_{\mathrm{x}} \approx 20$ MeV was also observed in the ^{7}Li(n,p) reaction [70] and may result from an excitation of the isovector giant dipole resonance of the α cluster core in ^{7}He similar to observations in ^{7}Li [71, 72]. The ^{7}He level scheme with known resonances and with particle thresholds relevant to the present analysis is shown in Fig. 4.12. Note that ^{7}He g.s. is unbound by 0.445 MeV. Thus, resonance and excitation energies are shifted by this value relative to each other.

Inspecting Fig. 4.11, the identification of a possible additional low-lying resonance is clearly a difficult task. The first step of the analysis is a decomposition into Breit-Wigner resonances with an energy-dependent penetrability shown in Fig. 4.12 plus an additional resonance at $E_{\mathrm{x}} \approx 20$ MeV from [70]. Contributions due to the quasifree nucleon knockout reactions are also expected not only from ^{7}Li, but also due to the charge-exchange reactions on t and ^{4}He because of the pronounced cluster structure of the ^{7}Li ground state with a (^{4}He$\otimes$t) configuration. For the quasifree scattering on ^{7}Li as a whole there exists not only a distribution for the ^{6}He ground state, but also for the first excited 2^+ state. The excitation energy dependence of both processes (^{6}He(g.s.)+n and ^{6}He(2^+)+n channels) is described by the semi-phenomenological parametrization of Erell *et*

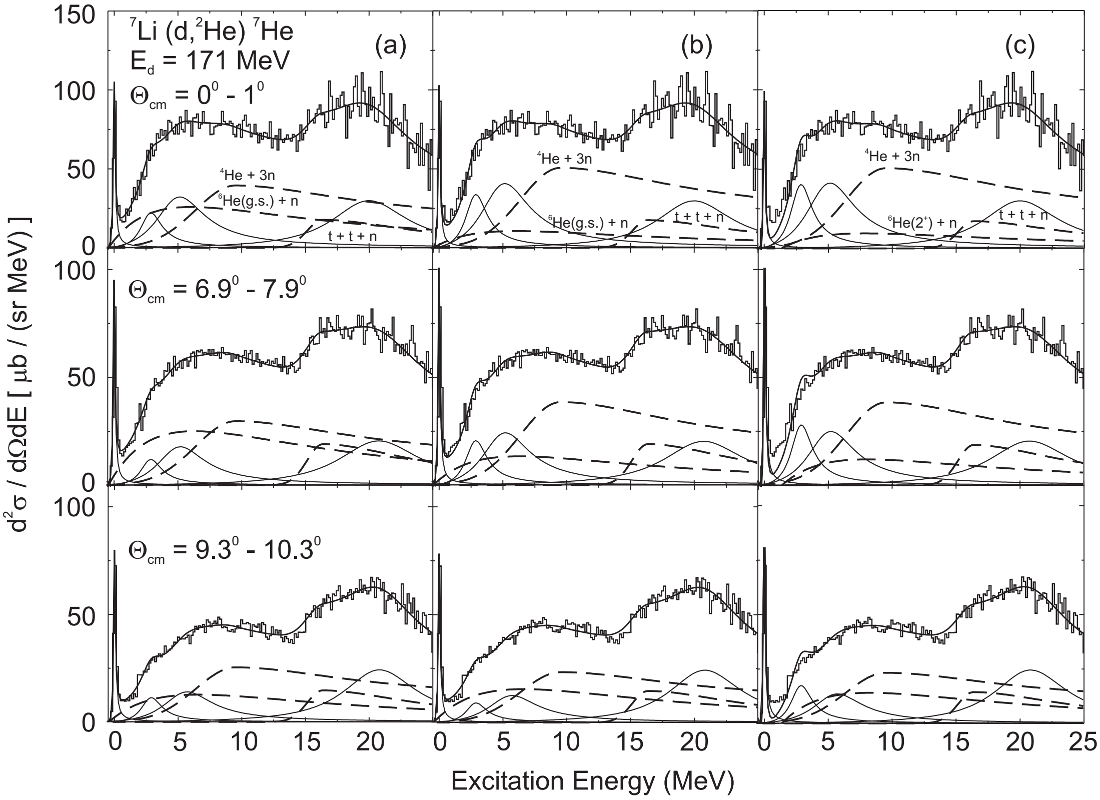

Fig. 4.11: Selected spectra of the ^{7}Li(d,^{2}He) reaction at $E_\mathrm{d} = 171$ MeV for different angular bins and their decomposition. Solid lines: experimentally established resonances and resulting fit. Long-dashed lines: background from quasifree scattering on ^{7}Li as a whole (^{6}He(g.s.) + n and ^{6}He(2$^+$) + n channels) using the model of Ref. [61], on the ^{4}He cluster in ^{7}Li (t+t+n channel) and on the triton cluster (^{4}He+3n channel) using the data from [74, 75]. (a): relative magnitudes determined by a fit to the data. (b): quasifree scattering on ^{7}Li, assuming ^{6}He(g.s.)+n channel or (c): assuming ^{6}He(2$^+$)+n channel, respectively, fixed by a measurement of the ^{6}Li(d,^{2}He) reaction.

al. [61], which has been presented in the previous Section. To determine the energy dependence of the charge-exchange reactions on the cluster components the data on the ^{3,4}He(p,n) reactions [74, 75] at momentum transfers comparable to the present case were used. The corresponding thresholds are $E_\mathrm{x} = 0.53$ MeV and $E_\mathrm{x} = 11.87$ MeV for the ^{4}He+3n and t+t+n channels, respectively. In order to apply the (p,n) results [74, 75] for the (n,p) reactions on the ^{7}Li g.s. clusters, one can employ charge symmetry. Furthermore, ^{3}He(p,n)3p represents the mirror re-

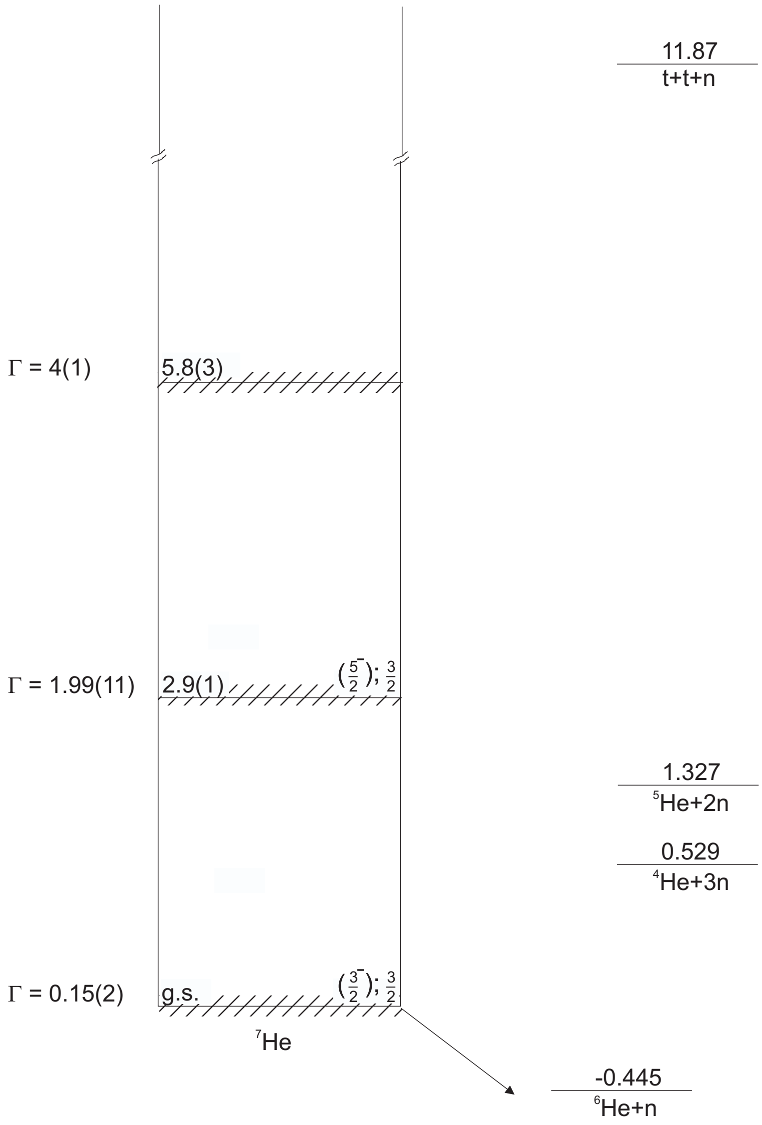

Fig. 4.12: Level scheme of the ^{7}He nucleus.

action to the required t(n,p)3n channel. In order to fit the ^{7}He spectra using these two cluster components, a standard function in the library programme FIT was chosen which describes the form of the corresponding experimental spectra [69] using a Gauss function and a polynomial of fourth order.

Returning to the ^{7}Li(d,^{2}He)^{7}He data, three different analyses of the spectra are presented in the following. The fits take into account all known resonances (g.s., 2.9 and 5.8 MeV) at low excitation energies. Their centroids and widths are allowed to vary within the experimental uncertainties [73]. Additionally, the prominent bump at ($E_\mathrm{x} \approx 20$ MeV) is described as a single resonance with the parameters deduced by [70]. Furthermore, the three quasifree background channels discussed above are included. A good description of all data can be achieved (see e.g. solid lines in Fig. 4.11). Independent of detailed assumptions about the centroid energies and widths of possible resonances at higher excitation energies, the decompositions shown in Fig. 4.11 demonstrate that they do not contribute significantly to the cross sections in the low-energy region. The same is true for background processes like the ^{4}He + 3n and t + t + n channels, which are structureless in the region of interest and slowly and smoothly increasing having maxima at much higher energies.

On the other hand, the magnitude of the ^{6}He+n contribution is the most critical aspect in the analysis of the ^{7}He spectra. In the Fig. 4.11(a) the decomposition of the spectra is shown, where the overall normalization N from Eq. (4.11) for both the ^{6}He(g.s.)+n and ^{6}He(2$^+$)+n channels is treated as a free parameter during the fit. However, the ^{6}He(2$^+$)+n part with a threshold energy E_x = 1.35 MeV is predicted to be zero in the free fit. Moreover, the resulting angular distribution of the ^{6}He(g.s.)+n channel shows considerable scattering and, in particular, a strong decrease at larger momentum transfers incompatible with the physical interpretation of the quasifree knockout process. This can be seen in Fig. 4.13, where the angular distribution of the ^{6}He(g.s.) + n quaisifree channel from the free fit [Fig. 4.11(a)] is compared with that from the decomposition constrained by the ^{6}Li(d,^{2}He)^{6}He measurement [Fig. 4.11(b)] is presented. Therefore, in an alternative analysis [Fig. 4.11(b,c)] it is assumed that the magnitude of the single nucleon knockout quasifree cross section is not changing significantly when going from ^{6}Li to ^{7}Li and therefore the overall normalization N in Eq. (4.11) thus was taken from the corresponding ^{6}Li(d,^{2}He)^{6}He data [67]. Two extreme cases are considered: the total ^{6}He+n contribution is described exclusively by the ^{6}He(g.s.)+n channel [Fig. 4.11(b)] or by the ^{6}He(2$^+$)+n channel [Fig. 4.11(c)].

4.6.2 Possible low-lying J$^\pi$=1/2$^-$ spin-orbit partner of the ground state

While the decomposition with three analyses described in previous Section shows comparable results over the wide range of the excitation energy, differences are observed in the low-energy region of the spectrum. An extended view of the

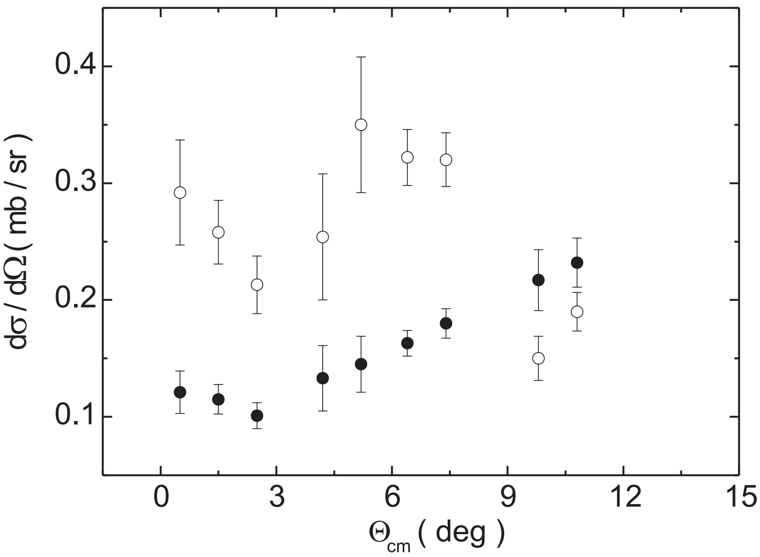

Fig. 4.13: Angular distribution of the total ^{6}He(g.s.) + n quasifree contribution derived from a free fit shown in Fig. 4.11(a) (open circles) and fixed by the ^{6}Li(d,^{2}He)^{6}He measurement shown in Fig. 4.11(b) (solid circles).

low-energy part of the $\Theta_{\rm cm} = 0° - 1°$ spectrum is plotted in Fig. 4.14(a)-(c) in comparison for the three different decompositions. The g.s. resonance and the region above $E_{\rm x} \simeq 3$ MeV are well described in all cases. However, in between the data overshoot the fit, indicating the presence of a possible further resonance. Indeed, this is not only observed at 0° but also in the other spectra, except for the largest scattering angles measured. On the other hand, inclusion of an additional resonance with $E_{\rm x} \simeq 1.45$ MeV and $\Gamma \simeq 2$ MeV provides an excellent description of the data, see Figs. 4.14(b), (c). Considering only the ^{6}He(2^+) + n channel the resonance becomes even more pronounced. For both cases the corresponding χ^2/d.o.f. improves from 2.3 to 1.7. The estimated uncertainties for the centroid energy and the resulting width of a possible additional resonance at low $E_{\rm x}$ are rather large, in particular, due to the large experimental error of the 5.8 MeV resonance width. A range of acceptable values $E_{\rm x} = (1.45^{+0.7}_{-0.5})$ MeV, $\Gamma = (2.0^{+1.0}_{-1.1})$ MeV was determined by the uncertainty of the theoretical χ^2 distribution. The systematic uncertainties of the extracted resonance parameters due to absolute normalization of the data and acceptance corrections [57] are of the order of 15%.

Assuming alternatively an additional resonance with the parameters of Ref. [6]

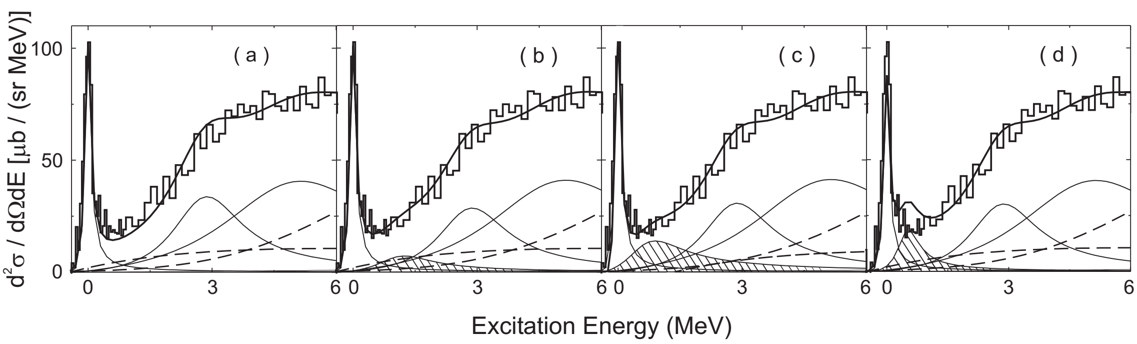

Fig. 4.14: Low-energy region of the ^{7}He spectrum obtained for $\Theta_{\mathrm{cm}} = 0^\circ - 1^\circ$ (top row of Fig. 4.11). Solid and dashed lines are the same as in decompositions (a)-(c) of Fig. 4.11. Hatched area in (b) and (c): additional low-energy resonance necessary to describe the data. (d): additional resonance assuming the parameters of [6].

and estimating the cross section at 0° from the predictions of the *ab initio* calculations discussed below leads to the poor fit shown in Fig. 4.14(d). Evidently, such a resonance should be clearly visible in the data.

As discussed in the next Section, where the B(GT) strengths extracted from the measured cross section are compared with model calculations, this low-lying resonance would be a candidate for the $J^\pi = 1/2^-$ spin-orbit partner of the ^{7}He ground state.

5 Extraction of Gamow-Teller strength

A further test of the possible evidence for a low-lying resonance in ^{7}He with the properties extracted from the data is provided by a comparison of Gamow-Teller strengths extracted from the measured charge-exchange cross sections with GFMC calculations [1]. The procedure to extract the B(GT) strength is based on its proportionality to the $\Delta L = 0$ part of the charge-exchange cross sections at momentum transfer $q = 0$ as discussed by [37] which can be extracted from an extrapolation of the measured angular distributions.

5.1 Cross section and B(GT)

In the case of vanishing momentum transfer, the (d,^{2}He) reaction proceeds through the $\sigma\tau$ part of the effective interaction. As described above in the section 2.5, the measured cross section is directly proportional to the B(GT) strength, which in the (n,p) case is [36,37]

$$\frac{d\sigma(q=0)}{d\Omega} = C\left[\left(\frac{\mu}{\pi\hbar^2}\right)^2 \frac{k_f}{k_i} N_D J_{\sigma\tau}^2 B(\mathrm{GT}^+)\right]. \qquad (5.1)$$

The scaling factor C is inserted because the (d,^{2}He) response additionally scales with the distribution of the d→^{2}He transition strength, whose detection is limited by the experimental setup. The scaling factor can be determined by comparing the (d,^{2}He) cross section with known GT strength from β decay, where available, or by using the (d,^{2}He) reaction on self-conjugate nuclei, where the GT strength is expected to be the same in both isospin directions ($B(\mathrm{GT}^-) = B(\mathrm{GT}^+)$), so that in this case, $B(\mathrm{GT}^-)$ data from (p,n) experiments can be taken as a reference. In our case an empirical normalization factor $C = 0.320 \pm 0.027$ derived from data on p- and sd-shell nuclei [76] is used for the determination of the B(GT) strengths. The volume integral of the spin-dependent isovector central part of the effective nucleon-nucleon interaction at $q = 0$ is given in [32] and amounts to $|J_{\sigma\tau}| = 165$ MeVfm^3 at $E/A = 85$ MeV. The distortion factor N_D is usually estimated by calculating the ratio of the distorted-wave (DW) and plane-wave

(PW) cross sections,

$$N_D = \frac{\sigma_{DW}(q=0)}{\sigma_{PW}(q=0)}. \qquad (5.2)$$

The PW cross sections are obtained by setting all potential strengths to zero. The cross sections are extrapolated to zero momentum transfer ($q = 0$) using the DWBA calculation,

$$\frac{d\sigma(q=0)}{d\Omega} = \frac{\sigma_{calc}(q=0)}{\sigma_{calc}(\Theta,q)} \frac{d\sigma_{exp}(\Theta,q)}{d\Omega}. \qquad (5.3)$$

This is a reliable procedure if measurements are being performed in a region close to 0°.

5.2 DWBA calculations of the angular distributions

Theoretical predictions of the angular distributions for different transitions are obtained from distorted wave Born approximation calculations employing the code ACCBA [29], which is specialized for the (d,^{2}He) reaction and applies the techniques discussed in Section 2.2. This is a semi-microscopic code that uses an effective nucleon-nucleon (NN) interaction described in Section 2.3 and shell-model wave functions (see Section 2.4). The effective NN interaction was taken from [32, 33], for which a parameter set at 85 MeV per nucleon has been extrapolated earlier [77]. The spin-orbit potential is not included. The optical-model parameters used to create the distorted waves in the incident channel were calculated from a global fit to deuteron elastic scattering up to 90 MeV [78]. They were extrapolated to the present energy of 171 MeV. However, the extrapolated parameters are identical with those of extracted from the experimental (d,d′) data measured at the same incident energy at KVI [79]. For the exit channel, the optical-model parameters have been taken from Gupta *et al.* [80]. Nuclear wave functions and one-body transition densities (OBTDs) were generated by the shell-model code OXBASH [34] as *ab initio* wave functions are still not available.

The angular distributions of the ^{7}Li(d,^{2}He) reaction populating low-lying states in ^{7}He in comparison with theoretical DWBA calculations are displayed in Fig. 5.1.

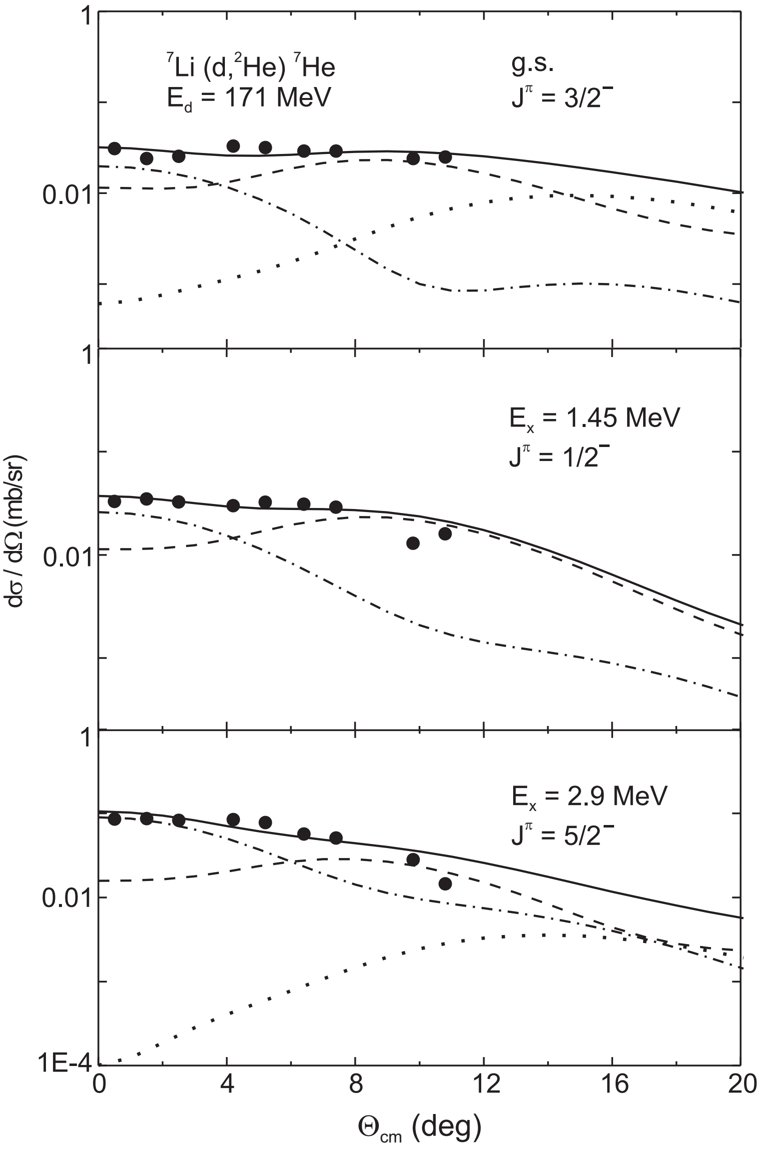

Fig. 5.1: Experimental angular distributions of the transitions to the levels at $E_{\mathrm{x}} = 0.0$, 1.45 and 2.9 MeV in ^{7}He (full circles) and DWBA calculations (solid lines) using shell-model wave functions and the Love-Franey effective projectile-target interaction [32, 33]. The dashed-dotted, dashed and dotted lines show the decomposition into $\Delta L = 0$, 2, and 4 contributions, respectively.

The data exhibit a quite unexpected behavior: while angular distributions of prominent GT transitions in charge-exchange reactions are normally strongly peaked at $\Theta_{\mathrm{cm}} = 0°$, only a weak angle dependence is visible in Fig. 5.1. In particular, the g.s. cross section angular distribution is almost constant. The cross sections at angles close to 0° are comparatively small, about 70 times weaker than the well-known $p_{3/2} \rightarrow p_{1/2}$ GT transition populated in the ^{12}C(d,^{2}He)^{12}B reaction at a comparable incident energy [77]. This strong reduction could be attributed to the dominant cluster structure of the involved nuclei. In order to separate the $\Delta L = 0$ and $\Delta L > 0$ pieces of the (d,^{2}He) cross sections we performed a systematic study testing a variety of p-shell residual interactions using the OXBASH code. Three different interactions were employed: CKPOT and CKI by Cohen and Kurath [81] and CKIHE, which is also based on the Cohen and Kurath interaction and adjusted by Stevenson and Brown [82] to different He isotopes. The predicted GT transition strengths and thus the corresponding charge-exchange cross sections differ widely, but for a given transition the shapes of the partial $\Delta L = 0, 2, 4$ DWBA angular distributions are rather insensitive to the particular choice of the interaction. Thus, the decomposition of the cross sections is determined by a fit allowing separate variation of averaged $\Delta L = 0, 2, 4$ angular distributions. Then the experimental data can be described well and the $\Delta L = 0$ fraction at $\Theta_{\mathrm{cm}} = 0°$ amounts to 62%, 68% and 85% for the levels at $E_{\mathrm{x}} = 0.0$, 1.45 and 2.9 MeV, respectively. Results obtained using any of the interactions individually agree within 5%. The impact of a reduced isovector tensor force as suggested in [77] has also been investigated. Again, the resulting $\Delta L = 0$ cross sections vary less than 5%.

5.3 Comparison with QMC calculations

The *ab initio* calculations provide a remarkably successful description of the properties of light nuclei including the transition from stable nuclei to the proton and neutron drip lines. They also reproduce the single-particle spectroscopic factor of the ^{7}He g.s. deduced from an R-matrix analysis of the present data (see Section 6 and [18]). Calculations for ^{7}Li→^{7}He GT transitions are available [83] using a variational Monte Carlo approach which precisely reproduces weak decay properties in $A = 6, 7$ nuclei [84]. Basic equations of the *ab initio* QMC calculations can be found in Section 2.6. The predictions are shown on the l.h.s. of Tab. 5.1. The deduced B(GT) values are summarized in the r.h.s of Tab. 5.1.

Tab. 5.1: Comparison of VMC model predictions and experimental excitation energies and GT transition strengths populating the lowest resonances in ^{7}He.

	VMC model		Experiment	
J^π	E_x (MeV)	B(GT)	E_x (MeV)	B(GT)
$3/2^-$	0.0	0.0039(1)	0.0	0.0044(14)
$1/2^-$	2.9(3)	0.0055(1)	$1.45^{+0.7}_{-0.5}$	0.0076(23)[a]
$5/2^-$	3.4(1)	0.0110(2)	2.9(1)	0.0252(78)

---

[a] A spectroscopic factor ratio of 1 : 3 [85] is assumed for the population of the ^{6}He(g.s.) + n and ^{6}He(2^+) + n channels.

The experimental uncertainties include statistical and systematic errors from the unit cross section normalization and the model dependence of the DWBA analysis. The experimental B(GT) value for the $J^\pi = 1/2^-$ state corresponds to a spectroscopic factor ratio of 1 : 3 for the quasifree ^{6}He(g.s.) + n and ^{6}He(2^+) + n channels taken from a shell-model prediction [85]. Going from one extreme (only ^{6}He(g.s.) + n) to the other (only the ^{6}He(2^+) + n) in the spectrum decomposition described in Section 4.6, the B(GT) strength changes from 0.0056(17) to 0.0084(26). The weakness of the GT transitions may raise some doubts about the applicability of the proportionality assumption between β decay matrix elements and 0° charge-exchange cross sections [86]. However, the comparison with the VMC predictions in Tab. 5.1 demonstrates a remarkable agreement between experiment and theory, not only for the ratio of the possible spin-orbit partners but also for the absolute values.

Finally, a comparison of experimental and theoretically predicted excitation energies for the low-energy resonances in ^{7}He can be done. The excitation energy of the $1/2^-$ state depends sensitively on the inclusion of a three-body interaction. The VMC calculation gives $E_\mathrm{x} = 2.0$ MeV. Results for various combinations of two- and three-body interactions are presented in Table XII of Ref. [23] allowing for a range of E_x values between 0.4 and 3.2 MeV. The combination of the Argonne v18 nucleon-nucleon and Illinois-2 three-nucleon interaction generally gives the best overall agreement for light nuclei [22] and the corresponding values

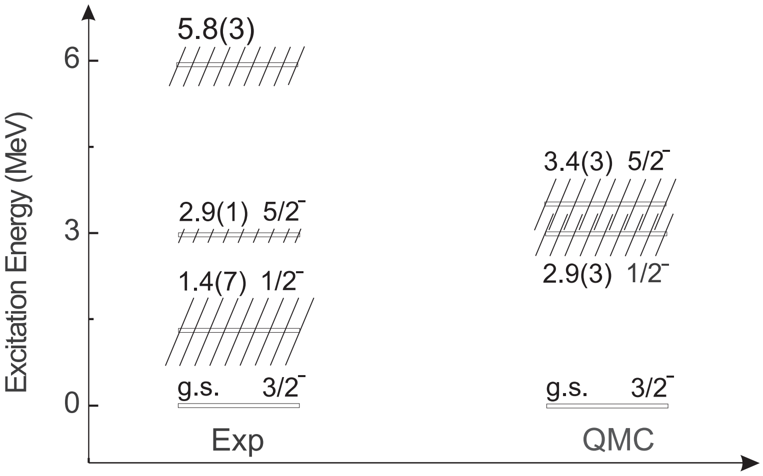

Fig. 5.2: Experimental excitation energies in ^{7}He (left) in comparison with the QMC calculated values (right). Hatched area: width of the states.

are included in Tab. 5.1. A comparison of the experimentally established and theoretically calculated excitation energies for the low-lying states in ^{7}He can be seen in Fig. 5.2. The prediction for the $1/2^-$ state is about 1.5 MeV higher than the experimental finding. Of course, if the $1/2^-$ state had an excitation energy close to the resonance at $E_\mathrm{x} = 2.9$ MeV these could not be separated in the present experiment, but the excess of cross section at low energies would remain unexplained.

6 Spectroscopic factor of the ground state

Spectroscopic factors are basic quantities characterizing the single-particle nature of nuclear excitations and therefore serve as an important test of wave functions calculated with recently developed *ab initio* methods. In particular, predictions from Green's function Monte Carlo calculations [23] are available [83] for the neutron spectroscopic factors S_n of the lowest $J^\pi = 3/2^-$ and $1/2^-$ states in ^{7}He, respectively: $S_\mathrm{n}(3/2^-) = 0.527(4)$ and $S_\mathrm{n}(1/2^-) = 0.873(6)$. It can also be compared to the classical nuclear shell-model calculations. The corresponding values within the Cohen and Kurath model [81] are 0.591 and 0.685, respectively. There are also the fermionic molecular dynamics FMD [87] calculations predicting $S_\mathrm{n}(3/2^-) = 0.53$. Using the (d,^{2}He) reaction with good energy resolution one can provide new information about the g.s. resonance parameters and then in the frame of an R-matrix analysis obtain the neutron spectroscopic factor, assuming that the $J^\pi = 3/2^-$ ground state of ^{7}He can be described as $^6\mathrm{He}\otimes\nu 1\mathrm{p}_{3/2}$ configuration. The analysis consists of two steps: subtraction of background under the resonance and deconvolution of the experimental data because of the finite energy resolution, and a single-level R-matrix analysis of the deconvoluted resonance.

6.1 Deconvolution

As already mentioned above, the ground state of ^{7}He is unbound by $E_\mathrm{r} = 0.445$ MeV with respect to the ^{6}He + n threshold [73]. The low-energy region up to resonance energy $E_\mathrm{r} = 2.5$ MeV is shown in Fig. 6.1. The spectrum is summed over the angular region $\Theta_\mathrm{cm} = 0° - 4°$ in order to obtain good statistics. The $\mathrm{J}^\pi = 3/2^-$ g.s. resonance clearly stands out. However, the experimental data show a background contribution below the resonance peak. This needs to be subtracted before applying an one-level R-matrix analysis to obtain the observed reduced width from which one can determine the spectroscopic factor.

The decomposition of the spectrum has been already discussed in Section 4.6 where three different analyses have been presented [see Figs. 4.11(a) and Figs. 4.14(b,c)].

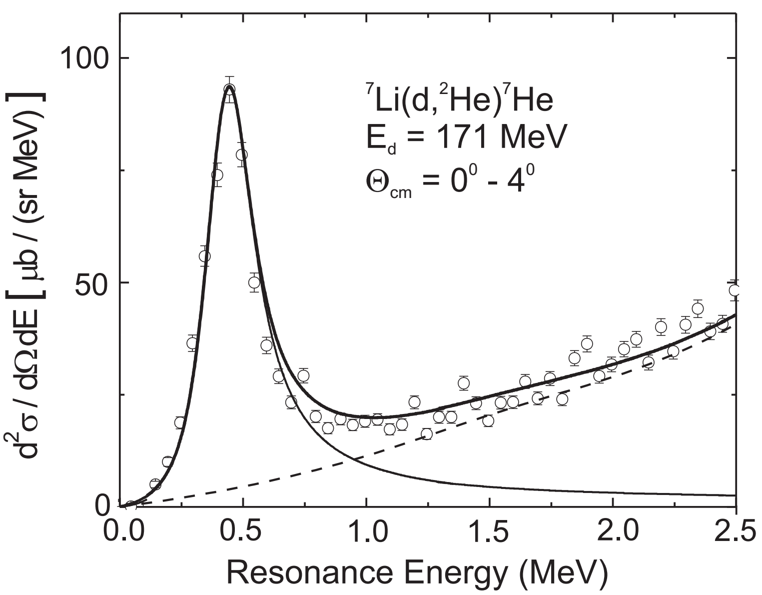

Fig. 6.1: Low-energy part of the ^{7}Li(d,^{2}He) spectrum. Dashed line: background contribution. Solid line: ground state fit function and total fit.

The dashed line in Fig. 6.1 is a sum of the resonances and quasifree channels contributions except the ground state. Here, as an example, only a case presented in Fig. 4.14(b) is shown. It is not important which analysis is used for the determination of the ratio – ground state versus the 'rest'. Moreover, the results of the analyses differ less than 2% from each other. It is clear that there is a systematical error in the fitting, in particular, due to the modelling of the ^{6}He + n quasifree scattering and experimental uncertainties of the known resonances (2.9 MeV and 5.8 MeV). Investigating the experimental limits of the parameters for both resonances the systematic error is estimated to be of the order of 10%.

The experimental energy resolution of $\Delta E \simeq 150$ keV (FWHM) requires a deconvolution of the g.s. resonance line shape. Using the spectrum as a discrete representation of the measured line shape, the problem reduces to solving a system of linear equations

$$u(E_i) = \sum_{k=-m/2}^{k=m/2} w(E_i - E_k) r(E_k) \delta E \ . \tag{6.1}$$

Here, $w(E)$ stands for the true spectral shape and $r(E)$ for the instrumental resolution function. The index i runs from 1 to $m+1$, and $\delta E = E_{m+1} - E_m$. For n measured data points $m = n - 1$. Since the $u(E_i)$ are noisy because of the

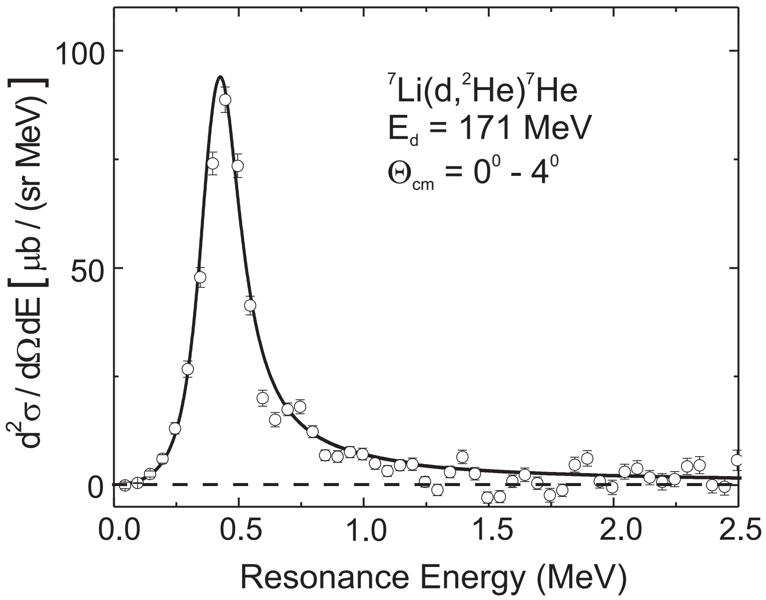

Fig. 6.2: Deconvoluted experimental cross section and fit with the R-matrix one-level resonance (solid line). The dashed line indicates zero cross section. Width of instrumental resolution function (FWHM) is 150 keV.

experimental error, the resulting system of linear equations is unstable, leading to unpredictable errors in the solutions $w(E_m)$. Stabilization might be achieved by using Tikhonov's regularization method [88, 89]. Alternatively, Eq. (6.1) can be solved by calculating the Fourier transform of the background subtracted fitted spectra and applying the Fourier convolution theorem. Since both methods are linear procedures, the results should be identical, and this was indeed observed. The Tikhonov regularization method was preferred because the input data are the noisy measured data, and the output is a set of deconvoluted noisy data which enter directly the R-matrix analysis without use of interpolating functions. The result of the deconvolution can be seen in Fig. 6.2. The fit was performed with the package 'Nonlinear Fit' [90] of Mathematica 5.1.

For the instrumental function $r(E)$ a normalized Gaussian with a width σ determined by the experiment has been used. The experimental uncertainties are dominated by variations of the experimental resolution ΔE during the experiment, which were measured to be ±10 keV. For this purpose the ^{12}C(d,^{2}He)^{12}B measurements were performed. The energy resolution was determined from the ^{12}B ground state. The resulting true width of the g.s. resonance of ^{7}He can be determined from the deconvoluted spectrum with the result Γ = 183(22) keV (FWHM). This value is considerably larger comparing with Γ = 150(20) keV from the literature [73].

6.2 *R*-matrix analysis

The *R*-matrix analysis procedure is described in details in Section 2.7. Table 6.1 summarizes results for E_{res}, γ^2_{sp}, γ^2_{obs} and the extracted spectroscopic factor S_n at representative values of the channel radius r_{match}. Results are presented for the estimated range of the instrumental energy resolution FWHM = 140 - 160 keV, and for three different matching radii r_{match} in the vicinity of the optimal one, r_{match} = 4.0 fm. The r_{match} varied between 3.5 fm and 4.5 fm in order to estimate the dependence of the results on the choice of the Woods-Saxon potential parameters. Using the optimal matching radius and averaging the results for the different estimated experimental resolutions with equal weight, one obtains as the result of the analysis for the ^{7}He ground state spectroscopic factor S_n = 0.64 ± 0.09 which is slightly larger than the GFMC and FMD predictions but agrees within uncertainties with a shell-model calculation based on the Cohen

Tab. 6.1: Results of the *R*-matrix analysis of the deconvoluted experimental cross section in the reaction ^{7}Li(d,^{2}He)^{7}He: resonance energy (E_{res}), single-particle (γ^2_{sp}) and observed (γ^2_{obs}) reduced widths, and neutron spectroscopic factor (S_n) for representative values of the channel radius r_{match}. The quoted errors result from the experimental uncertainties.

r_{match} (fm)	E_{res} (MeV)	γ^2_{sp} (MeV)	γ^2_{obs} (MeV)	S_n
3.5	0.442	2.951	1.767(20)	0.60(9)
4.0	0.442	1.748	1.145(13)	0.64(9)
4.5	0.442	1.187	0.802(9)	0.67(9)

and Kurath interaction.

Thus, the result suggests a large s.p. spectroscopic factor of the ^{7}He ground state. As a consequence, the ground state of ^{7}He can be considered as a predominantly single-particle neutron state.

7 Continuum structure at higher energies

Clustering in light nuclei has an important influence on their structure. As a possible building block an α - particle is considered because of its stable and inert behaviour due to the strong binding of two protons and two neutrons. Typical examples are ^{8}Be, which has an $\alpha - \alpha$ dinuclear molecular structure in the ground state and low-lying excited states, and ^{12}C which has been identified as a many-cluster 3-α structure. There are also systems which can not entirely decomposed into α - particle subunits, for example ^{6,7}Li posses α+ d and α+ t cluster structures, respectively. The experimental signatures of cluster states have been traditionally investigated by selective excitation in α - transfer reactions.

For the ^{7}Li(d,^{2}He)^{7}He reaction studied here, it means that there are excitations possible not only due to the charge-exchange reaction in ^{7}Li as a whole, but also due to the intrinsic excitations of the clusters itself, in the present case an α - particle and tritium. Two contributions from clusters in the ^{7}He excitation spectra are thus expected from charge-exchange quasifree reactions, occurring either on a proton of the ^{4}He or on the proton of the tritium. This corresponds to the α+ 3n and t + t + n channels in Fig. 4.11, with the threshold energies $E_{\mathrm{x}} = 0.53$ MeV and $E_{\mathrm{x}} = 11.87$ MeV, respectively. Using data from Refs. [74, 75] one can successfully describe the experimental spectra (see Section 4.6).

Another possible excitation of the α - particle in ^{7}Li is the resonance structure at $E_{\mathrm{x}} = 20.2^{+0.9}_{-1.2}$ MeV excitation energy with a width $\Gamma = 7.3^{+0.6}_{-0.3}$ MeV (Fig. 4.11) which was already observed in other charge-exchange reactions [70–72]. Yamagata *et al.* [71] searched for an excitation of an α - cluster, namely, the isovector giant dipole resonance (GDR) of ^{4}He in ^{7}Li by using the ^{7}Li(p,p$'$) reaction at 300 MeV and the analog of the GDR of the α - cluster in ^{7}He by the ^{7}Li(^{7}Li,^{7}Be) reaction at 455 MeV [72]. The data, as mentioned above, suggest that the resonance at $E_{\mathrm{x}} \approx 20$ MeV is a candidate for the GDR in an α - cluster. The excitation energy and the width of the resonance observed in nuclear reactions like (^{7}Li,^{7}Be), (n,p), (d,^{2}He) is very similar to those for the GDR in ^{4}He observed in the ^{4}He(γ,n) data [91]. All reactions mentioned above are selective for isovector excitations with spin-transfer $\Delta S = 0$ and $\Delta S = 1$, whereas the (d,^{2}He) reaction has a pure

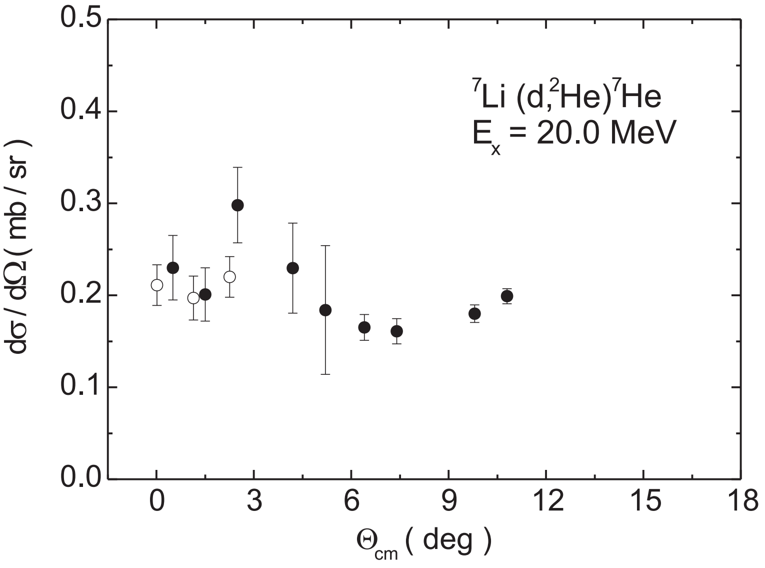

Fig. 7.1: Experimental angular distribution of the transition to the level at $E_{\mathrm{x}} =$ 20.0 MeV in ^{7}He from the present experiment (full circles, error bars are statistical only) in comparison with data (open circles) from Ref. [72].

spin-flip ($\Delta S = 1$) character. The GDR can be excited via both spin-flip and non-spin-flip transitions although non-spin-flip parts usually dominate. In the recent work of Ref. [72] it was reported that the investigated higher-lying resonance in ^{7}He is assigned to the dipole resonance with spin-transfer components $\Delta S = 0$ and $\Delta S = 1$. The contribution of each component is found to be approximately the same. This means that in the ^{7}Li(d,^{2}He)^{7}He only the $\Delta S = 1$ part of the GDR is observed, because of the selectivity of the reaction. In Fig. 7.1 remarkable agreement is observed comparing the differential cross sections of the $E_{\mathrm{x}} \approx 20$ MeV resonance structure from present (d,^{2}He) data with the $\Delta S = 1$ cross sections measured in the (^{7}Li,^{7}Be) reaction [72]. The angular distributions of the prominent structure at $E_{\mathrm{x}} \approx 20$ MeV (full circles in Fig. 7.1) is flat and almost constant over the whole angular range available in the present experiment. No conclusion about the spin is possible, because such an behaviour can be described with any combination of the partial ΔL = 1 and ΔL = 3 DWBA angular distributions for $J^\pi = 1/2^+$, $3/2^+$, $5/2^+$ (assuming a GDR excitation).

To summarize, the broad structure at high excitation energies in ^{7}He consists of two parts, both attributed to excitations in the α - cluster. As already mentioned, the first one results from the quasifree knockout reaction in ^{4}He which leads to the t + t + n channel [74, 75] with a centroid at E_x = 16.4 MeV and the second resonance at about 20 MeV is interpreted as an analog of the giant dipole resonance [70–72] in the α - cluster.

8 Summary and outlook

A search for the $p_{1/2}$ spin-orbit partner of the ^{7}He ground state has been performed utilizing the properties of GT transitions selectively excited in the ^{7}Li(d,^{2}He)^{7}He reaction at zero degrees. The data do not support a narrow $1/2^-$ resonance at $E_x = 0.56(10)$ MeV as claimed by Meister *et al.* [6], in agreement with conclusions of Refs. [11, 12]. However, contrary to [11] the present results suggest a resonance with parameters $E_\mathrm{x} = (1.45^{+0.7}_{-0.5})$ MeV, $\Gamma = (2.0^{+1.0}_{-1.1})$ MeV partially overlapping with the range of possible parameters deduced in [12] and as well as those in [14]. A decomposition of the spectrum is performed taking into account known resonances and quasifree charge-exchange reactions on ^{7}Li as well as on triton and ^{4}He clusters in the ^{7}Li ground state. As discussed in detail in Chapter 4, this finding depends sensitively on the modelling of the ^{6}He + n quasifree scattering contribution to the spectra. The choice of the parametrization described in [61] is justified by the good description of an analogous measurement of the ^{6}Li(d,^{2}He)^{6}He reaction in a kinematical regime where the quasifree cross sections dominate.

The B(GT) strengths to the lowest states in ^{7}He, extracted from the 0° cross sections after a decomposition of the spectra including this additional resonance, are in excellent agreement with Quantum Monte Carlo calculations. Further tests of these results may be provided by studies employing the (d,p) reaction with a radioactive ^{6}He beam [10, 15]. Also, alternative theoretical approaches like the Gamow shell model [92–94] or fermionic molecular dynamics [87] may help to clarify the question of the p-shell spin-orbit splitting in ^{7}He.

Using the present measurement of the ^{7}Li(d,^{2}He)^{7}He reaction with good energy resolution, the neutron single-particle spectroscopic factor S_n of the ^{7}He ground state was extracted by an R-matrix analysis. The width that results from the deconvolution of the spectrum is $\Gamma = 183(22)$ keV (FWHM). The spectroscopic factor obtained from the experimental data is in agreement with predictions from Cohen and Kurath but slightly larger than recent *ab initio* Green's function Monte Carlo calculations of Pieper and Wiringa as well as those from fermionic molecular dynamics model.

Physics of exotic nuclei is a very intriguing branch of modern physics. The recent development of radioactive beam facilities and theoretical methods has opened new perspectives in the investigation of the peculiar properties of drip-line nuclei. The exploration of the extreme regions of the mass table is just at the beginning and much remains to be discovered.

PART II:
Measurement of the Deuteron Electrodisintegration under 180° at the S-DALINAC

9 Introduction

Primordial nucleosynthesis (Big-Bang Nucleosynthesis, BBN) provides a test of cosmological models and constrains cosmological key parameters, such as average density of matter in the universe, baryon density, number of light neutrino species etc. [95]. The Standard Big-Bang model of cosmology is the simplest, based on the observed large-scale isotropy and homogeneity of the universe. Cosmological models can be tested by comparing predicted light element abundances with observed abundances. It is known, that primordial nucleosynthesis created only the first three light elements: hydrogen, helium and lithium. No elements heavier than beryllium were produced because there is no stable nucleus with 8 nucleons, so there was a bottleneck in the nucleosynthesis, that stopped the process there. The synthesis of the light elements (D, ^{3}He, ^{4}He and ^{7}Li) is determined by events occurring in the times from $t \approx 1$ to $t \approx 1000$ s in the history of the universe when temperatures went down from $T \approx 1000$ K or higher to $T \approx 100$ K. A small part of the reaction network of the primordial nucleosynthesis is shown in Fig. 9.1. As is shown, the nucleosynthesis chain begins with the formation of deuterium in the p(n,γ)d reaction which is known to create all deuterium in the early universe. The cross section of this process is necessary to estimate the production yields of primordial light elements. Deuterium (D) abundance provides direct information on the baryon density in the early universe, what makes D a perfect 'baryometer' [96–98]. However, deuterium is fragile and is destroyed in stars even before they reach the main sequence. Thus, local measurements, where probably about 50% of the material has been through stars, do not directly reflect its primeval abundances. The important synthesis-reaction p(n,γ)d takes place at $T < 0.3$ MeV, when the photodestruction rate is lower than the production rate. Knowing accurately the n-p capture cross section and using the experimental value for the primeval deuterium number density would allow for an accurate

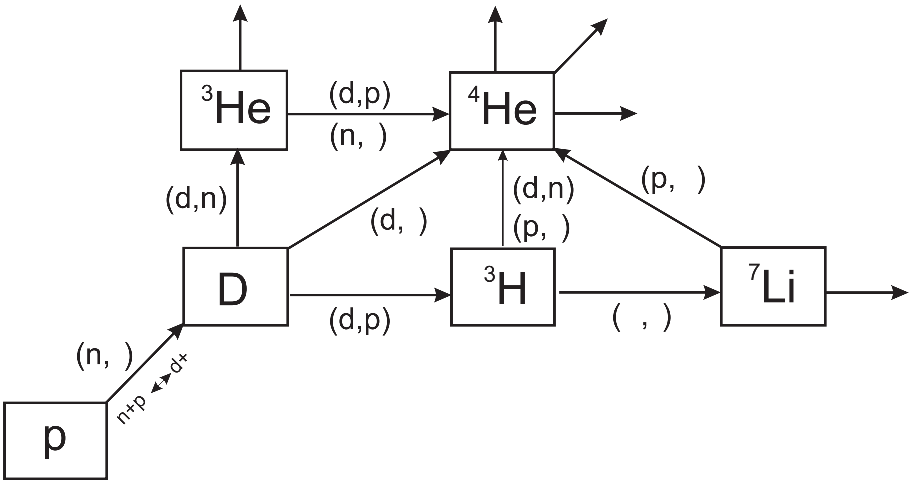

Fig. 9.1: Part of the reaction chain in Big-Bang Nucleosynthesis from [95].

determination of the baryon density $\Omega_B h^2$ (h is the Hubble constant in units of 100 km s^{-1} Mpc^{-1}).

With the baryon density at hand one can predict the abundances of the other three light elements. As an example, Fig. 9.2 displays the contribution of various primordial processes to the total uncertainty of the primordial ^{7}Li abundance. The largest uncertainty is associated with the p(n,γ)d reaction. The n-p capture cross sections have been measured at thermal energies [99, 100], at 270 keV in the center of mass (c.m.) and above, whereas in the Big-Bang energy region (20-200 keV n-p c.m. equivalent energies) measurements have not been performed, because neutron beams with low energy spread are not available.

The n-p capture cross section can also be inferred via *detailed balance* from deuteron photodisintegration experiments by using the γ-d cross section. The γ-d cross section is easier to measure with high accuracy than the n-p process itself. Thus, the experimental information obtained form the γ-d reaction in the threshold energy region provides parameters used in evaluations of nucleosynthesis in the early universe. Experimentally, the γ-d process has been recently studied using quasimonoenergetic gamma-rays produced via laser-Compton backscattering [101, 102] for photon analyzing power measurements in the energy range between 2.39 and 4.05 MeV. The $\gamma d \to np$ cross sections measured at the energies relevant to the BBN in several experimental works [103–107] are summarized in Fig. 9.3 together with recent theoretical calculations [108] within the framework of effective field theory (EFT). Here, the result of the total theoretical cross

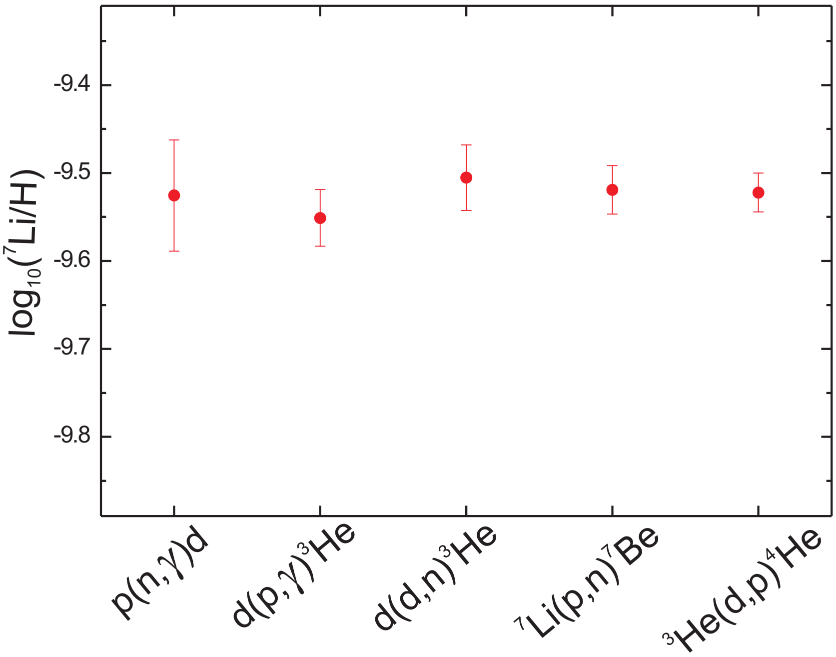

Fig. 9.2: Uncertainties in the predicted ^{7}Li abundance from the individual reactions; from Ref. [96].

section is shown as solid line, and also separately the contributions from the M1 (dashed) and E1 (dotted) transition amplitudes. There also exists theoretical calculations within the nucleon-nucleon potential model [109]. As one can see from the Fig. 9.3, there are no data available at the energies below 2.3 MeV. It is also important to emphasize that the contribution of the magnetic dipole (M1) dominates over the electric dipole (E1) in the threshold energy region.

Very recent work of Nakayama [110] reports about a measurement of the charge-exchange ^{2}H(^{7}Li,^{7}Be) reaction at 0° with an energy resolution of $\simeq$800 keV (FWHM) to deduce the distribution of the B(M1) reduced transition strength for the photodisintegration of the deuteron. However, it is necessary to measure the M1 γ-d cross section in greater detail with good energy resolution to improve the uncertainties in the BBN model predictions.

The first excited state (E_x = 2.2 MeV) of the deuteron is unbound by a few hundred keV only and is excited from the ground state predominantly through an isovector spin-flip M1 transition. Previous photodisintegration experiments focused on the angular distributions as a method of extracting the relative E1 and M1 contributions. However, these distributions are most sensitive to the M1

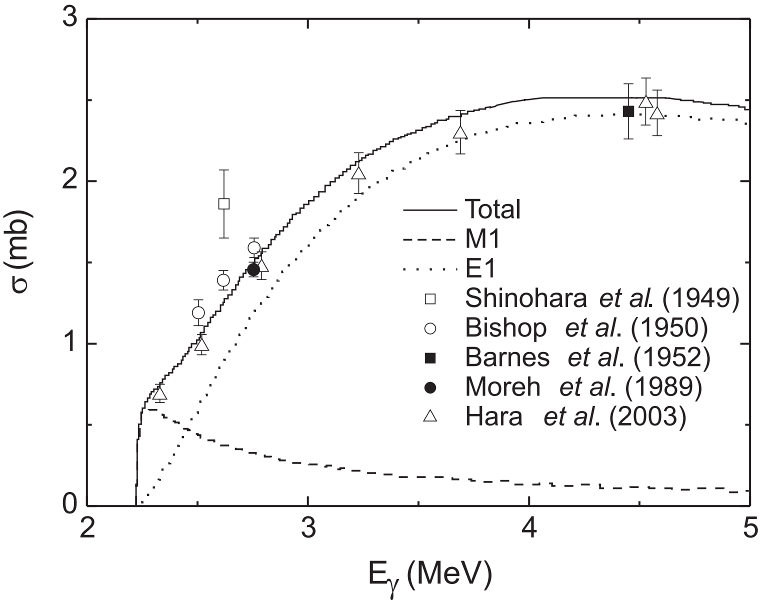

Fig. 9.3: Total cross section for the $\gamma d \rightarrow np$ process. The experimental data are from [103]: open squares, [104]: open circles, [105]: filled squares, [106]: filled circles and [107]: open triangles. Dashed and dotted curves in the theoretical EFT calculations [108] represent the M1 and E1 contributions to the total cross section (solid line), respectively.

contribution near 0° and 180°, where the measurements are difficult. Some earlier electron scattering works [111, 112] at 180° have been performed to study deuteron magnetic dipole desintegration at low-momentum transfer. These results are summarized in Fig. 9.4. The triangles and circles show the ^{2}H breakup spectrum measured with an electron initial energy of 41.5 MeV [111] and 56.4 MeV [112], respectively. However, as one can see from the figure, the resolution was relatively low (not better than 200 keV).

The system for 180° electron scattering at the superconducting Darmstadt electron linear accelerator S-DALINAC [113] is an ideal place to measure the M1 breakup cross section with good energy resolution. At 180° the transversal contribution to the electron scattering cross section remains finite, whereas the longitudinal part vanishes, greatly suppressing the background and increasing the sensitivity for transverse transitions. Thus, electron scattering at 180° serves as a 'spin filter' so that magnetic transitions, which are of purely transverse nature, are strongly enhanced while the elastic radiative tail is largely suppressed [114].

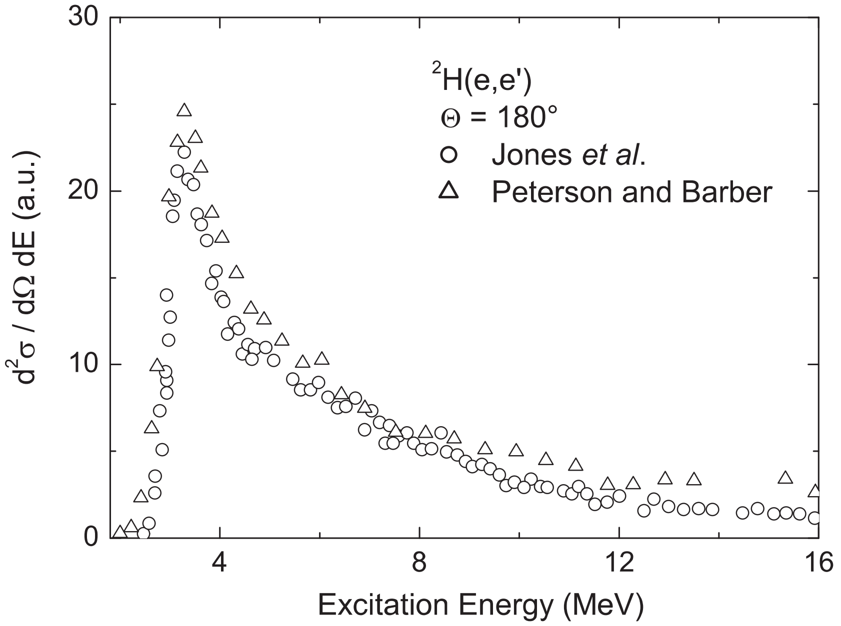

Fig. 9.4: Deuteron electrodisintegration spectra at 180° for $E_0 = 41.5$ MeV [111] (triangles) and for $E_0 = 56.4$ MeV [112] (circles).

The second part of the present work is structured as follows. Information about experimental techniques is provided in Chapter 10. Chapter 11 gives an overview of the data analysis, presents the experimental findings and a comparison of the experimental cross sections with theoretical calculations. In Chapter 12 a short summary and outlook are given.

10 Experimental procedure

10.1 S-DALINAC

The superconducting Darmstadt electron linear accelerator S-DALINAC is in operation at the Institute for Nuclear Physics of Darmstadt Universiy of Technology since 1991 [113]. It is used for experiments on nuclear and radiation physics with energies between 2.5 and 120 MeV. The electrons are emitted from a cathode and then accelerated electrostatically to an energy of 250 keV. The required time structure of the electron beam for radio-frequency acceleration in a 3 GHz field is prepared by a chopper/prebuncher system operating at room temperature. The superconducting injector linac consists of one 2-cell, one 5-cell, and two standard 20-cell Niobium structures, cooled to a temperature of 2 K by liquid helium. When leaving the injector, the beam has an energy up to 10 MeV and can be used for nuclear resonance fluorescence experiments [115]. Alternatively it can be bent by 180°, and injected into the main accelerator section. This superconducting linac has eight 20-cell cavities which provide an energy gain of up to 40 MeV. After passing through the main linac the electron beam may be extracted towards the experimental hall or it can be reinjected twice into the main linac using two separated recirculating beam transport systems. After acceleration the electron beam is delivered to several experimental facilities, schematically shown in Fig. 10.1. A wide range of electron scattering experiments is carried out using a large solid angle and momentum acceptance magnetic spectrometer of QCLAM type [116] or with a high-resolution magnetic spectrometer of energy-loss type [117, 118].

10.2 QCLAM spectrometer and 180° facility

The 180° system was brought into operation in 1994 [119, 120]. Compared to previous 180-degree systems the present device shows a number of exceptional features: a very large momentum acceptance; the ability to reconstruct both horizontal and vertical components of the scattering angle for each event, which

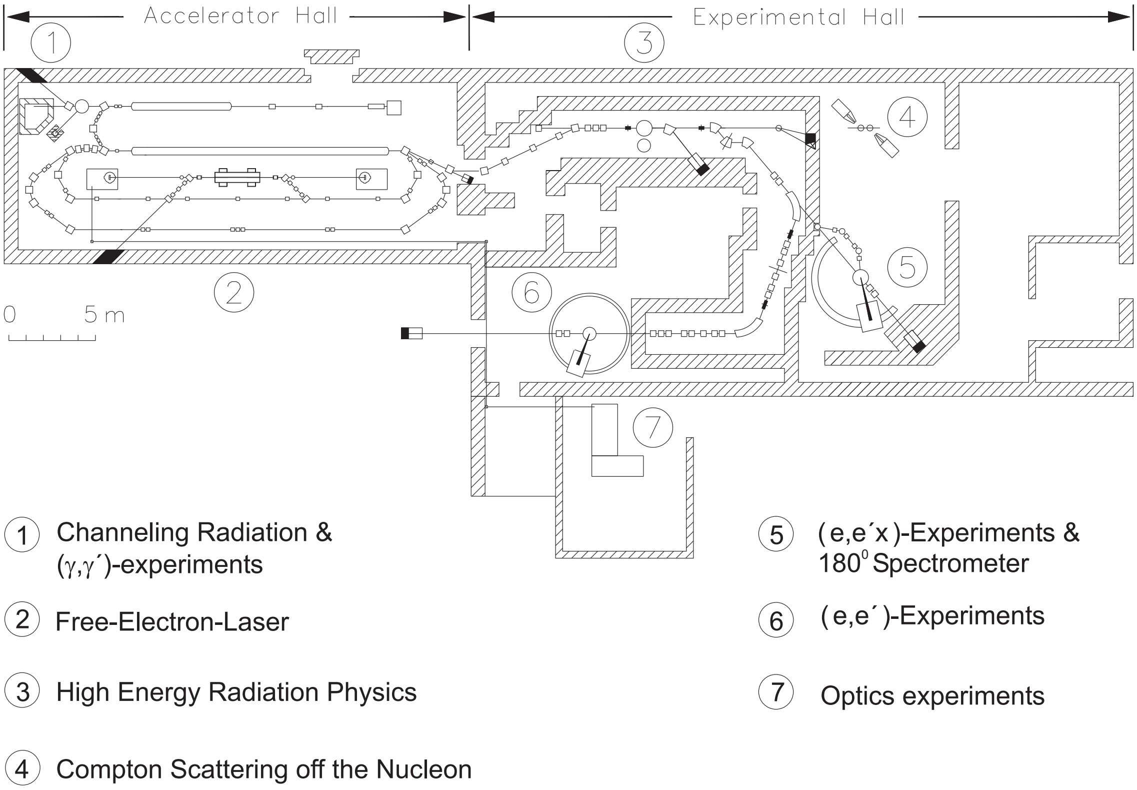

Fig. 10.1: The superconducting Darmstadt electron linear accelerator S - DALINAC with experimental facilities.

allows both the definition of solid angle and the ability to check the angular alignment; a large solid angle acceptance which may be reduced by software cuts in the data analysis. The QCLAM spectrometer [116] consists of two elements: a clamshell-type dipole magnet with a deflection angle of 120° and a quadrupole magnet which provides additional transverse focusing to increase the solid angle acceptance. The magnetic spectrometer is coupled to a scattering chamber through a sliding seal. This allows one to vary the angle between 25° and 155° without breaking the vacuum. Thus, the angular distributions of the electrons can be measured.

The properties of the 180° system can be summarized as follows

- maximum central momentum 95 MeV/c
- momentum acceptance ±10%
- horizontal opening angle ±60 mrad

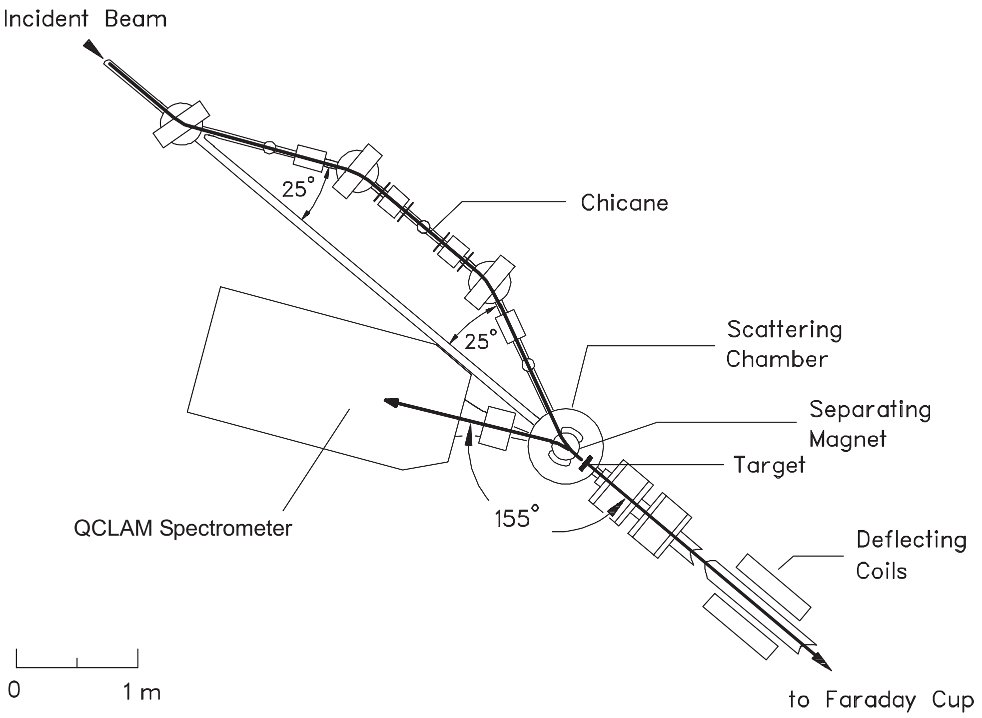

Fig. 10.2: Schematic view of the 180° facility

- vertical opening angle ±40 mrad
- solid angle 9.6 msr
- intrinsic momentum resolution 2×10^{-4}.

The Darmstadt 180° system is illustrated in Fig. 10.2. The first part is a chicane consisting of three magnets with circular poles. Each magnet bends the incident beam by 25°. The most important part of the beam transport in 180° mode is a 'separation magnet', located in the center of the scattering chamber between target and spectrometer. The 'separation magnet' deflects the beam back to its original direction and onto the target. The target is shifted 16.5 cm downstream from the center of the scattering chamber. Backscattered electrons are deflected by the 'separation magnet' to a finite angle where the spectrometer is placed. After traversing the target, the beam travels to a Faraday cup, where the electron beam current is integrated to determine the number of incident electrons. In order to refocus the beam after multiple scattering in the target, a quadrupole doublet is located immediately downstream of the scattering chamber. The quadrupole magnets are mounted on rails so that their position can be easily adjusted.

The focal-plane detection system [121] consists of three multi-wire drift chambers, a thin plastic scintillation counter and a plexiglass Cherenkov detector. Two drift chambers, X1 and X2, measure the position in the dispersive direction (x direction) and intersection angles. The wires in the third chamber (Y chamber) are rotated by 26.6° with respect to the wires in X1 and X2 so that it is also possible to determine intersection points in nondispersive direction. These data allow a complete reconstruction of scattering angle and excitation energy. The scintillator is serving as a trigger detector and a Cherenkov detector is used for the background suppression.

10.3 Experiment

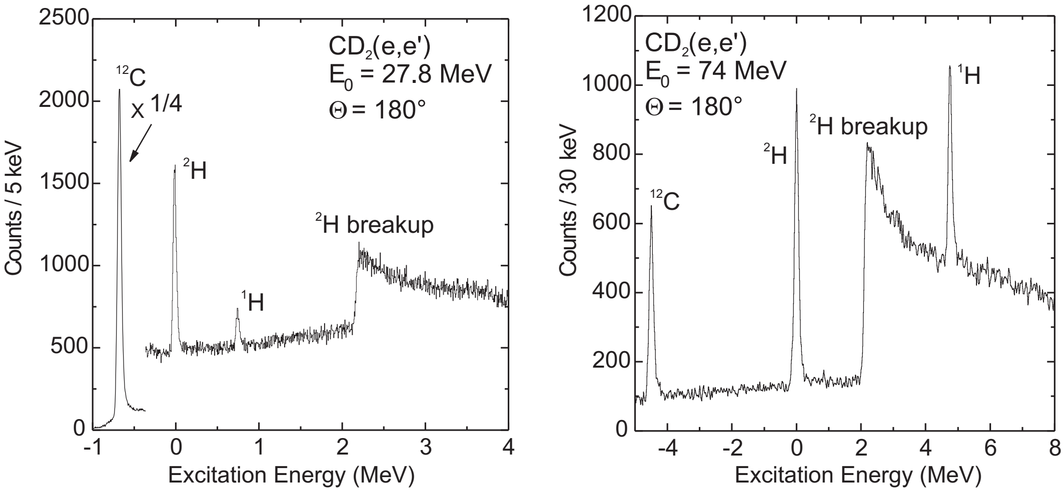

Fig. 10.3: Examples of raw CD_2(e,e′) spectra measured at 180° at $E_0 = 27.8$ MeV (left) and $E_0 = 74$ MeV (right).

For the measurements polyethylen foils enriched to 98% D_2 with different thicknesses between 4.8 to 9.6 mg/cm^2 were used. The elastic lines of H, D and ^{12}C are well separated in the spectrum by their respective recoil energies. Examples of raw spectra are shown in Fig. 10.3. Data were taken for electron energies $E_0 = 27.8(1)$ MeV and 74.0(1) MeV corresponding to momentum transfers $q = 0.28$ fm^{-1} and 0.73 fm^{-1}. The spectrometer setting covered an excitation energy range $E_\mathrm{x} \approx 0$ - 5.0 MeV at $E_0 = 27.8(1)$ MeV and $E_\mathrm{x} \approx 0$ - 12.5 MeV at 74 MeV. The energy resolution was $\Delta E \approx 45$ keV (FWHM) at lower electron beam energy and $\approx$ 140 keV at 74 MeV incident electron energy. It was limited by the target thickness and energy spread of the beam. Typical beam currents were 80 - 250 nA. At higher currents (200-250 nA) a special target holder [122] was used. This was necessary because the deuterium foils may evaporate and be destroyed rapidly if they get too hot in the area of the beam spot. The target moved with a velocity of few hundred rotations per minute both horizontally and vertically reproducing a Lissajous figure on an area of 0.8×0.8 cm^2. Also a ^{12}C target and an empty frame were put into the beam regularly. The ^{12}C measurement served for the energy calibration. With the empty-frame measurement instrumental background was controlled.

11 Results and discussion

11.1 Analysis of the spectrum

The following data analysis deals only with measurements performed with incident electrons having an energy of 27.8 MeV. Data obtained at an incident electron energy of 73.5 MeV will be analyzed in future.

An essential point for the success of the present experiment is the suppression of the instrumental background. For this purpose a 20 MHz pulsed beam was employed to distinguish between the electrons scattered off the target from those of background sources (e.g. the Faraday cup or slit systems) by time-of-flight (TOF) measurements. A macrostructure with a width of about 2 ns and repetition rate of 20 MHz is imprinted on the usual 3 GHz time structure.

With this technique the signal-to-background ratio in the measured spectra could be increased by up to an order of magnitude [123, 124]. Figure 11.1 presents a sample spectrum of counts versus time of flight. The peak from the target is

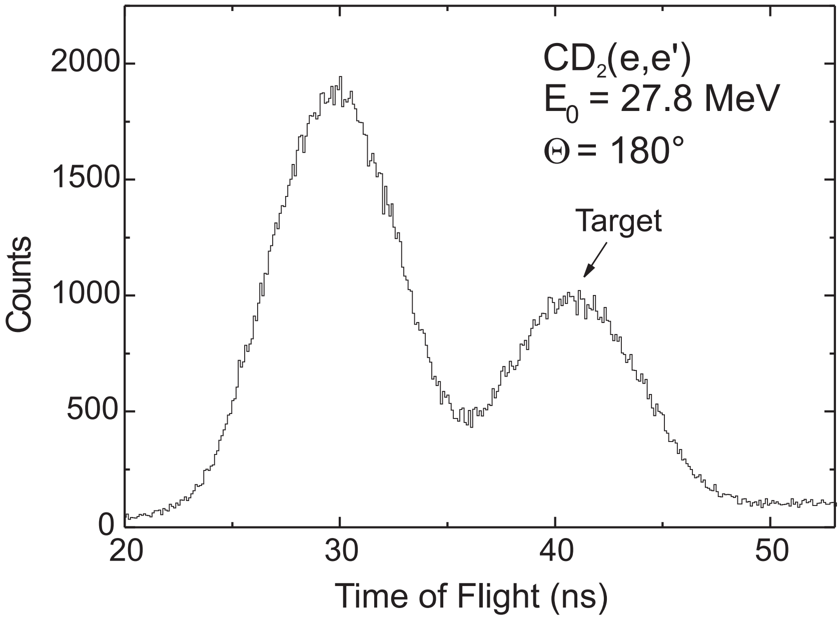

Fig. 11.1: Time of flight spectrum of the CD_2(e,e′) measured at $E_0 = 27.8$ MeV at 180°.

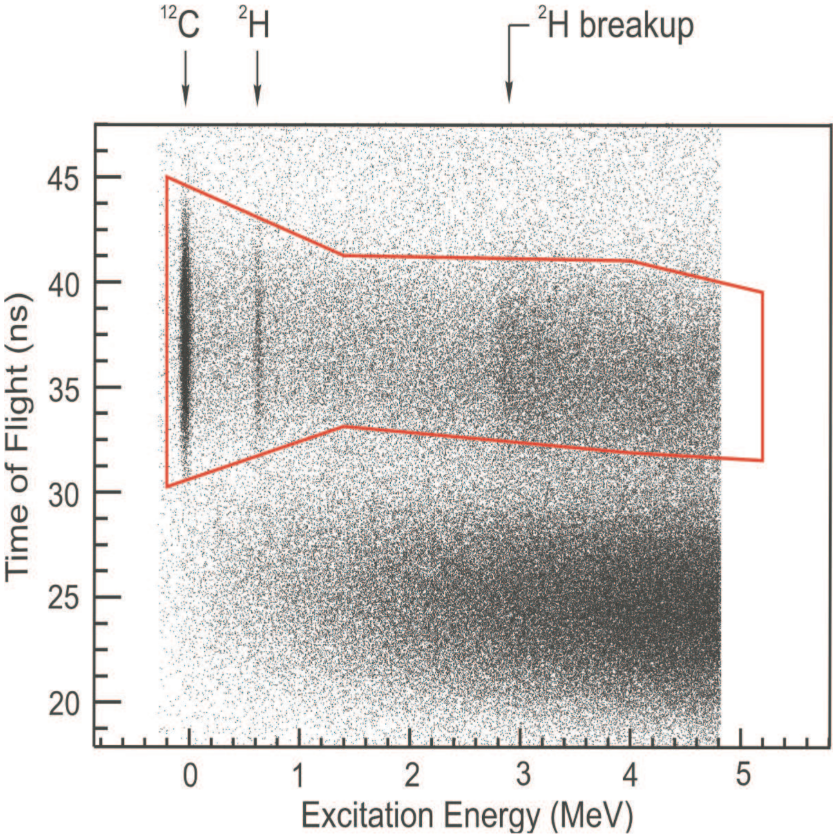

Fig. 11.2: Two-dimensional time-of-flight spectrum and a software cut applied to the data (solid line).

visible around 40 ns and can be identified by putting an empty target into the beam. An additional broad peak at about 30 ns results from different background sources. Individual sources cannot be resolved with the present time structure and resolution. According to previous investigations [123,124], however, the main contributions come from the Faraday cup, the chicane, refocusing quadrupole magnets and the slit system. With an electronic window on the target-related events, the background is already reduced considerably.

Further improvement of the time resolution is achieved by correcting for the path-length differences through the spectrometer. This technique allows one to make more accurate time gates without contributions from nearest to the target background sources. They are stemming from electrons scattered off the poles of the separating magnet and from the back wall of the scattering chamber surrounding the beam line exit. Figure 11.2 shows a typical histogram of time of flight versus excitation energy. To produce the histogram, gates on the vertical and horizontal angles are taking into account, the corresponding procedure is described further below. Making here a two-dimensional software cut on the true events the background could be reduced by a factor of 5 in the present experiment.

Figure 11.3 depicts as an example a spectrum without (upper) and with (lower) software cuts on the correct time of flight. Only a fraction of the background remains, partly due to the radiative tails of the elastic lines; this illustrates the advantage of 180° electron scattering.

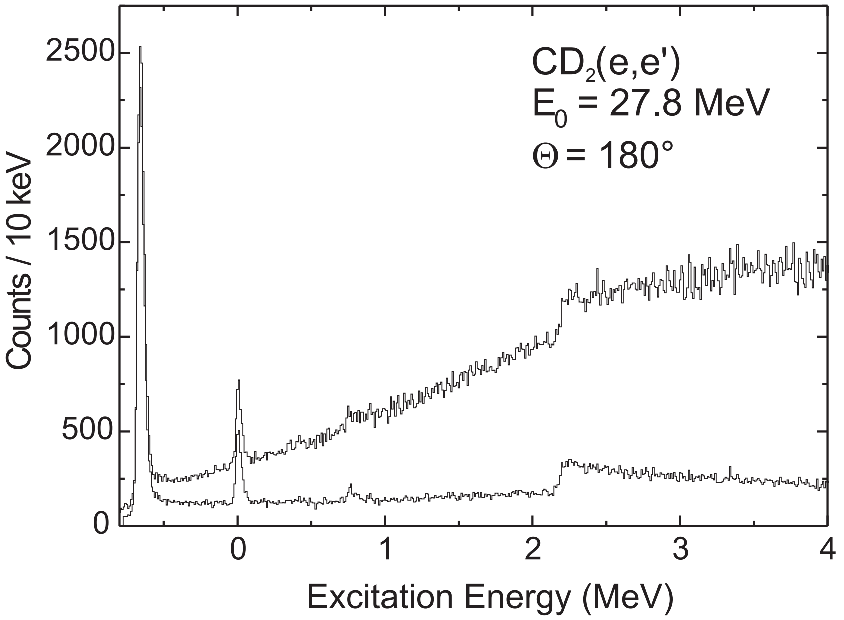

Fig. 11.3: Spectrum of the $CD_2(e,e')$ reaction at 180° without (top) and with (bottom) time-of-flight corrections.

The intersection points and the intersection angle in the focal plane of the spectrometer are defined using a method developed in [121,125]. The relative momentum deviation $\Delta p/p_{cent}$, the horizontal (Θ_H) and the vertical scattering angle (Θ_V) can be determined from these parameters and are used to obtain the excitation energy by the relation

$$E_{\mathrm{x}} = E_0 - c \cdot p_{cent} \left(\frac{\Delta p}{p_{cent}} \right) - T_{rec} - \Delta E_{Target}, \tag{11.1}$$

where E_0 is the beam energy, T_{rec} is the recoil energy and ΔE_{Target} is the energy loss in the target. The momentum of electrons on the reference trajectory through the spectrometer p_{cent} is defined by the magnetic field of the spectrometer dipole magnet. During the experiment the field is read out with a Hall probe with a relative accuracy of 1×10^{-4} and is controlled by measuring the current in the dipole magnet. The beam energy E_0 can be determined from the accelerator settings with an accuracy of only ±500 keV. Thus, E_0 is reconstructed from the position of the elastic line or prominent nuclear excitations with known excitation energy in the spectrum.

In the 180° mode the vertical scattering angle is basically limited by the gap of the separation magnet. Thus, within $\Delta p/p = 10\%$ the vertical acceptance is almost independent of the relative momentum deviation. In the right part of Fig. 11.4 counts are presented as a function of the vertical angle. The cross section, which is dominated by the elastic scattering on ^{12}C, is minimal at an angle 180°. An excitation energy cut applied here for the ^{12}C elastic line was less than 100 keV. The decrease for vertical angle smaller than 177° and larger than 183° shows the acceptance limits due to the above mentioned finite aperture of the separation magnet. Only counts inside the angular region 177° - 183° were used in the analysis. The asymmetry appears because of a coupling of the vertical angle acceptance to the horizontal scattering angle due to dispersive properties

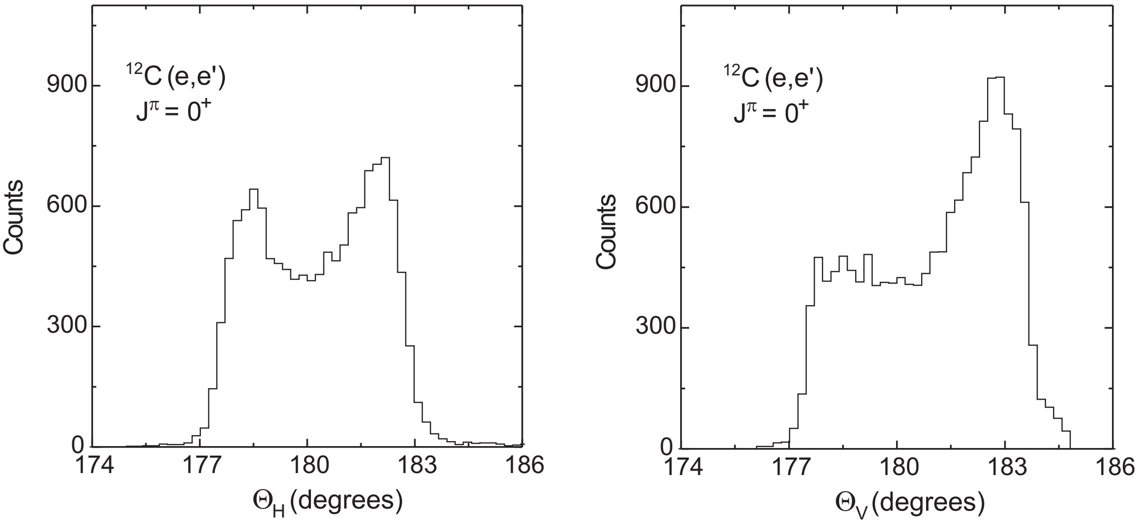

Fig. 11.4: Distribution of the reconstructed horizontal (left) and vertical (right) scattering angles with an excitation energy less than 100 keV for the ^{12}C elastic line in CD_2.

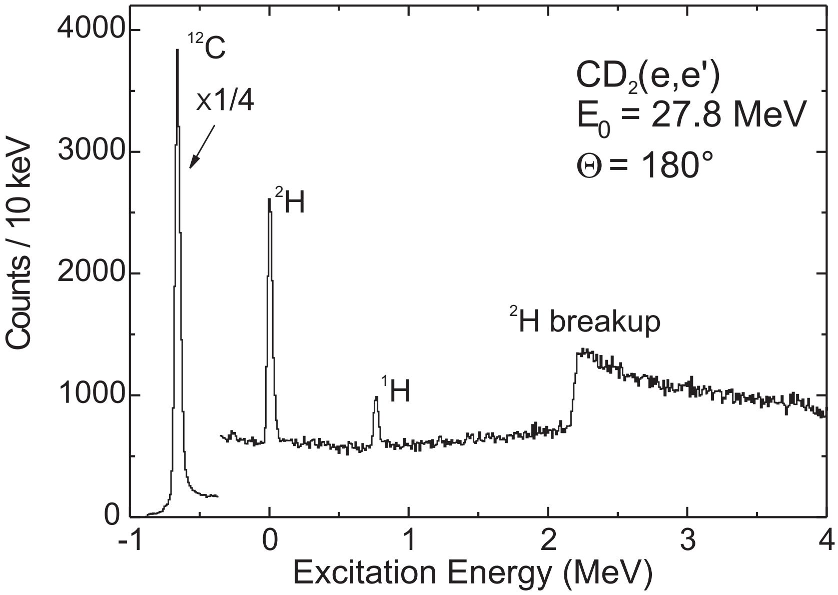

Fig. 11.5: Spectrum of the CD_2(e,e′) reaction at 180° and $E_0 = 27.8$ MeV. The spectrum is scaled by a factor of 1/4 for ^{12}C elastic line.

of the 'separating magnet' in the horizontal plane and due to a circular shape of the spectrometer aperture. A minor contribution might also arise if the beam passes not exactly perpendicular to the target and/or its position is not properly adjusted. The horizontal angle Θ_H is limited by the aperture of the QCLAM spectrometer and by the size of the detector system. Thus, acceptance depends on the momentum deviation $\Delta p/p_{cent}$. There are also electric transitions in the observed excitation energy region, whose cross section is very sensitive to the changes in the scattering angle. Thus, a software cut independent on the $\Delta p/p_{cent}$ was applied for Θ_H in order to obtain a constant solid-angle acceptance in the whole spectrum and a fixed effective scattering angle. The horizontal angle like the vertical angle was limited to the region 177° - 183° resulting in a solid angle acceptance of 9.47 msr. Figure 11.5 displays the CD_2 excitation energy spectrum including all cuts and corrections. Here, the ^{12}C elastic line, the deuteron and hydrogen elastic lines, and the breakup of the deuteron are observed.

11.2 Determination of the cross sections

Differential cross sections here calculated for the deuteron only. It can be determined absolutely by the following expression

$$\frac{d^2\sigma}{d\Omega dE_{\mathrm{x}}} = \frac{A}{TN_A}\,\frac{e}{Q_{eff}}\,\frac{N_{\Delta E_{\mathrm{x}},\Delta\Omega}}{\Delta E_{\mathrm{x}}\Delta\Omega} \qquad \left[\frac{\mu\mathrm{b}}{\mathrm{srMeV}}\right]. \tag{11.2}$$

Here

- N: number of events in the excitation energy bin ΔE_{x} and the solid angle acceptance $\Delta\Omega$
- A: target mass [g/mol]
- T: target thickness [mg/cm^2]
- N_A: Avogadro number [1/mol]
- e: electron charge [C]
- Q_{eff}: accumulated charge corrected for dead time [C]
- ΔE_{x}: energy bin [MeV]
- $\Delta\Omega$: solid angle acceptance [sr].

Under $\Theta = 180°$ elastic scattering is strongly suppressed for targets with ground state $\mathrm{J}^\pi = 0^+$. Since the effective scattering angle Θ_{eff} was about 177.5° in the experiment, the ^{12}C elastic line is still visible in the spectrum. It might thus be used for relative normalization of the deuteron inelastic scattering cross section. Since Θ_{eff} can, however, be determined only with the uncertainty of approximately 0.1° [123], this leads to a systematic error of more than 10% in the extracted elastic cross section (e.g. in ^{12}C). However, the deuteron ground state has $\mathrm{J}^\pi = 1^+$. This means that the elastic cross section is mainly of transverse character at $\Theta_{eff} = 177.5°$. Thus, a rather precise relative normalization of the inelastic cross section is possible by using the deuteron elastic line. The elastic cross section is usually determined [126] by two structure functions $A(q^2)$ and $B(q^2)$

$$\frac{d\sigma}{d\Omega} = \frac{d\sigma}{d\Omega}_{\mathrm{Mott}}\left[A(q^2) + B(q^2)\tan^2\left(\frac{\Theta}{2}\right)\right], \tag{11.3}$$

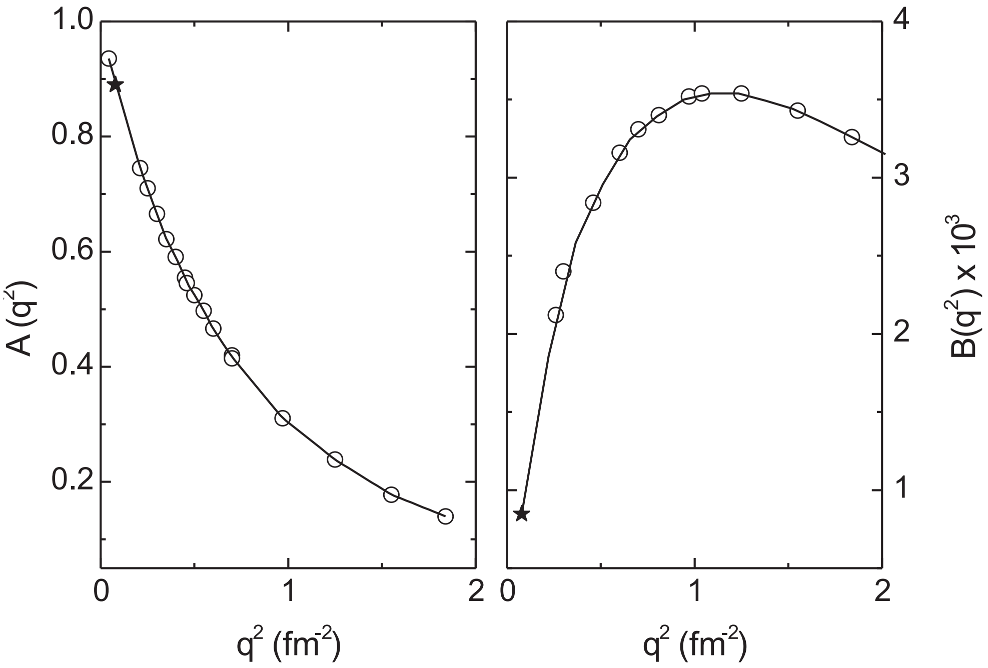

Fig. 11.6: Elastic deuteron structure functions $A(q^2)$ (left) and $B(q^2)$ (right) as functions of the momentum transfer. The solid lines show a fit to the experimental data (circles) taken from [127]. The stars represent the values extracted for the calculation of the cross section in the present experiment.

where $d\sigma/d\Omega_{\mathrm{Mott}}$ is the Mott cross section and Θ is the scattering angle. The structure functions A and B are well measured [127] for the momentum transfer $q^2 \; > 0.25 \; fm^{-2}$. The extrapolation of these data to the present case (q^2 = 0.078 fm^{-2}) is shown in Fig. 11.6. The difference between the absolutely calculated cross sections from Eq. (11.2) and that determined through the relative normalization from Eq. (11.3) is 6% only, well within the respective error bars.

Because of the small mass of the electron, a serious disadvantage of the electron scattering is the generated radiation. It results in a broadening of the lines and radiation tails which appear in any spectral peak. There is a big advantage of 180° scattering that generally the intensities of the tail backgrounds are comparable for elastic and inelastic peaks. The first of the radiative corrections, the Schwinger correction, accounts for the loss of the peak area due to those electrons degraded because of the emission of real soft photons as well as emission and absorption of virtual photons of any energy. Bremsstrahlung corrections take into account effects which cause an asymmetric distortion of the peak due to small angle scattering from electrons and nuclei other than the scattering nucleus. The third effect, Landau straggling, describes the broadening of the peak due to the losses of energy from atomic excitation and ionisation. Thus, the cross section should be multiplied by correction factors

$$\frac{d\sigma}{d\Omega} = \frac{d\sigma^{exp}}{d\Omega} \exp(\delta_S + \delta_B) \left(\frac{1}{1 - \delta_I} \right). \tag{11.4}$$

The value δ_S stands for the Schwinger correction, δ_B for bremsstrahlung and δ_I for ionisation corrections. A detailed description of these corrections can be found in [126, 128, 129]. At 180° the anomalous magnetic moment of the electron contributes to the radiative correction to scattering by a charge. This effect slightly increases the Schwinger correction. An explicit formula for the Schwinger correction to both charge and magnetic scattering was given by Borie [130] and used for the present calculation. The total correction factor is as large as 36%, where the largest contribution comes from the Schwinger correction.

The measured cross sections contain not only statistical but also the following systematic errors which contribute to the total uncertainty in the determination of the cross sections:

- Uncertainty in the determination of the accumulated charge in the Faraday cup (5%)
- Error in the dead-time correction (2%)
- Target inhomogenity (5%)
- Inaccuracy in the solid angle (7%).

The errors although being systematic once were treated as independent of each other and therefore can be added quadratically giving the total systematic error of approximately 10%.

11.3 Decomposition of the spectrum

A decomposition of the CD_2 spectrum into individual peaks and background (Fig. 11.7) has been performed using the program FIT [69]. The line shape of the elastic lines has been described by a special function, which takes into account the radiative tail as well as a Gaussian line shape due to the detector response [123].

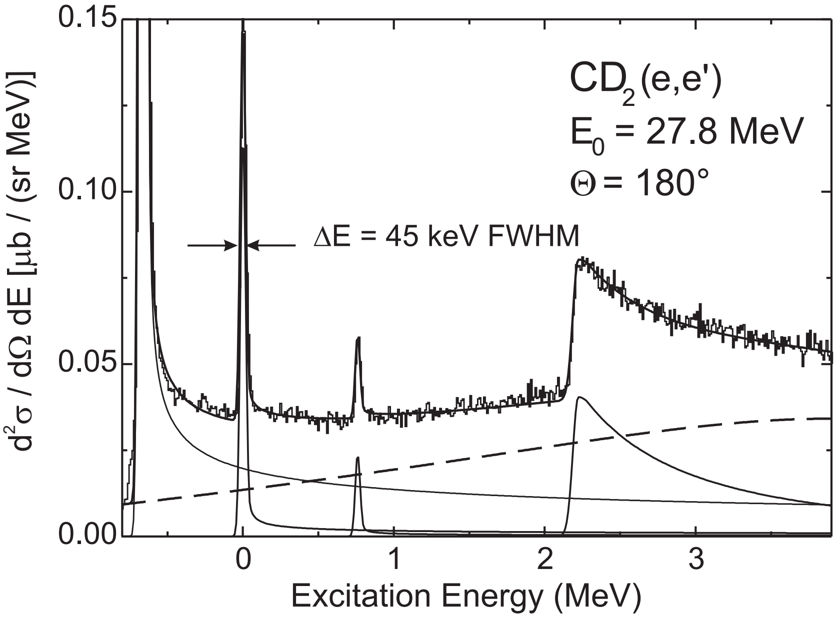

Fig. 11.7: Spectrum of the CD_2(e,e′) reaction at 180° and $E_0 = 27.8$ MeV. Solid lines: adjusted model functions for each individual peak and resulting fit. Dashed line: background function determined by the empty target frame measurements.

$$y = y_0 \cdot \begin{cases} \exp[-C(x-x_0)^2/\sigma_1^2] & x < x_0 \\ \exp[-C(x-x_0)^2/\sigma_2^2] & x_0 < x \leq x_0 + \eta\sigma_2 \\ A/(B+x-x_0)^\gamma & x > x_0 + \eta\sigma_2. \end{cases} \tag{11.5}$$

It consists of three smoothly connected parts: a Gaussian rising flank of width σ_1, a Gaussian dropping flank of width σ_2 and a hyperbolic function simulating the radiative tail. The symbol x_0 denotes the energy of the peak maximum, y_0 is the value at the peak maximum, η is the starting point of the radiative tail in units σ_2 and γ is the exponent of the hyperbolic function. The factors A, B and C result from the condition of the smoothly differentiable connection of the individual functions at the interconnection points x_0 and $\mathrm{x}_0 + \eta\sigma_2$. The same line shape, but with different parameters, has been applied to fit the breakup of the deuteron. The shape and the magnitude of the instrumental background was determined by the empty frame measurements during the experiment and approximated in the spectrum with a polynomial. All lines and the background have been fitted simultaneously.

11.4 Discussion

In the next step of the analysis the elastic radiative tails and the instrumental background have been subtracted from the inelastic spectrum. In spite of good energy resolution the spectrum of the deuteron breakup still should be deconvoluted in order to obtain the correct line shape. The instrumental response function has been expected to be a Gaussian function with a width of 45 keV (FWHM). The deconvolution procedure has been described in Chapter 6.1. Also in this case it was observed, that both, Fourier transform and Tikhonov's regularization methods furnish identical results. The spectrum before and after the deconvolution is shown in Fig. 11.8.

The cross sections were then multiplied by the radiative correction factor in each energy bin of the inelastic continuum and compared with theoretical calculations for the electrodisintegration of the deuteron based on a phenomenological nucleon-nucleon potential (Bonn-B) provided by Arenhövel [131, 132]. Meson exchange currents and isobar configurations are included in the calculations. An excellent agreement of the experimental magnetic dipole disintegration cross sections with theoretical predictions is observed, as can be seen in Fig. 11.9.

There are also effective field theory [134] calculations of d(e,e′p)n coincidence cross sections at 180°. The results described in [134] show a perfect agreement with the potential model calculations in the same kinematical regime. Thus, one can expect, that future calculations [133,135] of the inclusive d(e,e′) cross sections might also give good agreement with the present experimental data.

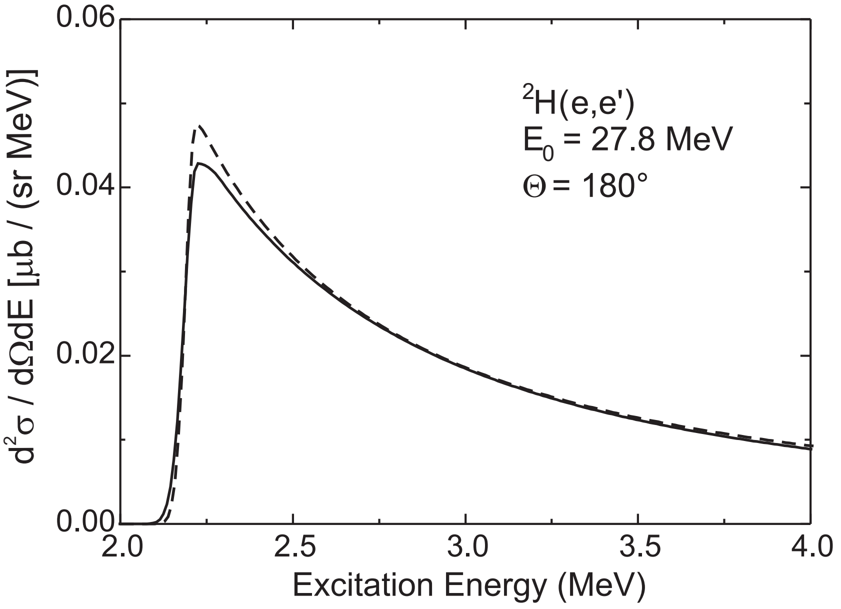

Fig. 11.8: Solid line: deuteron electrodisintegration spectrum at 180° for E_0 = 27.8 MeV with an energy resolution ΔE = 45 keV FWHM. Dashed line: deconvoluted spectrum.

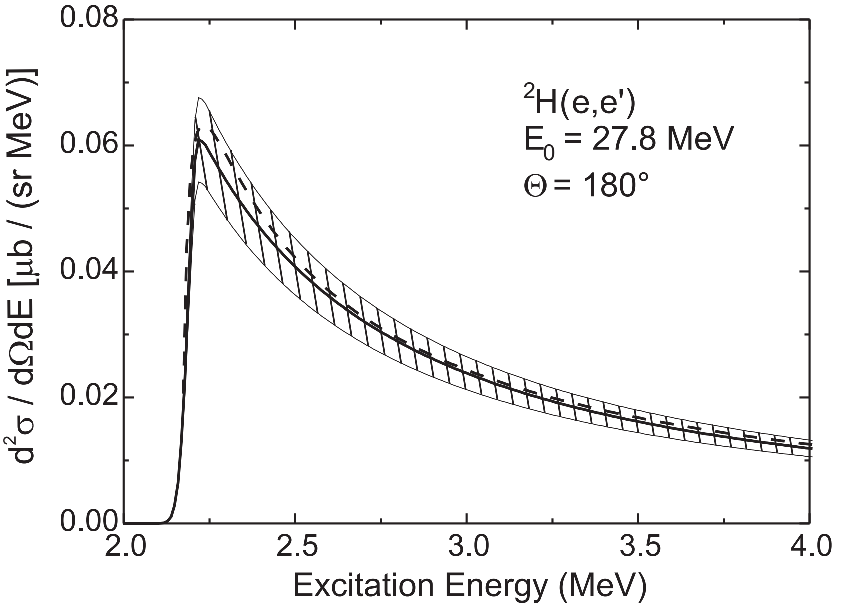

Fig. 11.9: Solid line: deconvoluted deuteron spectrum at 180° for $E_0 = 27.8$ MeV with experimental uncertainties (hatched area). Dashed line: theoretical calculations based on phenomenological nucleon-nucleon potential (Bonn-B) [131].

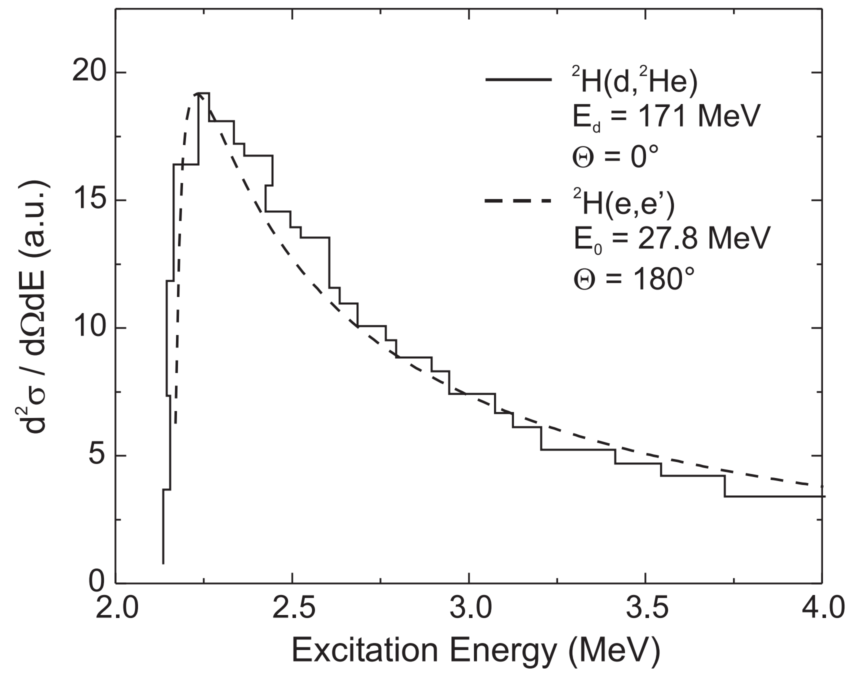

Fig. 11.10: Dashed line: deuteron electrodisintegration spectrum at 180° for E_0 = 27.8 MeV. Solid line: excitation energy spectrum of the ^{2}H(d,^{2}He) reaction at $\Theta = 0°$ (see Ref. [136] for further details).

The charge-exchange (d,^{2}He) reaction used in the first part of the present thesis to study the exotic ^{7}He nucleus has also been utilized [136] to investigate the ^{2}H system. Taken from that work the excitation energy spectrum of the ^{2}H(d,^{2}He)^{2}n reaction measured at zero-degree is shown in Fig. 11.10 (solid line) together with the 180° deuteron electrodisintegration spectrum from the present experiment (dashed line) normalized on the respective maxima of the cross sections. Excellent agreement between their shapes is observed. This is a quite remarkable finding since these two reactions are based on totally different types of interaction. It is known that the (d,^{2}He) reaction induces exclusively isovector spin-flip excitations. From the above mentioned agreement it becomes evident that also in the ^{2}H(e,e$'$) reaction at 180° at low-momentum transfer the M1 contribution dominates in the measured breakup cross section.

11.5 Extraction of the astrophysical $np \longrightarrow d\gamma$ cross section

Under the simplifying assumption that the deuteron electrodisintegration cross section measured at 180° is exclusively described by a magnetic dipole (M1) transition, one can extract the form factor

$$\frac{d\sigma(180^\circ)}{d\Omega} = \frac{e^2}{2E_1^2}\frac{E_3}{E_1}\frac{q^2}{M_d^2}[G_M(q^2)]^2, \tag{11.6}$$

where E_1 and E_3 are respectively the energies of the incident and scattered electron, G_M is the deuteron magnetic form factor, M_d denotes the deuteron mass, and q is the four momentum transfer. From the definition of magnetic cross section [137] for scattering at an angle Θ and for a momentum transfer q

$$\begin{aligned} \frac{d\sigma}{d\Omega}(\Theta, q) &= \frac{d\sigma}{d\Omega}_{\text{Mott}} V_{\text{T}} F_{\text{T}}^2(q) \qquad (11.7) \\ &= \frac{d\sigma}{d\Omega}_{\text{Mott}} \frac{q^2}{6M_d^2}[G_M(q^2)]^2 \left[1 + 2\left(1 + \frac{q^2}{4M_d^2}\right)\tan^2\left(\frac{\Theta}{2}\right)\right]. \end{aligned}$$

Here, $d\sigma/d\Omega_{\text{Mott}}$ is the Mott cross section and V_{T} is the transversal kinematic factor. From this expression one can extract the form factor

$$F_{\text{T}}^2(q) = \frac{q^2}{3M_d^2}[G_M(q^2)]^2. \tag{11.8}$$

In order to extrapolate the form factor obtained in the electron scattering to the photon point, one needs also the data measured at higher energy ($E_0 = 74$ MeV). Using the two data points from the present experiment together with data from the literature [127], an extrapolation procedure similar to that described in Section 11.2 can be invoked. The $B(M1)$ strength is calculated from the following equation

$$B(M1, q) = \frac{9}{2q^2}F_{\text{T}}^2(q). \tag{11.9}$$

Since the absorption cross sections are proportional to the radiative widths, one obtaines the widths from

$$\Gamma_\gamma(\uparrow) = 0.01157 E_\gamma^3 B(M1, \uparrow), \tag{11.10}$$

with

$$\Gamma_\gamma(\downarrow) = \frac{(2j_0+1)}{(2j_x+1)}\Gamma_\gamma(\uparrow). \tag{11.11}$$

For the deuteron case the spin of the ground state $j_0 = 1$, and the spin of the investigated excited state at $E_x = 2.2$ MeV is assumed to be $j_x = 0$. Thus, one can write

$$\Gamma_\gamma(\downarrow) = 3\Gamma_\gamma(\uparrow). \tag{11.12}$$

For the radiative capture of neutrons the absorption cross section is written as

$$\sigma = \pi \lambda\!\!\!^{-} \frac{(2j_R+1)}{(2j_a+1)(2j_b+1)} \frac{1}{(E-E_R)^2 + \frac{1}{4}\Gamma^2} \Gamma_n \Gamma_\gamma, \tag{11.13}$$

where $j_a = j_b = 1/2$ are the spins of the nucleons and $j_R = 0$ is the spin of the resonance, and $\lambda\!\!\!^{-}$ is defined as

$$\lambda\!\!\!^{-} = \frac{M_a + M_b}{M_b} \frac{\hbar}{\sqrt{2M_a E_L}}. \tag{11.14}$$

In the present case the values M_a, M_b are the nucleon masses and the E_L is the kinetic energy in the laboratory frame. At the continuum in the excitation energy spectrum one can set $E = E_R$ and Γ is equal to the bin width. One can also set $\Gamma = \Gamma_n$, because the predominant decay mode is the elastic channel. The cross section then looks like

$$\sigma = \pi \lambda\!\!\!^{-2} \frac{4 \cdot (2j_R+1)}{(2j_a+1)(2j_b+1)} \frac{\Gamma_\gamma(\downarrow)}{\Gamma}. \tag{11.15}$$

During the period of interest (see Section 9) the nucleons are nonrelativistic. Assuming that both proton and neutron are distributed according to the Maxwell-Boltzmann distribution for temperature T, the $np \to d\gamma$ reaction rate is expressed in terms of the cross section by

$$\langle \sigma v \rangle = \left(\frac{8}{\pi\mu}\right)^{1/2} \int \sigma(E) \exp(-E/kT) dE, \tag{11.16}$$

where μ is the reduced mass.

12 Summary and outlook

Electron scattering at 180° provides numerous advantages for the study of nuclear structure, in particular magnetic excitations in nuclei. The M1 cross section of the deuteron breakup has been precisely measured close to threshold with good energy resolution of $\Delta E = 45$ keV (FWHM) using the d(e,e$'$) reaction at 180° for $E_0 = 27.8$ MeV. Data were also taken at higher electron energy $E_0 = 74$ MeV and will be analyzed in the near future. From this electrodisintegration cross section one can infer in a further analysis the astrophysically relevant cross section for $np \longrightarrow d\gamma$ process which in turn provides information about abundances of light elements in Big-Bang nucleosynthesis. Data are in excellent agreement with theoretical calculations based on a phenomenological nucleon-nucleon potential (Bonn-B), and inclusion of meson-exchange currents and isobar configurations. It would be also of interest to compare the data with effective field theory calculations which are now in progress.

The d(e,e$'$) data obtained close to the threshold can make an important contribution to the Gerasimov-Drell-Hearn (GDH) sum rule. GDH connects an energy weighted integral of spin-polarized photoabsorption cross section with the anomalous magnetic moment of the target [138]. Since the magnetic moment of the deuteron is very small, the absolute value of the integral is also small. At higher energies it can be estimated by the incoherent sum of quasifree production from the individual nucleons in the deuteron that means that this contribution is large and positive. This can be cancelled by large negative contribution at lower energies dominated by the breakup peak. It is expected that the GDH sum rule is dominated by the M1 component of the cross section near the breakup threshold. This means that the measured cross sections can be directly related to the sum rule [139].

A Double-differential cross sections for the ^{7}Li(d,^{2}He) reaction

The double-differential cross sections for the ^{7}Li(d,^{2}He) reaction for various scattering angles have been calculated in Section 4.4 and are listed in the following table. The values are given in [μb / (sr MeV)]. The errors are statistical only.

Tab. A.1: Double-differential cross sections for the ^{7}Li(d,^{2}He)^{7}He reaction for various scattering angles.

E$_x$, MeV	0.0°–1.0°	1.0°–2.0°	2.0°–3.0°	3.7°–4.7°	4.7°–5.7°	5.9°–6.9°	6.9°–7.9°	9.3°–10.3°	10.3°–11.3°
-0.60	-2.16 $^{\pm0.33}$	0.38 $^{\pm0.27}$	0.46 $^{\pm0.33}$	0.80 $^{\pm0.67}$	0.41 $^{\pm0.47}$	3.07 $^{\pm0.53}$	1.57 $^{\pm0.33}$	0.11 $^{\pm0.07}$	1.20 $^{\pm0.07}$
-0.5	0.4 $^{\pm0.7}$	3.5 $^{\pm0.7}$	4.1 $^{\pm0.7}$	3.4 $^{\pm1.3}$	2.6 $^{\pm1.3}$	1.7 $^{\pm0.7}$	-2.4 $^{\pm0.7}$	-0.1 $^{\pm0.0}$	3.1 $^{\pm0.7}$
-0.3	12.6 $^{\pm2.0}$	6.0 $^{\pm0.7}$	4.8 $^{\pm0.7}$	4.2 $^{\pm1.3}$	8.9 $^{\pm2.0}$	6.3 $^{\pm0.7}$	8.9 $^{\pm0.7}$	4.8 $^{\pm0.7}$	7.4 $^{\pm0.7}$
-0.2	56.6 $^{\pm4.0}$	48.7 $^{\pm2.7}$	34.2 $^{\pm2.7}$	60.3 $^{\pm6.0}$	19.4 $^{\pm3.3}$	33.3 $^{\pm2.0}$	31.6 $^{\pm1.3}$	41.2 $^{\pm2.0}$	46.5 $^{\pm2.0}$
0.0	92.8 $^{\pm5.3}$	76.4 $^{\pm3.3}$	75.7 $^{\pm4.0}$	94.2 $^{\pm7.3}$	94.2 $^{\pm7.3}$	81.9 $^{\pm2.7}$	82.6 $^{\pm2.7}$	72.6 $^{\pm2.7}$	69.4 $^{\pm2.0}$
0.2	25.9 $^{\pm2.7}$	25.2 $^{\pm2.0}$	28.4 $^{\pm2.0}$	39.8 $^{\pm4.7}$	45.6 $^{\pm4.7}$	35.3 $^{\pm2.0}$	45.2 $^{\pm2.0}$	25.7 $^{\pm1.3}$	25.9 $^{\pm1.3}$
0.3	26.7 $^{\pm3.3}$	17.3 $^{\pm1.3}$	22.6 $^{\pm2.0}$	24.3 $^{\pm4.0}$	23.6 $^{\pm3.3}$	22.9 $^{\pm1.3}$	21.0 $^{\pm1.3}$	12.9 $^{\pm1.3}$	13.5 $^{\pm0.7}$
0.5	17.6 $^{\pm2.7}$	17.5 $^{\pm1.3}$	13.1 $^{\pm1.3}$	28.4 $^{\pm4.0}$	24.7 $^{\pm3.3}$	18.7 $^{\pm1.3}$	14.7 $^{\pm1.3}$	9.9 $^{\pm0.7}$	12.5 $^{\pm0.7}$
0.6	16.4 $^{\pm2.7}$	18.2 $^{\pm2.0}$	21.3 $^{\pm2.0}$	10.5 $^{\pm2.7}$	17.7 $^{\pm3.3}$	17.9 $^{\pm1.3}$	13.6 $^{\pm1.3}$	10.4 $^{\pm0.7}$	7.9 $^{\pm0.7}$
0.8	16.5 $^{\pm2.7}$	17.3 $^{\pm1.3}$	19.7 $^{\pm2.0}$	26.2 $^{\pm4.0}$	21.5 $^{\pm3.3}$	13.3 $^{\pm1.3}$	15.5 $^{\pm1.3}$	9.7 $^{\pm0.7}$	8.1 $^{\pm0.7}$
0.9	24.5 $^{\pm2.7}$	22.4 $^{\pm2.0}$	18.5 $^{\pm2.0}$	21.3 $^{\pm3.3}$	17.6 $^{\pm3.3}$	18.9 $^{\pm1.3}$	17.6 $^{\pm1.3}$	10.5 $^{\pm0.7}$	11.2 $^{\pm0.7}$
1.1	20.5 $^{\pm2.7}$	22.3 $^{\pm2.0}$	20.7 $^{\pm2.0}$	24.5 $^{\pm4.0}$	24.8 $^{\pm3.3}$	17.5 $^{\pm1.3}$	18.5 $^{\pm1.3}$	9.9 $^{\pm0.7}$	11.4 $^{\pm0.7}$
1.2	23.3 $^{\pm2.7}$	26.2 $^{\pm2.0}$	23.0 $^{\pm2.0}$	19.7 $^{\pm3.3}$	17.5 $^{\pm2.7}$	22.7 $^{\pm1.3}$	19.2 $^{\pm1.3}$	12.2 $^{\pm0.7}$	12.5 $^{\pm0.7}$
1.4	31.0 $^{\pm3.3}$	27.3 $^{\pm2.0}$	29.2 $^{\pm2.0}$	25.7 $^{\pm4.0}$	25.0 $^{\pm3.3}$	23.9 $^{\pm1.3}$	20.0 $^{\pm1.3}$	10.8 $^{\pm0.7}$	9.7 $^{\pm0.7}$

Tab. A.1: Double-differential cross sections for the ^{7}Li(d,^{2}He)^{7}He reaction for various scattering angles.

E_x, MeV	0.0°–1.0°	1.0°–2.0°	2.0°–3.0°	3.7°–4.7°	4.7°–5.7°	5.9°–6.9°	6.9°–7.9°	9.3°–10.3°	10.3°–11.3°
1.5	$38.1^{\pm 3.3}$	$27.2^{\pm 2.0}$	$28.9^{\pm 2.0}$	$33.8^{\pm 4.0}$	$25.2^{\pm 3.3}$	$24.1^{\pm 1.3}$	$20.8^{\pm 1.3}$	$13.1^{\pm 1.3}$	$14.9^{\pm 0.7}$
1.7	$30.5^{\pm 3.3}$	$37.3^{\pm 2.0}$	$34.7^{\pm 2.7}$	$33.8^{\pm 4.0}$	$36.3^{\pm 4.0}$	$28.3^{\pm 1.3}$	$28.5^{\pm 1.3}$	$11.7^{\pm 1.3}$	$15.8^{\pm 0.7}$
1.8	$42.7^{\pm 3.3}$	$38.4^{\pm 2.7}$	$32.9^{\pm 2.7}$	$34.0^{\pm 4.0}$	$40.0^{\pm 4.7}$	$33.7^{\pm 2.0}$	$29.1^{\pm 1.3}$	$21.9^{\pm 1.3}$	$16.0^{\pm 0.7}$
2.0	$33.1^{\pm 3.3}$	$31.6^{\pm 2.7}$	$39.9^{\pm 2.7}$	$48.6^{\pm 5.3}$	$47.4^{\pm 4.7}$	$42.8^{\pm 2.0}$	$37.7^{\pm 2.0}$	$21.9^{\pm 1.3}$	$16.8^{\pm 0.7}$
2.1	$47.8^{\pm 5.3}$	$37.5^{\pm 4.0}$	$15.9^{\pm 3.3}$	$43.7^{\pm 6.0}$	$35.0^{\pm 5.3}$	$24.5^{\pm 2.0}$	$25.3^{\pm 2.0}$	$21.8^{\pm 1.3}$	$17.9^{\pm 0.7}$
2.3	$43.4^{\pm 4.0}$	$47.7^{\pm 2.7}$	$52.3^{\pm 3.3}$	$48.3^{\pm 5.3}$	$42.5^{\pm 4.7}$	$33.3^{\pm 2.0}$	$31.7^{\pm 1.3}$	$23.6^{\pm 1.3}$	$16.4^{\pm 0.7}$
2.4	$45.3^{\pm 4.0}$	$58.3^{\pm 2.7}$	$54.9^{\pm 3.3}$	$60.5^{\pm 5.3}$	$46.2^{\pm 4.7}$	$40.8^{\pm 2.0}$	$35.2^{\pm 1.3}$	$23.2^{\pm 1.3}$	$18.8^{\pm 0.7}$
2.6	$61.7^{\pm 4.0}$	$51.9^{\pm 2.7}$	$50.4^{\pm 2.7}$	$65.1^{\pm 6.0}$	$55.9^{\pm 5.3}$	$42.7^{\pm 2.0}$	$40.0^{\pm 2.0}$	$24.5^{\pm 1.3}$	$22.2^{\pm 1.3}$
2.7	$55.3^{\pm 4.0}$	$61.1^{\pm 2.7}$	$59.1^{\pm 3.3}$	$57.7^{\pm 5.3}$	$49.9^{\pm 4.7}$	$44.9^{\pm 2.0}$	$39.8^{\pm 2.0}$	$27.4^{\pm 1.3}$	$22.9^{\pm 1.3}$
2.9	$65.8^{\pm 4.7}$	$64.4^{\pm 2.7}$	$60.5^{\pm 3.3}$	$53.9^{\pm 5.3}$	$55.6^{\pm 5.3}$	$47.9^{\pm 2.0}$	$44.6^{\pm 2.0}$	$28.8^{\pm 1.3}$	$23.7^{\pm 1.3}$
3.0	$58.2^{\pm 4.0}$	$61.8^{\pm 2.7}$	$61.8^{\pm 3.3}$	$69.8^{\pm 6.0}$	$58.3^{\pm 5.3}$	$51.6^{\pm 2.0}$	$44.0^{\pm 2.0}$	$30.1^{\pm 1.3}$	$25.8^{\pm 1.3}$
3.2	$61.9^{\pm 4.0}$	$63.1^{\pm 2.7}$	$59.0^{\pm 3.3}$	$60.7^{\pm 5.3}$	$59.5^{\pm 5.3}$	$49.6^{\pm 2.0}$	$49.4^{\pm 2.0}$	$28.0^{\pm 1.3}$	$24.7^{\pm 1.3}$
3.3	$72.2^{\pm 4.7}$	$62.5^{\pm 2.7}$	$66.4^{\pm 3.3}$	$76.6^{\pm 6.0}$	$52.0^{\pm 4.7}$	$56.9^{\pm 2.0}$	$47.5^{\pm 2.0}$	$30.3^{\pm 1.3}$	$25.7^{\pm 1.3}$
3.5	$69.6^{\pm 4.7}$	$66.1^{\pm 3.3}$	$63.3^{\pm 3.3}$	$66.9^{\pm 6.0}$	$63.3^{\pm 5.3}$	$57.7^{\pm 2.0}$	$46.0^{\pm 2.0}$	$31.6^{\pm 1.3}$	$26.5^{\pm 1.3}$

Tab. A.1: Double-differential cross sections for the ^{7}Li(d,^{2}He)^{7}He reaction for various scattering angles.

E$_x$, MeV	0.0°–1.0°	1.0°–2.0°	2.0°–3.0°	3.7°–4.7°	4.7°–5.7°	5.9°–6.9°	6.9°–7.9°	9.3°–10.3°	10.3°–11.3°
3.6	$74.9^{\pm4.7}$	$73.6^{\pm3.3}$	$70.3^{\pm3.3}$	$62.0^{\pm5.3}$	$68.4^{\pm5.3}$	$53.5^{\pm2.0}$	$47.1^{\pm2.0}$	$30.2^{\pm1.3}$	$26.9^{\pm1.3}$
3.8	$71.3^{\pm4.7}$	$68.9^{\pm3.3}$	$67.5^{\pm3.3}$	$73.2^{\pm6.0}$	$55.0^{\pm5.3}$	$58.4^{\pm2.0}$	$48.8^{\pm2.0}$	$31.6^{\pm1.3}$	$26.3^{\pm1.3}$
3.9	$74.3^{\pm4.7}$	$73.9^{\pm3.3}$	$70.6^{\pm3.3}$	$66.4^{\pm6.0}$	$65.0^{\pm5.3}$	$53.2^{\pm2.0}$	$53.2^{\pm2.0}$	$35.3^{\pm1.3}$	$29.2^{\pm1.3}$
4.1	$68.3^{\pm4.7}$	$69.0^{\pm3.3}$	$67.2^{\pm3.3}$	$76.8^{\pm6.0}$	$80.6^{\pm6.0}$	$59.0^{\pm2.0}$	$52.7^{\pm2.0}$	$32.7^{\pm1.3}$	$29.3^{\pm1.3}$
4.2	$80.7^{\pm4.7}$	$69.9^{\pm3.3}$	$66.2^{\pm3.3}$	$75.8^{\pm6.0}$	$70.7^{\pm6.0}$	$62.3^{\pm2.0}$	$56.7^{\pm2.0}$	$33.4^{\pm1.3}$	$28.0^{\pm1.3}$
4.4	$79.6^{\pm4.7}$	$69.8^{\pm3.3}$	$74.4^{\pm3.3}$	$78.1^{\pm6.0}$	$64.9^{\pm5.3}$	$63.4^{\pm2.0}$	$53.0^{\pm2.0}$	$34.1^{\pm1.3}$	$27.6^{\pm1.3}$
4.5	$74.1^{\pm4.7}$	$74.8^{\pm3.3}$	$74.6^{\pm3.3}$	$84.4^{\pm6.7}$	$74.1^{\pm6.0}$	$58.8^{\pm2.0}$	$50.7^{\pm2.0}$	$35.4^{\pm1.3}$	$27.7^{\pm1.3}$
4.7	$72.1^{\pm4.7}$	$79.7^{\pm3.3}$	$73.3^{\pm3.3}$	$91.2^{\pm6.7}$	$61.7^{\pm5.3}$	$61.8^{\pm2.0}$	$59.8^{\pm2.0}$	$37.1^{\pm1.3}$	$28.7^{\pm1.3}$
4.8	$78.2^{\pm4.7}$	$72.2^{\pm3.3}$	$75.2^{\pm3.3}$	$83.8^{\pm6.7}$	$63.1^{\pm5.3}$	$62.1^{\pm2.0}$	$53.4^{\pm2.0}$	$36.9^{\pm1.3}$	$32.6^{\pm1.3}$
5.0	$72.2^{\pm4.7}$	$80.7^{\pm3.3}$	$69.0^{\pm3.3}$	$79.5^{\pm6.0}$	$79.5^{\pm6.0}$	$59.5^{\pm2.0}$	$54.7^{\pm2.0}$	$39.5^{\pm1.3}$	$32.0^{\pm1.3}$
5.1	$82.9^{\pm4.7}$	$77.9^{\pm3.3}$	$79.9^{\pm3.3}$	$86.4^{\pm6.7}$	$68.3^{\pm5.3}$	$61.3^{\pm2.0}$	$57.6^{\pm2.0}$	$38.6^{\pm1.3}$	$31.1^{\pm1.3}$
5.3	$75.0^{\pm4.7}$	$74.6^{\pm3.3}$	$69.7^{\pm3.3}$	$76.7^{\pm6.0}$	$65.2^{\pm5.3}$	$62.6^{\pm2.0}$	$54.3^{\pm2.0}$	$38.6^{\pm1.3}$	$31.1^{\pm1.3}$
5.4	$73.5^{\pm4.7}$	$83.7^{\pm3.3}$	$78.9^{\pm3.3}$	$75.9^{\pm6.0}$	$67.6^{\pm5.3}$	$61.4^{\pm2.0}$	$58.0^{\pm2.0}$	$38.6^{\pm1.3}$	$33.7^{\pm1.3}$
5.6	$87.0^{\pm4.7}$	$80.1^{\pm3.3}$	$79.0^{\pm3.3}$	$87.5^{\pm6.7}$	$61.9^{\pm5.3}$	$60.0^{\pm2.0}$	$58.2^{\pm2.0}$	$39.2^{\pm1.3}$	$34.2^{\pm1.3}$

Tab. A.1: Double-differential cross sections for the ^{7}Li(d,^{2}He)^{7}He reaction for various scattering angles.

E_x, MeV	0.0°–1.0°	1.0°–2.0°	2.0°–3.0°	3.7°–4.7°	4.7°–5.7°	5.9°–6.9°	6.9°–7.9°	9.3°–10.3°	10.3°–11.3°
5.7	$79.0^{\pm 4.7}$	$74.2^{\pm 3.3}$	$74.3^{\pm 3.3}$	$80.0^{\pm 6.0}$	$70.5^{\pm 5.3}$	$63.2^{\pm 2.0}$	$55.2^{\pm 2.0}$	$40.4^{\pm 1.3}$	$33.3^{\pm 1.3}$
5.9	$80.3^{\pm 4.7}$	$77.9^{\pm 3.3}$	$75.0^{\pm 3.3}$	$77.3^{\pm 6.0}$	$77.2^{\pm 6.0}$	$64.6^{\pm 2.0}$	$57.6^{\pm 2.0}$	$36.4^{\pm 1.3}$	$34.2^{\pm 1.3}$
6.0	$70.8^{\pm 4.7}$	$71.9^{\pm 3.3}$	$76.5^{\pm 3.3}$	$81.8^{\pm 6.0}$	$64.5^{\pm 5.3}$	$69.1^{\pm 2.0}$	$61.1^{\pm 2.0}$	$40.3^{\pm 1.3}$	$34.4^{\pm 1.3}$
6.2	$82.3^{\pm 4.7}$	$72.9^{\pm 3.3}$	$76.1^{\pm 3.3}$	$75.3^{\pm 6.0}$	$62.3^{\pm 5.3}$	$64.9^{\pm 2.0}$	$61.8^{\pm 2.0}$	$41.8^{\pm 1.3}$	$36.9^{\pm 1.3}$
6.3	$82.3^{\pm 4.7}$	$78.2^{\pm 3.3}$	$74.2^{\pm 3.3}$	$80.0^{\pm 6.0}$	$76.1^{\pm 6.0}$	$67.6^{\pm 2.7}$	$54.4^{\pm 2.0}$	$44.5^{\pm 2.0}$	$40.9^{\pm 1.3}$
6.5	$84.7^{\pm 4.7}$	$78.0^{\pm 3.3}$	$75.4^{\pm 3.3}$	$81.6^{\pm 6.7}$	$78.2^{\pm 6.0}$	$65.5^{\pm 2.7}$	$62.3^{\pm 2.0}$	$43.1^{\pm 1.3}$	$36.8^{\pm 1.3}$
6.6	$75.7^{\pm 4.7}$	$82.5^{\pm 3.3}$	$77.6^{\pm 4.0}$	$87.0^{\pm 6.7}$	$64.0^{\pm 5.3}$	$67.6^{\pm 2.7}$	$61.8^{\pm 2.0}$	$44.7^{\pm 1.3}$	$35.4^{\pm 1.3}$
6.8	$78.4^{\pm 4.7}$	$80.0^{\pm 3.3}$	$71.3^{\pm 3.3}$	$74.8^{\pm 6.0}$	$72.9^{\pm 6.0}$	$70.7^{\pm 2.7}$	$62.7^{\pm 2.0}$	$44.1^{\pm 1.3}$	$37.9^{\pm 1.3}$
6.9	$86.2^{\pm 4.7}$	$79.6^{\pm 3.3}$	$80.6^{\pm 4.0}$	$82.1^{\pm 6.7}$	$76.7^{\pm 6.0}$	$64.7^{\pm 2.0}$	$61.3^{\pm 2.0}$	$45.3^{\pm 1.3}$	$38.4^{\pm 1.3}$
7.1	$79.3^{\pm 4.7}$	$82.1^{\pm 3.3}$	$67.9^{\pm 3.3}$	$102.0^{\pm 7.3}$	$69.3^{\pm 5.3}$	$67.2^{\pm 2.0}$	$61.6^{\pm 2.0}$	$41.6^{\pm 1.3}$	$39.4^{\pm 1.3}$
7.2	$79.2^{\pm 4.7}$	$85.6^{\pm 3.3}$	$79.4^{\pm 4.0}$	$75.0^{\pm 6.0}$	$67.4^{\pm 5.3}$	$66.8^{\pm 2.0}$	$61.0^{\pm 2.0}$	$47.4^{\pm 2.0}$	$36.0^{\pm 1.3}$
7.4	$79.1^{\pm 4.7}$	$77.6^{\pm 3.3}$	$87.1^{\pm 4.0}$	$82.4^{\pm 6.7}$	$82.2^{\pm 6.0}$	$67.9^{\pm 2.0}$	$62.8^{\pm 2.0}$	$46.5^{\pm 2.0}$	$37.8^{\pm 1.3}$
7.5	$71.7^{\pm 4.7}$	$85.2^{\pm 3.3}$	$71.6^{\pm 3.3}$	$82.7^{\pm 6.7}$	$82.2^{\pm 6.0}$	$65.7^{\pm 2.0}$	$60.2^{\pm 2.0}$	$44.2^{\pm 1.3}$	$39.7^{\pm 1.3}$
7.7	$72.0^{\pm 4.7}$	$75.3^{\pm 3.3}$	$82.9^{\pm 4.0}$	$78.9^{\pm 6.0}$	$76.9^{\pm 6.0}$	$69.2^{\pm 2.7}$	$62.9^{\pm 2.0}$	$45.8^{\pm 2.0}$	$38.9^{\pm 1.3}$

Tab. A.1: Double-differential cross sections for the ^{7}Li(d,^{2}He)^{7}He reaction for various scattering angles.

E$_x$, MeV	0.0°–1.0°	1.0°–2.0°	2.0°–3.0°	3.7°–4.7°	4.7°–5.7°	5.9°–6.9°	6.9°–7.9°	9.3°–10.3°	10.3°–11.3°
7.8	76.6 $^{\pm 4.7}$	80.3 $^{\pm 3.3}$	69.8 $^{\pm 3.3}$	91.7 $^{\pm 6.7}$	62.2 $^{\pm 5.3}$	68.7 $^{\pm 2.7}$	60.1 $^{\pm 2.0}$	46.9 $^{\pm 2.0}$	41.7 $^{\pm 1.3}$
8.0	77.2 $^{\pm 4.7}$	80.3 $^{\pm 3.3}$	75.5 $^{\pm 3.3}$	85.3 $^{\pm 6.7}$	73.3 $^{\pm 6.0}$	66.3 $^{\pm 2.0}$	60.1 $^{\pm 2.0}$	45.9 $^{\pm 2.0}$	43.1 $^{\pm 1.3}$
8.1	77.8 $^{\pm 4.7}$	79.6 $^{\pm 3.3}$	87.4 $^{\pm 4.0}$	69.1 $^{\pm 6.0}$	67.1 $^{\pm 5.3}$	67.3 $^{\pm 2.0}$	61.7 $^{\pm 2.0}$	48.7 $^{\pm 2.0}$	40.0 $^{\pm 1.3}$
8.3	77.6 $^{\pm 4.7}$	75.3 $^{\pm 3.3}$	72.8 $^{\pm 3.3}$	75.2 $^{\pm 6.0}$	73.6 $^{\pm 6.0}$	66.7 $^{\pm 2.0}$	59.0 $^{\pm 2.0}$	47.8 $^{\pm 2.0}$	40.4 $^{\pm 1.3}$
8.4	86.3 $^{\pm 5.3}$	80.6 $^{\pm 3.3}$	78.9 $^{\pm 4.0}$	69.9 $^{\pm 6.0}$	74.2 $^{\pm 6.0}$	68.2 $^{\pm 2.7}$	63.9 $^{\pm 2.0}$	43.8 $^{\pm 1.3}$	41.8 $^{\pm 1.3}$
8.6	80.0 $^{\pm 4.7}$	73.6 $^{\pm 3.3}$	73.1 $^{\pm 3.3}$	76.9 $^{\pm 6.0}$	77.2 $^{\pm 6.0}$	71.4 $^{\pm 2.7}$	61.1 $^{\pm 2.0}$	44.3 $^{\pm 1.3}$	40.7 $^{\pm 1.3}$
8.7	78.7 $^{\pm 4.7}$	81.4 $^{\pm 3.3}$	74.9 $^{\pm 4.0}$	84.9 $^{\pm 6.7}$	75.5 $^{\pm 6.0}$	62.8 $^{\pm 2.0}$	60.5 $^{\pm 2.0}$	44.0 $^{\pm 1.3}$	40.9 $^{\pm 1.3}$
8.9	78.5 $^{\pm 4.7}$	75.0 $^{\pm 3.3}$	70.3 $^{\pm 3.3}$	74.4 $^{\pm 6.0}$	76.4 $^{\pm 6.0}$	63.8 $^{\pm 2.0}$	60.5 $^{\pm 2.0}$	42.3 $^{\pm 1.3}$	41.0 $^{\pm 1.3}$
9.0	80.2 $^{\pm 4.7}$	81.5 $^{\pm 3.3}$	72.4 $^{\pm 3.3}$	85.5 $^{\pm 6.7}$	81.3 $^{\pm 6.0}$	66.5 $^{\pm 2.7}$	60.6 $^{\pm 2.0}$	42.1 $^{\pm 1.3}$	38.0 $^{\pm 1.3}$
9.2	78.8 $^{\pm 4.7}$	79.1 $^{\pm 3.3}$	68.7 $^{\pm 3.3}$	69.5 $^{\pm 6.0}$	78.4 $^{\pm 6.0}$	66.5 $^{\pm 2.7}$	57.5 $^{\pm 2.0}$	43.0 $^{\pm 1.3}$	41.4 $^{\pm 1.3}$
9.3	71.9 $^{\pm 4.7}$	79.0 $^{\pm 3.3}$	68.7 $^{\pm 3.3}$	62.3 $^{\pm 6.0}$	78.3 $^{\pm 6.0}$	64.8 $^{\pm 2.7}$	60.6 $^{\pm 2.0}$	41.8 $^{\pm 1.3}$	41.5 $^{\pm 1.3}$
9.5	70.3 $^{\pm 4.7}$	77.1 $^{\pm 3.3}$	77.1 $^{\pm 4.0}$	76.0 $^{\pm 6.7}$	67.8 $^{\pm 6.0}$	63.9 $^{\pm 2.7}$	59.0 $^{\pm 2.0}$	43.3 $^{\pm 2.0}$	40.4 $^{\pm 1.3}$
9.6	77.2 $^{\pm 4.7}$	77.5 $^{\pm 3.3}$	70.5 $^{\pm 4.0}$	78.9 $^{\pm 6.7}$	82.8 $^{\pm 6.7}$	63.2 $^{\pm 2.7}$	60.6 $^{\pm 2.0}$	44.7 $^{\pm 2.0}$	42.4 $^{\pm 1.3}$
9.8	78.3 $^{\pm 4.7}$	74.2 $^{\pm 3.3}$	68.9 $^{\pm 4.0}$	77.7 $^{\pm 6.7}$	74.3 $^{\pm 6.0}$	63.4 $^{\pm 2.7}$	57.9 $^{\pm 2.0}$	43.7 $^{\pm 2.0}$	39.0 $^{\pm 1.3}$

Tab. A.1: Double-differential cross sections for the ^{7}Li(d,^{2}He)^{7}He reaction for various scattering angles.

E_x, MeV	0.0°–1.0°	1.0°–2.0°	2.0°–3.0°	3.7°–4.7°	4.7°–5.7°	5.9°–6.9°	6.9°–7.9°	9.3°–10.3°	10.3°–11.3°
9.9	$70.0^{\pm 4.7}$	$75.6^{\pm 3.3}$	$68.0^{\pm 4.0}$	$85.6^{\pm 6.7}$	$74.4^{\pm 6.0}$	$62.2^{\pm 2.7}$	$56.9^{\pm 2.0}$	$47.5^{\pm 2.0}$	$39.4^{\pm 1.3}$
10.1	$80.7^{\pm 5.3}$	$72.6^{\pm 3.3}$	$67.6^{\pm 4.0}$	$69.7^{\pm 6.0}$	$65.0^{\pm 6.0}$	$62.9^{\pm 2.7}$	$60.1^{\pm 2.0}$	$45.6^{\pm 2.0}$	$42.2^{\pm 1.3}$
10.2	$84.0^{\pm 5.3}$	$78.5^{\pm 3.3}$	$66.5^{\pm 4.0}$	$67.4^{\pm 6.0}$	$87.2^{\pm 6.7}$	$64.1^{\pm 2.7}$	$62.6^{\pm 2.0}$	$45.7^{\pm 2.0}$	$36.0^{\pm 1.3}$
10.4	$77.2^{\pm 5.3}$	$76.8^{\pm 3.3}$	$71.7^{\pm 4.0}$	$72.1^{\pm 6.0}$	$77.6^{\pm 6.0}$	$67.0^{\pm 2.7}$	$56.9^{\pm 2.0}$	$46.3^{\pm 2.0}$	$37.8^{\pm 1.3}$
10.5	$78.2^{\pm 5.3}$	$69.2^{\pm 3.3}$	$76.8^{\pm 4.0}$	$88.5^{\pm 6.7}$	$64.1^{\pm 6.0}$	$62.6^{\pm 2.7}$	$61.0^{\pm 2.0}$	$45.7^{\pm 2.0}$	$40.6^{\pm 1.3}$
10.7	$70.4^{\pm 4.7}$	$72.6^{\pm 3.3}$	$67.2^{\pm 4.0}$	$67.0^{\pm 6.0}$	$63.1^{\pm 6.0}$	$60.9^{\pm 2.7}$	$62.4^{\pm 2.0}$	$39.9^{\pm 1.3}$	$40.9^{\pm 1.3}$
10.8	$72.3^{\pm 4.7}$	$76.5^{\pm 3.3}$	$81.5^{\pm 4.0}$	$74.7^{\pm 6.7}$	$77.3^{\pm 6.0}$	$58.7^{\pm 2.0}$	$56.2^{\pm 2.0}$	$45.2^{\pm 2.0}$	$40.6^{\pm 1.3}$
11.0	$78.2^{\pm 5.3}$	$78.5^{\pm 3.3}$	$78.7^{\pm 4.0}$	$69.1^{\pm 6.0}$	$62.6^{\pm 6.0}$	$58.2^{\pm 2.0}$	$57.7^{\pm 2.0}$	$44.5^{\pm 2.0}$	$39.8^{\pm 1.3}$
11.1	$72.7^{\pm 4.7}$	$76.8^{\pm 3.3}$	$76.5^{\pm 4.0}$	$76.0^{\pm 6.7}$	$80.1^{\pm 6.7}$	$59.9^{\pm 2.7}$	$61.0^{\pm 2.0}$	$44.0^{\pm 2.0}$	$39.5^{\pm 1.3}$
11.3	$66.5^{\pm 4.7}$	$73.8^{\pm 3.3}$	$68.7^{\pm 4.0}$	$72.3^{\pm 6.7}$	$70.4^{\pm 6.0}$	$60.2^{\pm 2.7}$	$58.2^{\pm 2.0}$	$45.5^{\pm 2.0}$	$40.5^{\pm 1.3}$
11.4	$72.6^{\pm 5.3}$	$80.1^{\pm 4.0}$	$64.9^{\pm 4.0}$	$71.2^{\pm 6.7}$	$70.1^{\pm 6.0}$	$64.6^{\pm 2.7}$	$55.0^{\pm 2.0}$	$42.0^{\pm 2.0}$	$37.6^{\pm 1.3}$
11.6	$68.7^{\pm 4.7}$	$78.7^{\pm 4.0}$	$71.9^{\pm 4.0}$	$74.6^{\pm 6.7}$	$53.1^{\pm 5.3}$	$64.3^{\pm 2.7}$	$57.3^{\pm 2.0}$	$46.3^{\pm 2.0}$	$39.5^{\pm 1.3}$
11.7	$73.0^{\pm 5.3}$	$65.0^{\pm 3.3}$	$75.9^{\pm 4.0}$	$64.9^{\pm 6.0}$	$70.9^{\pm 6.0}$	$60.4^{\pm 2.7}$	$56.5^{\pm 2.0}$	$45.2^{\pm 2.0}$	$37.4^{\pm 1.3}$
11.9	$72.7^{\pm 5.3}$	$75.0^{\pm 3.3}$	$68.8^{\pm 4.0}$	$83.6^{\pm 7.3}$	$66.8^{\pm 6.0}$	$64.9^{\pm 2.7}$	$57.0^{\pm 2.0}$	$39.5^{\pm 2.0}$	$40.1^{\pm 1.3}$

Tab. A.1: Double-differential cross sections for the ^{7}Li(d,^{2}He)^{7}He reaction for various scattering angles.

E$_x$, MeV	0.0°–1.0°	1.0°–2.0°	2.0°–3.0°	3.7°–4.7°	4.7°–5.7°	5.9°–6.9°	6.9°–7.9°	9.3°–10.3°	10.3°–11.3°
12.0	69.2 $^{\pm 4.7}$	73.5 $^{\pm 3.3}$	75.8 $^{\pm 4.0}$	68.3 $^{\pm 6.7}$	68.4 $^{\pm 6.0}$	55.0 $^{\pm 2.7}$	58.0 $^{\pm 2.0}$	38.5 $^{\pm 1.3}$	38.5 $^{\pm 1.3}$
12.2	79.8 $^{\pm 5.3}$	68.2 $^{\pm 3.3}$	64.0 $^{\pm 4.0}$	61.9 $^{\pm 6.0}$	67.9 $^{\pm 6.0}$	60.2 $^{\pm 2.7}$	55.6 $^{\pm 2.0}$	40.1 $^{\pm 2.0}$	37.4 $^{\pm 1.3}$
12.3	63.3 $^{\pm 4.7}$	65.2 $^{\pm 3.3}$	64.0 $^{\pm 4.0}$	65.4 $^{\pm 6.0}$	66.6 $^{\pm 6.0}$	60.8 $^{\pm 2.7}$	57.5 $^{\pm 2.0}$	44.2 $^{\pm 2.0}$	40.1 $^{\pm 1.3}$
12.5	69.3 $^{\pm 5.3}$	72.7 $^{\pm 4.0}$	66.1 $^{\pm 4.0}$	72.9 $^{\pm 6.7}$	65.0 $^{\pm 6.0}$	55.0 $^{\pm 2.7}$	56.5 $^{\pm 2.0}$	40.8 $^{\pm 2.0}$	40.0 $^{\pm 1.3}$
12.6	71.0 $^{\pm 5.3}$	69.0 $^{\pm 3.3}$	63.3 $^{\pm 4.0}$	78.7 $^{\pm 6.7}$	66.5 $^{\pm 6.0}$	57.9 $^{\pm 2.7}$	58.9 $^{\pm 2.0}$	42.8 $^{\pm 2.0}$	38.1 $^{\pm 1.3}$
12.8	61.9 $^{\pm 4.7}$	62.1 $^{\pm 3.3}$	57.8 $^{\pm 4.0}$	72.0 $^{\pm 6.7}$	77.7 $^{\pm 6.7}$	56.2 $^{\pm 2.7}$	55.7 $^{\pm 2.0}$	41.3 $^{\pm 2.0}$	38.1 $^{\pm 1.3}$
12.9	75.1 $^{\pm 5.3}$	62.6 $^{\pm 3.3}$	71.0 $^{\pm 4.0}$	74.6 $^{\pm 6.7}$	54.6 $^{\pm 6.0}$	59.2 $^{\pm 2.7}$	55.9 $^{\pm 2.0}$	42.6 $^{\pm 2.0}$	38.2 $^{\pm 1.3}$
13.1	68.5 $^{\pm 5.3}$	66.5 $^{\pm 3.3}$	62.0 $^{\pm 4.0}$	68.0 $^{\pm 6.7}$	59.7 $^{\pm 6.0}$	56.0 $^{\pm 2.7}$	52.8 $^{\pm 2.0}$	39.3 $^{\pm 2.0}$	37.4 $^{\pm 1.3}$
13.2	66.7 $^{\pm 5.3}$	64.0 $^{\pm 3.3}$	66.5 $^{\pm 4.0}$	61.1 $^{\pm 6.0}$	69.9 $^{\pm 6.7}$	59.8 $^{\pm 2.7}$	59.7 $^{\pm 2.7}$	37.3 $^{\pm 2.0}$	34.8 $^{\pm 1.3}$
13.4	69.4 $^{\pm 5.3}$	67.5 $^{\pm 4.0}$	64.7 $^{\pm 4.0}$	53.5 $^{\pm 6.0}$	52.8 $^{\pm 6.0}$	56.9 $^{\pm 2.7}$	55.2 $^{\pm 2.0}$	39.8 $^{\pm 2.0}$	34.3 $^{\pm 1.3}$
13.5	71.5 $^{\pm 5.3}$	70.1 $^{\pm 4.0}$	64.3 $^{\pm 4.0}$	68.0 $^{\pm 6.7}$	47.3 $^{\pm 5.3}$	56.0 $^{\pm 2.7}$	51.6 $^{\pm 2.0}$	38.8 $^{\pm 2.0}$	35.7 $^{\pm 1.3}$
13.7	69.2 $^{\pm 5.3}$	71.8 $^{\pm 4.0}$	61.0 $^{\pm 4.0}$	73.3 $^{\pm 7.3}$	66.8 $^{\pm 6.7}$	51.9 $^{\pm 2.7}$	54.3 $^{\pm 2.0}$	36.9 $^{\pm 2.0}$	39.4 $^{\pm 1.3}$
13.8	67.7 $^{\pm 5.3}$	62.8 $^{\pm 3.3}$	62.8 $^{\pm 4.0}$	61.1 $^{\pm 6.7}$	67.7 $^{\pm 6.7}$	58.3 $^{\pm 2.7}$	57.0 $^{\pm 2.7}$	38.3 $^{\pm 2.0}$	40.0 $^{\pm 1.3}$
14.0	71.8 $^{\pm 5.3}$	62.2 $^{\pm 3.3}$	77.5 $^{\pm 4.7}$	75.6 $^{\pm 7.3}$	61.3 $^{\pm 6.0}$	56.4 $^{\pm 2.7}$	54.9 $^{\pm 2.7}$	36.5 $^{\pm 2.0}$	37.9 $^{\pm 1.3}$

Tab. A.1: Double-differential cross sections for the ^{7}Li(d,^{2}He)^{7}He reaction for various scattering angles.

E_x, MeV	0.0°–1.0°	1.0°–2.0°	2.0°–3.0°	3.7°–4.7°	4.7°–5.7°	5.9°–6.9°	6.9°–7.9°	9.3°–10.3°	10.3°–11.3°
14.1	70.7 $^{\pm 5.3}$	70.3 $^{\pm 4.0}$	63.8 $^{\pm 4.0}$	62.1 $^{\pm 6.7}$	71.1 $^{\pm 6.7}$	51.4 $^{\pm 2.7}$	52.4 $^{\pm 2.7}$	41.0 $^{\pm 2.0}$	36.6 $^{\pm 1.3}$
14.3	61.1 $^{\pm 5.3}$	74.0 $^{\pm 4.0}$	66.0 $^{\pm 4.7}$	63.5 $^{\pm 6.7}$	63.5 $^{\pm 6.7}$	53.1 $^{\pm 2.7}$	53.3 $^{\pm 2.7}$	39.4 $^{\pm 2.0}$	37.8 $^{\pm 1.3}$
14.4	67.7 $^{\pm 5.3}$	70.8 $^{\pm 4.0}$	74.1 $^{\pm 4.7}$	51.1 $^{\pm 6.0}$	63.5 $^{\pm 6.7}$	56.4 $^{\pm 2.7}$	54.2 $^{\pm 2.7}$	41.8 $^{\pm 2.0}$	35.6 $^{\pm 1.3}$
14.6	77.8 $^{\pm 6.0}$	68.4 $^{\pm 4.0}$	66.5 $^{\pm 4.7}$	62.7 $^{\pm 6.7}$	55.4 $^{\pm 6.0}$	55.6 $^{\pm 2.7}$	61.0 $^{\pm 2.7}$	41.6 $^{\pm 2.0}$	41.8 $^{\pm 1.3}$
14.7	68.3 $^{\pm 5.3}$	75.9 $^{\pm 4.0}$	65.4 $^{\pm 4.7}$	69.6 $^{\pm 7.3}$	51.2 $^{\pm 6.0}$	61.2 $^{\pm 2.7}$	60.2 $^{\pm 2.7}$	41.7 $^{\pm 2.0}$	37.2 $^{\pm 1.3}$
14.9	72.4 $^{\pm 6.0}$	81.1 $^{\pm 4.7}$	80.6 $^{\pm 5.3}$	66.5 $^{\pm 7.3}$	63.4 $^{\pm 6.7}$	58.7 $^{\pm 2.7}$	61.0 $^{\pm 2.7}$	41.8 $^{\pm 2.0}$	39.9 $^{\pm 1.3}$
15.0	74.4 $^{\pm 6.0}$	77.5 $^{\pm 4.0}$	71.2 $^{\pm 4.7}$	66.3 $^{\pm 7.3}$	66.4 $^{\pm 6.7}$	61.4 $^{\pm 2.7}$	59.7 $^{\pm 2.7}$	50.2 $^{\pm 2.0}$	41.2 $^{\pm 1.3}$
15.2	87.3 $^{\pm 6.7}$	81.3 $^{\pm 4.7}$	71.0 $^{\pm 4.7}$	90.0 $^{\pm 8.7}$	76.8 $^{\pm 7.3}$	63.7 $^{\pm 2.7}$	62.7 $^{\pm 2.7}$	49.9 $^{\pm 2.0}$	43.6 $^{\pm 2.0}$
15.3	80.0 $^{\pm 6.0}$	77.3 $^{\pm 4.7}$	73.0 $^{\pm 4.7}$	86.4 $^{\pm 8.0}$	72.0 $^{\pm 7.3}$	71.2 $^{\pm 3.3}$	68.3 $^{\pm 2.7}$	48.9 $^{\pm 2.0}$	47.2 $^{\pm 2.0}$
15.5	80.7 $^{\pm 6.0}$	85.4 $^{\pm 4.7}$	79.8 $^{\pm 5.3}$	77.1 $^{\pm 8.0}$	90.4 $^{\pm 8.0}$	69.6 $^{\pm 3.3}$	69.1 $^{\pm 2.7}$	51.5 $^{\pm 2.0}$	42.2 $^{\pm 2.0}$
15.6	79.1 $^{\pm 6.0}$	85.6 $^{\pm 4.7}$	85.1 $^{\pm 5.3}$	65.6 $^{\pm 7.3}$	72.0 $^{\pm 7.3}$	70.9 $^{\pm 3.3}$	65.3 $^{\pm 2.7}$	54.0 $^{\pm 2.0}$	47.0 $^{\pm 2.0}$
15.8	84.9 $^{\pm 6.7}$	80.5 $^{\pm 4.7}$	95.3 $^{\pm 6.0}$	71.7 $^{\pm 8.0}$	87.8 $^{\pm 8.0}$	73.3 $^{\pm 3.3}$	65.5 $^{\pm 2.7}$	48.6 $^{\pm 2.0}$	48.4 $^{\pm 2.0}$
15.9	87.9 $^{\pm 6.7}$	89.9 $^{\pm 4.7}$	87.8 $^{\pm 5.3}$	65.6 $^{\pm 7.3}$	82.5 $^{\pm 8.0}$	76.0 $^{\pm 3.3}$	65.8 $^{\pm 2.7}$	52.9 $^{\pm 2.0}$	46.6 $^{\pm 2.0}$
16.1	90.5 $^{\pm 6.7}$	91.4 $^{\pm 4.7}$	75.7 $^{\pm 5.3}$	75.5 $^{\pm 8.0}$	90.8 $^{\pm 8.7}$	71.6 $^{\pm 3.3}$	77.6 $^{\pm 3.3}$	48.7 $^{\pm 2.0}$	49.4 $^{\pm 2.0}$

Tab. A.1: Double-differential cross sections for the ^{7}Li(d,^{2}He)^{7}He reaction for various scattering angles.

E$_x$, MeV	0.0°–1.0°	1.0°–2.0°	2.0°–3.0°	3.7°–4.7°	4.7°–5.7°	5.9°–6.9°	6.9°–7.9°	9.3°–10.3°	10.3°–11.3°
16.2	$84.3^{\pm 6.7}$	$86.7^{\pm 4.7}$	$78.3^{\pm 5.3}$	$85.4^{\pm 8.7}$	$71.5^{\pm 7.3}$	$69.0^{\pm 3.3}$	$70.7^{\pm 3.3}$	$53.8^{\pm 2.7}$	$51.6^{\pm 2.0}$
16.4	$84.9^{\pm 6.7}$	$89.4^{\pm 5.3}$	$86.4^{\pm 6.0}$	$77.8^{\pm 8.0}$	$70.7^{\pm 7.3}$	$68.5^{\pm 3.3}$	$72.6^{\pm 3.3}$	$57.2^{\pm 2.7}$	$47.4^{\pm 2.0}$
16.5	$76.2^{\pm 6.7}$	$87.7^{\pm 5.3}$	$81.9^{\pm 6.0}$	$61.6^{\pm 7.3}$	$84.7^{\pm 8.7}$	$74.2^{\pm 3.3}$	$68.6^{\pm 3.3}$	$55.4^{\pm 2.7}$	$50.2^{\pm 2.0}$
16.7	$79.4^{\pm 6.7}$	$89.7^{\pm 5.3}$	$90.5^{\pm 6.0}$	$91.1^{\pm 9.3}$	$80.8^{\pm 8.0}$	$77.5^{\pm 3.3}$	$77.6^{\pm 3.3}$	$59.1^{\pm 2.7}$	$52.3^{\pm 2.0}$
16.8	$105.6^{\pm 8.0}$	$99.7^{\pm 5.3}$	$92.2^{\pm 6.0}$	$82.1^{\pm 8.7}$	$75.3^{\pm 8.0}$	$75.2^{\pm 3.3}$	$75.5^{\pm 3.3}$	$57.8^{\pm 2.7}$	$51.5^{\pm 2.0}$
17.0	$96.0^{\pm 7.3}$	$82.5^{\pm 5.3}$	$89.1^{\pm 6.0}$	$84.2^{\pm 8.7}$	$81.3^{\pm 8.7}$	$76.0^{\pm 3.3}$	$73.5^{\pm 3.3}$	$52.1^{\pm 2.7}$	$56.4^{\pm 2.0}$
17.1	$81.4^{\pm 6.7}$	$97.0^{\pm 5.3}$	$89.9^{\pm 6.0}$	$74.3^{\pm 8.7}$	$82.0^{\pm 8.7}$	$71.7^{\pm 3.3}$	$72.0^{\pm 3.3}$	$59.5^{\pm 2.7}$	$51.8^{\pm 2.0}$
17.3	$87.7^{\pm 7.3}$	$93.7^{\pm 5.3}$	$90.2^{\pm 6.0}$	$72.1^{\pm 8.7}$	$72.7^{\pm 8.0}$	$76.4^{\pm 3.3}$	$71.4^{\pm 3.3}$	$58.7^{\pm 2.7}$	$61.0^{\pm 2.0}$
17.4	$94.6^{\pm 7.3}$	$91.2^{\pm 5.3}$	$96.5^{\pm 6.7}$	$86.8^{\pm 9.3}$	$87.9^{\pm 9.3}$	$88.8^{\pm 4.0}$	$78.6^{\pm 3.3}$	$61.0^{\pm 2.7}$	$55.3^{\pm 2.0}$
17.6	$89.6^{\pm 7.3}$	$99.7^{\pm 6.0}$	$82.5^{\pm 6.0}$	$77.0^{\pm 8.7}$	$82.8^{\pm 8.7}$	$84.4^{\pm 4.0}$	$73.0^{\pm 3.3}$	$63.3^{\pm 2.7}$	$57.5^{\pm 2.0}$
17.7	$96.6^{\pm 8.0}$	$93.1^{\pm 5.3}$	$107.6^{\pm 7.3}$	$93.7^{\pm 10.0}$	$79.1^{\pm 8.7}$	$85.1^{\pm 4.0}$	$69.8^{\pm 3.3}$	$56.1^{\pm 2.7}$	$57.2^{\pm 2.0}$
17.9	$98.7^{\pm 8.0}$	$90.8^{\pm 5.3}$	$90.3^{\pm 6.7}$	$94.4^{\pm 10.0}$	$71.5^{\pm 8.7}$	$76.1^{\pm 4.0}$	$68.2^{\pm 3.3}$	$58.8^{\pm 2.7}$	$56.8^{\pm 2.0}$
18.0	$90.4^{\pm 8.0}$	$86.5^{\pm 5.3}$	$88.8^{\pm 6.7}$	$94.8^{\pm 10.0}$	$89.6^{\pm 9.3}$	$71.3^{\pm 4.0}$	$73.4^{\pm 3.3}$	$58.0^{\pm 2.7}$	$56.8^{\pm 2.0}$
18.2	$69.5^{\pm 6.7}$	$96.7^{\pm 6.0}$	$113.6^{\pm 7.3}$	$78.1^{\pm 9.3}$	$96.4^{\pm 10.0}$	$73.7^{\pm 4.0}$	$72.6^{\pm 3.3}$	$57.4^{\pm 2.7}$	$55.2^{\pm 2.0}$

Tab. A.1: Double-differential cross sections for the ^{7}Li(d,^{2}He)^{7}He reaction for various scattering angles.

E_x, MeV	0.0°–1.0°	1.0°–2.0°	2.0°–3.0°	3.7°–4.7°	4.7°–5.7°	5.9°–6.9°	6.9°–7.9°	9.3°–10.3°	10.3°–11.3°
18.3	$89.6^{\pm 8.0}$	$103.1^{\pm 6.0}$	$93.5^{\pm 7.3}$	$86.4^{\pm 10.0}$	$73.9^{\pm 8.7}$	$80.4^{\pm 4.0}$	$69.1^{\pm 3.3}$	$60.1^{\pm 2.7}$	$57.4^{\pm 2.7}$
18.5	$82.2^{\pm 7.3}$	$98.3^{\pm 6.0}$	$91.2^{\pm 7.3}$	$88.0^{\pm 10.0}$	$86.6^{\pm 9.3}$	$78.4^{\pm 4.0}$	$67.8^{\pm 3.3}$	$61.5^{\pm 2.7}$	$55.2^{\pm 2.0}$
18.6	$86.6^{\pm 8.0}$	$88.1^{\pm 6.0}$	$90.1^{\pm 7.3}$	$94.5^{\pm 10.7}$	$56.8^{\pm 8.0}$	$74.8^{\pm 4.0}$	$71.5^{\pm 3.3}$	$57.0^{\pm 2.7}$	$54.3^{\pm 2.0}$
18.8	$102.0^{\pm 8.7}$	$105.2^{\pm 6.7}$	$85.0^{\pm 6.7}$	$81.7^{\pm 10.0}$	$76.0^{\pm 9.3}$	$69.0^{\pm 4.0}$	$73.3^{\pm 4.0}$	$60.4^{\pm 2.7}$	$54.9^{\pm 2.7}$
18.9	$108.8^{\pm 9.3}$	$96.5^{\pm 6.0}$	$89.5^{\pm 7.3}$	$62.4^{\pm 8.7}$	$58.9^{\pm 8.0}$	$70.3^{\pm 4.0}$	$73.4^{\pm 4.0}$	$62.1^{\pm 3.3}$	$52.8^{\pm 2.7}$
19.1	$89.5^{\pm 8.0}$	$80.7^{\pm 6.0}$	$92.4^{\pm 7.3}$	$81.8^{\pm 10.0}$	$69.2^{\pm 8.7}$	$72.3^{\pm 4.0}$	$78.9^{\pm 4.0}$	$60.2^{\pm 3.3}$	$61.2^{\pm 2.7}$
19.2	$83.5^{\pm 8.0}$	$96.3^{\pm 6.7}$	$89.5^{\pm 7.3}$	$99.8^{\pm 11.3}$	$53.9^{\pm 8.0}$	$78.6^{\pm 4.0}$	$73.8^{\pm 4.0}$	$66.2^{\pm 3.3}$	$53.4^{\pm 2.7}$
19.4	$110.9^{\pm 9.3}$	$92.6^{\pm 6.7}$	$91.3^{\pm 7.3}$	$106.5^{\pm 12.0}$	$63.3^{\pm 8.7}$	$76.0^{\pm 4.0}$	$78.4^{\pm 4.0}$	$60.3^{\pm 3.3}$	$58.6^{\pm 2.7}$
19.5	$99.1^{\pm 8.7}$	$86.6^{\pm 6.0}$	$101.4^{\pm 8.0}$	$98.0^{\pm 11.3}$	$82.8^{\pm 10.0}$	$78.8^{\pm 4.7}$	$65.4^{\pm 4.0}$	$63.6^{\pm 3.3}$	$55.9^{\pm 2.7}$
19.7	$90.7^{\pm 8.7}$	$89.4^{\pm 6.7}$	$94.5^{\pm 8.0}$	$80.8^{\pm 10.7}$	$86.5^{\pm 10.7}$	$73.5^{\pm 4.0}$	$71.7^{\pm 4.0}$	$61.2^{\pm 3.3}$	$56.3^{\pm 2.7}$
19.8	$83.2^{\pm 8.7}$	$90.1^{\pm 6.7}$	$78.7^{\pm 7.3}$	$84.3^{\pm 10.7}$	$71.2^{\pm 9.3}$	$77.4^{\pm 4.7}$	$74.9^{\pm 4.0}$	$59.5^{\pm 3.3}$	$58.0^{\pm 2.7}$
20.0	$101.7^{\pm 9.3}$	$79.6^{\pm 6.0}$	$86.1^{\pm 8.0}$	$60.8^{\pm 9.3}$	$65.4^{\pm 9.3}$	$82.5^{\pm 4.7}$	$75.3^{\pm 4.0}$	$61.0^{\pm 3.3}$	$60.4^{\pm 2.7}$
20.1	$87.4^{\pm 8.7}$	$91.7^{\pm 6.7}$	$90.7^{\pm 8.0}$	$89.8^{\pm 11.3}$	$74.7^{\pm 10.0}$	$71.3^{\pm 4.7}$	$81.7^{\pm 4.7}$	$67.2^{\pm 3.3}$	$52.0^{\pm 2.7}$
20.3	$95.4^{\pm 9.3}$	$90.9^{\pm 6.7}$	$95.5^{\pm 8.7}$	$63.7^{\pm 9.3}$	$81.6^{\pm 10.7}$	$80.7^{\pm 4.7}$	$73.8^{\pm 4.0}$	$65.2^{\pm 3.3}$	$58.5^{\pm 2.7}$

Tab. A.1: Double-differential cross sections for the ^{7}Li(d,^{2}He)^{7}He reaction for various scattering angles.

E$_x$, MeV	0.0°–1.0°	1.0°–2.0°	2.0°–3.0°	3.7°–4.7°	4.7°–5.7°	5.9°–6.9°	6.9°–7.9°	9.3°–10.3°	10.3°–11.3°
20.4	80.4 $^{\pm 8.7}$	87.8 $^{\pm 6.7}$	89.0 $^{\pm 8.7}$	80.2 $^{\pm 10.7}$	65.3 $^{\pm 10.0}$	72.9 $^{\pm 4.7}$	71.5 $^{\pm 4.0}$	57.9 $^{\pm 3.3}$	59.6 $^{\pm 2.7}$
20.6	79.7 $^{\pm 8.7}$	90.6 $^{\pm 6.7}$	81.1 $^{\pm 8.0}$	51.7 $^{\pm 8.7}$	75.1 $^{\pm 10.7}$	73.7 $^{\pm 4.7}$	69.5 $^{\pm 4.0}$	67.0 $^{\pm 3.3}$	58.3 $^{\pm 2.7}$
20.7	90.5 $^{\pm 9.3}$	93.9 $^{\pm 7.3}$	75.0 $^{\pm 8.0}$	65.1 $^{\pm 10.0}$	87.7 $^{\pm 11.3}$	83.0 $^{\pm 4.7}$	67.6 $^{\pm 4.0}$	66.2 $^{\pm 4.0}$	52.7 $^{\pm 2.7}$
20.9	111.6 $^{\pm 10.7}$	85.6 $^{\pm 6.7}$	77.6 $^{\pm 8.0}$	91.6 $^{\pm 12.0}$	69.8 $^{\pm 10.0}$	68.6 $^{\pm 4.7}$	61.5 $^{\pm 4.0}$	61.0 $^{\pm 3.3}$	60.0 $^{\pm 2.7}$
21.0	97.6 $^{\pm 10.0}$	75.6 $^{\pm 6.7}$	77.0 $^{\pm 8.0}$	76.2 $^{\pm 11.3}$	57.7 $^{\pm 9.3}$	78.4 $^{\pm 4.7}$	73.1 $^{\pm 4.7}$	64.9 $^{\pm 4.0}$	61.3 $^{\pm 2.7}$
21.2	77.5 $^{\pm 9.3}$	86.1 $^{\pm 7.3}$	76.2 $^{\pm 8.7}$	75.4 $^{\pm 11.3}$	65.8 $^{\pm 10.7}$	69.1 $^{\pm 4.7}$	67.3 $^{\pm 4.0}$	50.6 $^{\pm 3.3}$	51.4 $^{\pm 2.7}$
21.3	77.3 $^{\pm 9.3}$	75.6 $^{\pm 6.7}$	91.1 $^{\pm 9.3}$	66.9 $^{\pm 10.7}$	67.3 $^{\pm 10.7}$	73.8 $^{\pm 4.7}$	71.4 $^{\pm 4.7}$	56.5 $^{\pm 3.3}$	61.3 $^{\pm 3.3}$
21.5	64.1 $^{\pm 8.7}$	81.7 $^{\pm 7.3}$	79.6 $^{\pm 8.7}$	61.8 $^{\pm 10.7}$	74.3 $^{\pm 11.3}$	87.2 $^{\pm 5.3}$	70.0 $^{\pm 4.7}$	58.8 $^{\pm 4.0}$	56.0 $^{\pm 2.7}$
21.6	97.5 $^{\pm 10.7}$	85.7 $^{\pm 7.3}$	73.9 $^{\pm 8.7}$	88.1 $^{\pm 12.7}$	66.5 $^{\pm 10.7}$	68.3 $^{\pm 4.7}$	69.3 $^{\pm 4.7}$	57.1 $^{\pm 4.0}$	56.0 $^{\pm 2.7}$
21.8	72.7 $^{\pm 9.3}$	81.1 $^{\pm 7.3}$	90.8 $^{\pm 10.0}$	51.7 $^{\pm 10.0}$	42.2 $^{\pm 8.7}$	69.3 $^{\pm 5.3}$	77.9 $^{\pm 4.7}$	59.9 $^{\pm 4.0}$	51.7 $^{\pm 2.7}$
21.9	80.9 $^{\pm 10.0}$	73.7 $^{\pm 7.3}$	73.2 $^{\pm 8.7}$	99.4 $^{\pm 14.0}$	51.2 $^{\pm 10.0}$	63.2 $^{\pm 4.7}$	62.1 $^{\pm 4.7}$	59.7 $^{\pm 4.0}$	61.6 $^{\pm 3.3}$
22.1	82.0 $^{\pm 10.0}$	71.7 $^{\pm 7.3}$	70.6 $^{\pm 8.7}$	71.2 $^{\pm 12.0}$	74.4 $^{\pm 12.0}$	74.4 $^{\pm 5.3}$	65.1 $^{\pm 4.7}$	55.2 $^{\pm 4.0}$	54.0 $^{\pm 3.3}$
22.2	77.9 $^{\pm 10.0}$	85.1 $^{\pm 8.0}$	85.0 $^{\pm 10.0}$	67.8 $^{\pm 12.0}$	67.3 $^{\pm 11.3}$	72.8 $^{\pm 5.3}$	65.3 $^{\pm 4.7}$	51.6 $^{\pm 4.0}$	58.5 $^{\pm 3.3}$
22.4	79.1 $^{\pm 10.0}$	75.2 $^{\pm 7.3}$	56.3 $^{\pm 8.0}$	76.3 $^{\pm 12.7}$	59.9 $^{\pm 10.7}$	74.1 $^{\pm 5.3}$	61.0 $^{\pm 4.7}$	52.5 $^{\pm 4.0}$	54.7 $^{\pm 3.3}$

Tab. A.1: Double-differential cross sections for the ^{7}Li(d,^{2}He)^{7}He reaction for various scattering angles.

E_x, MeV	0.0°–1.0°	1.0°–2.0°	2.0°–3.0°	3.7°–4.7°	4.7°–5.7°	5.9°–6.9°	6.9°–7.9°	9.3°–10.3°	10.3°–11.3°
22.5	70.9 $^{\pm 10.0}$	77.1 $^{\pm 8.0}$	79.3 $^{\pm 10.0}$	66.2 $^{\pm 12.0}$	46.0 $^{\pm 10.0}$	72.9 $^{\pm 5.3}$	65.2 $^{\pm 4.7}$	64.2 $^{\pm 4.0}$	62.2 $^{\pm 3.3}$
22.7	90.7 $^{\pm 11.3}$	90.0 $^{\pm 8.7}$	65.4 $^{\pm 9.3}$	51.0 $^{\pm 10.7}$	60.3 $^{\pm 11.3}$	74.6 $^{\pm 6.0}$	60.1 $^{\pm 4.7}$	54.5 $^{\pm 4.0}$	51.8 $^{\pm 3.3}$
22.8	80.9 $^{\pm 10.7}$	87.2 $^{\pm 8.7}$	59.2 $^{\pm 8.7}$	75.2 $^{\pm 13.3}$	62.6 $^{\pm 11.3}$	68.8 $^{\pm 5.3}$	65.5 $^{\pm 4.7}$	45.6 $^{\pm 4.0}$	53.8 $^{\pm 3.3}$
23.0	50.2 $^{\pm 8.7}$	70.6 $^{\pm 8.0}$	51.0 $^{\pm 8.7}$	93.9 $^{\pm 14.7}$	62.7 $^{\pm 12.0}$	79.0 $^{\pm 6.0}$	60.4 $^{\pm 4.7}$	59.6 $^{\pm 4.0}$	51.9 $^{\pm 3.3}$
23.1	66.8 $^{\pm 10.0}$	73.2 $^{\pm 8.0}$	68.7 $^{\pm 10.0}$	66.2 $^{\pm 12.7}$	62.7 $^{\pm 12.0}$	61.4 $^{\pm 5.3}$	67.2 $^{\pm 5.3}$	55.3 $^{\pm 4.0}$	49.2 $^{\pm 3.3}$
23.3	65.9 $^{\pm 10.0}$	63.6 $^{\pm 7.3}$	45.0 $^{\pm 8.0}$	63.6 $^{\pm 12.7}$	60.4 $^{\pm 12.0}$	51.4 $^{\pm 5.3}$	74.0 $^{\pm 5.3}$	50.7 $^{\pm 4.0}$	50.5 $^{\pm 3.3}$
23.4	63.1 $^{\pm 10.0}$	70.3 $^{\pm 8.0}$	74.0 $^{\pm 10.7}$	85.8 $^{\pm 14.7}$	48.3 $^{\pm 10.7}$	56.8 $^{\pm 5.3}$	65.9 $^{\pm 5.3}$	57.6 $^{\pm 4.7}$	54.8 $^{\pm 3.3}$
23.6	60.3 $^{\pm 10.0}$	55.8 $^{\pm 7.3}$	66.3 $^{\pm 10.0}$	52.5 $^{\pm 11.3}$	74.8 $^{\pm 13.3}$	68.2 $^{\pm 6.0}$	59.8 $^{\pm 5.3}$	43.4 $^{\pm 4.0}$	43.3 $^{\pm 3.3}$
23.7	72.3 $^{\pm 11.3}$	58.8 $^{\pm 7.3}$	41.4 $^{\pm 8.0}$	51.7 $^{\pm 12.0}$	44.5 $^{\pm 10.7}$	63.6 $^{\pm 6.0}$	56.9 $^{\pm 5.3}$	51.5 $^{\pm 4.7}$	54.0 $^{\pm 3.3}$
23.9	52.4 $^{\pm 9.3}$	77.1 $^{\pm 8.7}$	51.8 $^{\pm 9.3}$	67.1 $^{\pm 13.3}$	48.8 $^{\pm 11.3}$	56.4 $^{\pm 5.3}$	56.5 $^{\pm 5.3}$	45.9 $^{\pm 4.0}$	47.9 $^{\pm 3.3}$
24.0	78.9 $^{\pm 12.0}$	69.5 $^{\pm 8.7}$	68.8 $^{\pm 11.3}$	69.3 $^{\pm 14.0}$	58.7 $^{\pm 12.7}$	55.0 $^{\pm 5.3}$	57.4 $^{\pm 5.3}$	41.7 $^{\pm 4.0}$	45.5 $^{\pm 3.3}$
24.2	52.2 $^{\pm 10.0}$	61.0 $^{\pm 8.0}$	86.4 $^{\pm 12.7}$	51.4 $^{\pm 12.0}$	33.1 $^{\pm 9.3}$	54.5 $^{\pm 6.0}$	56.4 $^{\pm 5.3}$	50.8 $^{\pm 4.7}$	42.0 $^{\pm 3.3}$
24.3	61.7 $^{\pm 10.7}$	61.9 $^{\pm 8.7}$	77.1 $^{\pm 12.0}$	44.1 $^{\pm 11.3}$	48.6 $^{\pm 12.0}$	50.3 $^{\pm 5.3}$	47.5 $^{\pm 4.7}$	49.6 $^{\pm 4.7}$	48.8 $^{\pm 3.3}$
24.5	65.8 $^{\pm 11.3}$	55.1 $^{\pm 8.0}$	54.8 $^{\pm 10.7}$	57.8 $^{\pm 13.3}$	56.2 $^{\pm 12.7}$	44.5 $^{\pm 5.3}$	61.9 $^{\pm 6.0}$	43.7 $^{\pm 4.7}$	49.8 $^{\pm 4.0}$

Tab. A.1: Double-differential cross sections for the ^{7}Li(d,^{2}He)^{7}He reaction for various scattering angles.

E_x, MeV	0.0°–1.0°	1.0°–2.0°	2.0°–3.0°	3.7°–4.7°	4.7°–5.7°	5.9°–6.9°	6.9°–7.9°	9.3°–10.3°	10.3°–11.3°
24.6	$36.4^{\pm 8.7}$	$67.9^{\pm 9.3}$	$67.2^{\pm 12.0}$	$34.4^{\pm 10.7}$	$58.1^{\pm 13.3}$	$50.0^{\pm 6.0}$	$52.4^{\pm 5.3}$	$40.7^{\pm 4.0}$	$48.3^{\pm 4.0}$
24.8	$68.5^{\pm 12.0}$	$58.9^{\pm 8.7}$	$59.7^{\pm 11.3}$	$84.3^{\pm 16.7}$	$35.0^{\pm 10.7}$	$52.4^{\pm 6.0}$	$54.1^{\pm 5.3}$	$41.7^{\pm 4.7}$	$46.7^{\pm 4.0}$
24.9	$58.1^{\pm 11.3}$	$55.0^{\pm 8.7}$	$46.5^{\pm 10.0}$	$49.9^{\pm 12.7}$	$49.0^{\pm 12.7}$	$53.4^{\pm 6.0}$	$44.7^{\pm 5.3}$	$32.1^{\pm 4.0}$	$41.8^{\pm 3.3}$

References

[1] S.C. Pieper and R.B. Wiringa, Annu. Rev. Nucl. Part. Sci. **51** (2001) 53.

[2] B.R. Barrett, P. Navratil, Acta Phys. Pol. B **33** (2002) 297.

[3] R. Roth, T. Neff, H. Hergert, H. Feldmeier, Nucl. Phys. A **745** (2004) 3.

[4] B. Jonson, Phys. Rep. **389** (2004) 1.

[5] A. Richter, Nucl. Phys. A **751** (2005) 3c.

[6] M. Meister, K. Markenroth, D. Aleksandrov, T. Aumann, L. Axelsson, T. Baumannn, M.J.G. Borge, L.V. Chulkov, W. Dostal, B. Eberlein, Th.W. Elze, H. Emling, C. Forssén, H. Geissel, M. Hellström, R. Holzmann, B. Jonson, J.V. Kratz, R. Kulessa, Y. Leifels, A. Leistenschneider, I. Mukha, G. Münzenberg, F. Nickel, T. Nilsson, G. Nyman, A. Richter, K. Riisager, C. Scheidenberger, G. Schrieder, H. Simon, O. Tengblad, and M.V. Zhukov, Phys. Rev. Lett. **88** (2002) 102501.

[7] R.H. Stokes and P.G. Young, Phys. Rev. Lett. **18** (1967) 611.

[8] A.A. Korsheninnikov, M.S. Golovkov, A. Ozawa, E.A. Kuzmin, E.Yu. Nikolskii, K. Yoshida, B.G. Novatskii, A.A. Ogloblin, I. Tanihata, Z. Fulop, K. Kusaka, K. Morimoto, H. Otsu, H. Petrascu and F. Tokanai, Phys. Rev. Lett. **82** (1999) 3581.

[9] H.G. Bohlen, R. Kalpakchieva, A. Blažević, B. Gebauer, T.N. Massey, W. von Oertzen and S. Thummerer, Phys. Rev. C **64** (2001) 024312.

[10] M.S. Golovkov, A.A. Korsheninnikov, I. Tanihata, D.D. Bogdanov, M.L. Chelnokov, A.S. Fomichev, V.A. Gorshkov, Yu.Ts. Oganessian, A.M. Rodin, S.I. Sidorchuk, S.V. Stepantsov, G.M. Ter-Akopian, R. Wolski, W. Mittig, P. Roussel-Chomaz, H. Savajols, E.A. Kuzmin, E.Yu. Nikolski, B.G. Novatskii and A.A. Ogloblin, Phys. At. Nucl. **64** (2001) 1244.

[11] G.V. Rogachev, P. Boutachkov, A. Aprahamian, F.D. Becchetti, J.P. Bychowski, Y. Chen, G. Chubarian, P.A. DeYoung, V.Z. Goldberg, J.J. Kolata, L.O. Lamm, G.F. Peaslee, M. Quinn, B.B. Skorodumov and A. Wöhr, Phys. Rev. Lett. **92** (2004) 232502.

[12] P. Boutachkov, G.V. Rogachev, V.Z. Goldberg, A. Aprahamian, F.D. Becchetti, J.P. Bychowski, Y. Chen, G. Chubarian, P.A. DeYoung, J.J. Kolata, L.O. Lamm, G.F. Peaslee, M. Quinn, B.B. Skorodumov and A. Wöhr, Phys. Rev. Lett. **95** (2005) 132502.

[13] D. Halderson, Phys. Rev. C **70** (2004) 041603.

[14] F. Skaza, V. Lapoux, N. Keeley, N. Alamanos, E.C. Pollacco, F. Auger, A. Drouart, A. Gillibert, D. Beaumel, E. Becheva, Y. Blumenfeld, F. Delaunay, L. Giot, K.W. Kemper, L. Nalpas, A. Obertelli, A. Pakou, R. Raabe, P. Roussel-Chomaz, J.-L. Sida, J.-A. Scarpaci, S. Stepantsov, R. Wolski, Phys. Rev. C **73** (2006) 044301.

[15] A.H. Wuosmaa, K.E. Rehm, J.P. Greene, D.J. Henderson, R.V.F. Janssens, C.L. Jiang, L. Jisonna, E.F. Moore, R.C. Pardo, M. Paul, D. Peterson, S.C. Pieper, G. Savard, J.P. Schiffer, R.E. Segel, S. Sinha, X. Tang and R.B. Wiringa, Phys. Rev. C **72** (2005) 061301.

[16] D. Frekers, Nucl. Phys. A **731** (2004) 76.

[17] N. Ryezayeva, C. Bäumer, A.M. van den Berg, L.V. Chulkov, D. Frekers, D. De Frenne, E.-W. Grewe, P. Haefner, E. Jacobs, H. Johanson, Y. Kalmykov, A. Negret, P. von Neumann-Cosel, L. Popescu, S. Rakers, A. Richter, G. Schrieder, A. Shevchenko, H. Simon, H.J. Wörtche, Phys. Lett. B, in press.

[18] F. Beck, P. von Neumann-Cosel, A. Richter, N. Ryezayeva, J.P. Schiffer, I.J. Thompson, Phys. Lett. B, submitted.

[19] P.E. Hodgson, *Nuclear Reactions and Nuclear Structure* (Clarendon Press, Oxford, 1971).

[20] A.G. Sitenko, *Lectures in Scattering Theory* (Pergamon Press, Oxford, 1971).

[21] Daphne F. Jackson, *Nuclear Reactions* (Methuen and Co LTD, London, 1970).

[22] S.C. Pieper, R.B. Wiringa and J. Carlson, Phys. Rev. C **70** (2004) 054325.

[23] S.C. Pieper, V.R. Pandharipande, R.B. Wiringa and J. Carlson, Phys. Rev. C **64** (2001) 014001.

[24] S.C. Pieper, Nucl. Phys. A **751** (2005) 516c.

[25] S.C. Pieper, Nucl. Phys. A **701** (2002) 357c.

[26] B.S. Pudliner, V.R. Pandharipande, J. Carlson, S.C. Pieper and R.B. Wiringa, Phys. Rev. C **56** (1997) 1720.

[27] G.R. Satchler, Nucl. Phys. **18** (1960) 110.

[28] G.R. Satchler, Nucl. Phys. **55** (1964) 1.

[29] H. Okamura, Phys. Rev. C **60** (1999) 064602.

[30] R.C. Johnson and P.J.R. Soper, Phys. Rev. C **1** (1970) 976.

[31] M. Yahiro, J.A. Tostevin and R.C. Johnson Phys. Rev. Lett. **62** (1989) 133.

[32] W.G. Love and M.A. Franey, Phys. Rev. C **24** (1981) 1073.

[33] M.A. Franey and W.G. Love, Phys. Rev. C **31** (1985) 488.

[34] B.A. Brown, A. Etchegoyen and W.D.M. Rae, *Computer shell-model code OXBASH* (Michigan State University, Oxford University, Comision Nacional de Energia Atomica Buenos Aires, 1988).

[35] Norman K. Glendenning, *Direct Nuclear Reactions* (Akademic Press, New York, 1983).

[36] T.N. Taddeucci, C.A. Goulding, T.A. Carey, R.C. Byrd, C.D. Goodman, C. Gaarde, J. Larsen, D. Horen, J. Rapaport, E. Sugarbaker, Nucl. Phys. A **469** (1987) 125.

[37] C.D. Goodman, C.A. Goulding, M.B. Greenfield, J. Rapaport, D.E. Bainum, C.C. Foster, W.G. Love and F. Petrovich, Phys. Rev. Lett. **44** (1980) 1755.

[38] R.B. Wiringa, V.G.J. Stoks, R. Schiavilla, Phys. Rev. C **51** (1995) 38.

[39] B.S. Pudliner, V.R. Pandharipande, J. Carlson and R.B. Wiringa, Phys. Rev. Lett. **74** (1995) 4396.

[40] J. Carlson, Phys. Rev. C **36** (1987) 2026.

[41] A.M. Lane and R.G. Thomas, Rev. Mod. Phys. **30** (1958) 257.

[42] G.R. Satchler, L.W. Owen, A.J. Elwyn, G.L. Morgan and R.L. Walter, Nucl. Phys. A **112** (1968) 1.

[43] L.-B. Wang, P. Mueller, K. Bailey, G.W.F. Drake, J.P. Greene, D. Henderson, R.J. Holt, R.V.F. Janssens, C.L. Jiang, Z.-T. Lu, T.P.O. O'Connor, R.C. Pardo, K.E. Rehm, J.P. Schiffer and X.D. Tang, Phys. Rev. Lett. **93** (2004) 142501.

[44] S. Brandenburg, *The superconducting cyclotron AGOR: accelerator for light and heavy ions*, Proc. of the Particle Accelerator Conference, Eds. S. Meyers, A. Pacheco, R. Pascual, C. Petit-Jean-Genaz, J. Poole, Washington USA (1987) 376.

[45] A.M. van den Berg, Nucl. Instr. Meth. B **99** (1995) 637.

[46] V.M. Hannen, *A high-precision study of polarized proton scattering to low-lying states in* ^{11}B, Dissertation, Rijksuniversiteit Groningen (2001).

[47] S. Rakers, *Messung der Gamow-Teller Übergangsstärken in* ^{12}C *und* ^{24}Mg *mit der (d,*^{2}*He)-Reaktion*, Dissertation, Westfälische Wilhelms-Universität Münster (2002).

[48] M.A. de Huu, *Computer program KINEMA*, KVI Program Library, 2001.

[49] H.J. Wörtche, Nucl. Phys. A **687** (2001) 321c.

[50] W. Bertozzi, M.V. Hynes, C.P. Sargent, C. Creswell, P.C. Dunn, A. Hirsch, M. Leitch, B. Norum, F.N. Rad and T. Sasanuma, Nucl. Instr. Meth. **141** (1977) 457.

[51] M. Hagemann, *Exclusive study of spin-isospin excitations in* ^{58}Ni *using the (d,*^{2}*He) charge-exchange reaction*, Dissertation, Universiteit Gent (2001).

[52] M. Hagemann, *Ein auf DSPs basierendes schnelles Auslese- und Online-Datenverarbeitungssystem für ein neues Fokalebenenpolarimeter am KVI*, Diploma thesis, Westfälische Wilhelms-Universität Münster (1997).

[53] M. Hagemann, R. Bassini, A.M. van den Berg, F. Ellinghaus, D. Frekers, V.M. Hannen, T. Häupke, J. Heyse, E. Jacobs, M. Kirsch, B. Krüsemann, S. Rakers, H. Sohlbach, H.J. Wörtche, Nucl. Instr. Meth. A **437** (1999) 459.

[54] F. Zwarts, KVI annual report, 1996.

[55] Computer program PAW++, CERN Program Library, 1995.

[56] R. Schmidt, *VESNA Spur-Rekonstruktion für den ESN-Detektor*, Diploma thesis, Westfälische Wilhelms-Universität Münster (2001).

[57] S. Rakers, F. Ellinghaus, R. Bassini, C. Bäumer, A.M. van den Berg, D. Frekers, D. De Frenne, M. Hagemann, V.M. Hannen, M.N. Harakeh, M. Hartig, R. Henderson, J. Heyse, M.A. de Huu, E. Jacobs, M. Mielke, J.M. Schippers, R. Schmidt, S.Y. van der Werf, H.J. Wörtche, Nucl. Instr. Meth. A **481** (2002) 253.

[58] K.M. Watson, Phys. Rev. **88** (1952) 1163.

[59] A.B. Migdal, J. Exp. Theoret. Phys. USSR **28** (1955) 3.

[60] http://qclam.ikp.physik.tu-darmstadt.de/files/work/he7.

[61] A. Erell, J. Alster, J. Lichtenstadt, M.A. Moinester, J.D. Bowman, M.D. Cooper, F. Irom, H.S. Matis, E. Piasetzky and U. Sennhauser, Phys. Rev. C **34** (1986) 1822.

[62] J. Jänecke, K. Pham, D.A. Roberts, D. Stewart, M.N. Harakeh, G.P.A. Berg, C.C. Foster, J.E. Lisantti, R. Sawafta, E.J. Stephenson, A.M. van den Berg, S.Y. van den Werf, S.E. Muraviev and M.H. Urin, Phys. Rev. C **48** (1993) 2828.

[63] J. Jänecke, A. Annakkage, G.P.A. Berg, B.A. Brown, J.A. Brown, G. Crawley, S. Danczyk, M. Fujiwara, D.J. Mercer, K. Pham, D.A. Roberts, J. Stasko, J.S. Winfield and G.H. Yoo, Phys. Rev. C **54** (1996) 1070.

[64] A. Annakkage, J. Jänecke, J.S. Winfield, G.P.A. Berg, J.A. Brown, G. Crawley, S. Danczyk, M. Fujiwara, D.J. Mercer, K. Pham, D.A. Roberts, J. Stasko, G.H. Yoo, Nucl. Phys. A **648** (1999) 3.

[65] H. Okamura, T. Uesaka, K. Suda, H. Kumasaka, R. Suzuki, A. Tamii, N. Sakamoto and H. Sakai, Phys. Rev. C **66** (2002) 054602.

[66] K.J. Raywood, B.M. Spicer, S. Yen, S.A. Long, M.A. Moinester, R. Abegg, W.P. Alford, A. Celler, T.E. Drake, D. Frekers, P.E. Green, O. Häusser, R.L. Helmer, R.S. Henderson, K.H. Hicks, K.P. Jackson, R.G. Jeppesen, J.D. King, N.S.P. King, C.A. Miller, V.C. Officer, R. Schubank, G.G. Shute, M. Vetterli, J. Watson and A.I. Yavin, Phys. Rev. C **41** (1990) 2836.

[67] P. Haefner, *Hinweise auf eine Soft-Dipole Resonanz im Halo-Kern* ^{6}*He*, Diploma Thesis, Westfälische Wilhelms-Universität Münster (2004).

[68] L. Wang, X. Yang, J. Rapaport, C.D. Goodman, C.C. Foster, Y. Wang, J. Piekarewicz, E. Sugarbaker, D. Marchlenski, S. de Lucia, B. Luther, L. Rybarcyk, T.N. Taddeucci, B.K. Park, Phys. Rev. C **50** (1994) 2438.

[69] S. Strauch and F. Neumeyer, *Computer Program FIT*, TH Darmstadt, 1996.

[70] F. Brady, G.A. Needham, J.L. Romero, C.M. Castaneda, T.D. Ford, J.L. Ullmann and M.L. Webb, Phys. Rev. Lett. **51** (1983) 1320.

[71] T. Yamagata, S. Nakayama, H. Akimune, M. Fujiwara, K. Fushimi, M.B. Greenfield, K. Hara, K.Y. Hara, H. Hashimoto, K. Ichihara, K. Kawase, M. Kinoshita, Y. Matsui, K. Nakanishi, M. Tanaka, H. Utsunomiya and M. Yosoi, Phys. Rev. C **69** (2004) 044313.

[72] S. Nakayama, T. Yamagata, H. Akimune, I. Daito, H. Fujimura, Y. Fujita, M. Fujiwara, K. Fushimi, M.B. Greenfield, H. Kohri, N. Koori, K. Takahisa, A. Tamii, M. Tanaka, and H. Toyokawa, Phys. Rev. Lett. **87** (2001) 122502.

[73] D.R. Tilley, C.M. Cheves, J.L. Godwin, G.M. Hale, H.M. Hofmann, J.H. Kelley, C.G. Sheu, H.R. Weller, Nucl. Phys. A **708** (2002) 3.

[74] M. Palarczyk, C.M. Riedel, D. Dehnhard, M.A. Espy, M.A. Franey, J.L. Langenbrunner, L.C. Bland, D.S. Carman, B. Brinkmöller, R. Madey, Y. Wang, J.W. Watson and N.S. Chant, Phys. Rev. C **58** (1998) 645.

[75] C.M. Riedel, D. Dehnhard, M. Palarczyk, M.A. Espy, M.A. Franey, J.L. Langenbrunner, L.C. Bland, D.S. Carman, B. Brinkmöller, R. Madey, Y. Wang and J.W. Watson, Phys. Rev. C **69** (2004) 024616.

[76] E.W. Grewe, C. Bäumer, A.M. van den Berg, N. Blasi, B. Davids, D. De Frenne, D. Frekers, P. Haefner, M.N. Harakeh, M. Huynyadi, E. Jacobs, B. Junk, A. Korff, A. Negret, P. von Neumann-Cosel, L. Popescu, S. Rakers and H.J. Wörtche, Phys. Rev. C **69** (2004) 064325.

[77] S. Rakers, C. Bäumer, D. Frekers, R. Schmidt, A.M. van den Berg, V.M. Hannen, M.N. Harakeh, M.A. de Huu, H.J. Wörtche, D. De Frenne, M. Hagemann, J. Heyse, E. Jacobs and Y. Fujita, Phys. Rev. C **65** (2002) 044323.

[78] W.W. Daehnick, J.D. Childs and Z. Vrcelj, Phys. Rev. C **21** (1980) 2253.

[79] A. Korff, P. Haefner, C. Bäumer, A.M. van den Berg, N. Blasi, B. Davids, D. De Frenne, R. de Leo, D. Frekers, E.-W. Grewe, M.N. Harakeh, F. Hofmann, M. Hunyadi, E. Jacobs, B.C. Junk, A. Negret, P. von Neumann-Cosel, L. Popescu, S. Rakers, A. Richter and H.J. Wörtche, Phys. Rev. C **70** (2004) 067601.

[80] D. Gupta, C. Samanta, R. Kanungo, Nucl. Phys. A **674** (2000) 77.

[81] S. Cohen and D. Kurath, Nucl. Phys. **73** (1965) 1.

[82] J. Stevenson, B.A. Brown, Y. Chen, J. Clayton, E. Kashy, D. Mikolas, J. Nolen, M. Samuel, B. Sherrill, J.S. Winfield, Z.Q. Xie, R.E. Julies, W.A. Richter, Phys. Rev. C **37** (1988) 2220.

[83] R.B. Wiringa, S.C. Pieper, private communication to A. Richter.

[84] R. Schiavilla and R.B. Wiringa, Phys. Rev. C **65** (2002) 054302.

[85] S. Cohen and D. Kurath, Nucl. Phys. A **101** (1967) 1.

[86] S.M. Austin, N. Anantaraman, W.G. Love, Phys. Rev. Lett. **73** (1994) 30.

[87] T. Neff, H. Feldmeier, Nucl. Phys. A **738** (2004) 357.

[88] A.N. Tikhonov and V.Y. Arsenin, Solutions of Ill-Posed Problems, John Wiley, New York, 1977.

[89] G.M. Petrov, J. Quant. Spectrosc. Radiat. Transfer **72** (2002) 281.

[90] Wolfram Research, Inc., Champaign, IL, 2004.

[91] B.L. Berman and S.C. Fultz, Rev. Mod. Phys. **47** (1975) 713.

[92] N. Michel, W. Naczarewicz, M. Ploszajczak, J. Okolowicz, Phys. Rev. Lett. **89** (2002) 042502.

[93] N. Michel, W. Naczarewicz, M. Płoszajczak, J. Okołowicz, Phys. Rev. C **67** (2003) 054311.

[94] N. Michel, W. Naczarewicz, J. Okołowicz, M. Płoszajeck and J. Rotureau, Acta Phys. Pol. B **35** (2004) 1249.

[95] David N. Schramm and Michael S. Turner, Rev. Mod. Phys. **70** (1998) 303.

[96] Scott Burles, Kenneth M. Nollett, James W. Truran and Michael S. Turner, Phys. Rev. Lett. **82** (1999) 4176.

[97] Scott Burles and David Tytler, Astrophys. J. **499** (1998) 699.

[98] Scott Burles and David Tytler, Astrophys. J. **507** (1998) 732.

[99] Y. Nagai, T.S. Suzuki, T. Kikuchi, T. Shima, T. Kii, H. Sato and M. Igashira, Phys. Rev. C **56** (1997) 3173.

[100] T.S. Suzuki, Y. Nagai, T. Shima, T. Kikuchi, H. Sato, T. Kii and M. Igashira, Astrophys. J. **439** (1995) L59.

[101] E.C. Schreiber, R.S. Canon, B.T. Crowley, C.R. Howell, J.H. Kelley, V.N. Litvinenko, S.O. Nelson, S.H. Park, I.V. Pinayev, R.M. Prior, K. Sabourov, M. Spraker, W. Tornow, Y. Wu, E.A. Wulf and H.R. Weller, Phys. Rev. C **61** (2000) 061604.

[102] W. Tornow, N.G. Czakon, C.R. Howell, A. Hutcheson, J.H. Kelley, V.N. Litvinenko, S.F. Mikhailov, I.V. Pinayev, G.J. Weisel, H. Witala, Phys. Lett. B **574** (2003) 8.

[103] K. Shinohara, T. Okada, S. Morita, J. Phys. Soc. Jap. **4** (1949) 77.

[104] G.R. Bishop, C.H. Collie, H. Halban, A. Hedgran, K. Siegbahn, S. du Toit, R. Wilson, Phys. Rev. **80** (1950) 211.

[105] C.A. Barnes, J.H. Carver, G.H. Stafford and D.H. Wilkinson, Phys. Rev. **86** (1952) 359.

[106] R. Moreh, T.J. Kennett, W.V. Prestwich, Phys. Rev. C **39** (1989) 1247.

[107] K.Y. Hara, H. Utsunomiya, S. Goko, H. Akimune, T. Yamagata, M. Ohta, H. Toyokawa, K. Kudo, A. Uritani, Y. Shibata, Y.-W. Lui and H. Ohgaki, Phys. Rev. D **68** (2003) 072001.

[108] S. Ando, R.H. Cyburt, S.W. Hong and C.H. Hyun, Phys. Rev. C, accepted.

[109] H. Arenhövel and M. Sanzone *Photodisintegration of the Deuteron: A Review of Theory and Experiment* (Springer-Verlag, Wien, 1991).

[110] S. Nakayama, T. Yamagata, H. Akimune, Y. Arimoto, H. Daito, H. Ejiri, H. Fujimura, Y. Fujita, M. Fujiwara, K. Fushimi, M.B. Greenfield, H. Kohri, N. Koori, K. Takahisa, T. Takeuchi, M. Tanaka, K. Yonehara and H.P. Yoshida, Phys. Rev. C **72** (2005) 041001.

[111] G.A. Peterson and W.C. Barber, Phys. Rev. **128** (1962) 812.

[112] E.C. Jones, Jr., W.L. Bendel, L.W. Fagg, R.A. Lindgren, Phys. Rev. C **21** (1980) 1162.

[113] A. Richter, *Operational experience at the S-DALINAC*, Proc. of the Fifth EPAC, Eds. S. Meyers, A. Pacheco, R. Pascual, C. Petit-Jean-Genaz, J. Poole, IOP Publishing, Bristol (1996) 110.

[114] Lawrence W. Fagg, Rev. Mod. Phys. **47** (1975) 683.

[115] P. Mohr, J. Enders, T. Hartmann, H. Kaiser, D. Schiesser, S. Schmitt, S. Volz, F. Wissel, A. Zilges, Nucl. Instr. Meth. A **423** (1999) 480.

[116] M. Knirsch, *Konzeption, Aufbau und Erprobung eines hochauflösenden QCLAM-Elektronenspektrometers mit großem Raumwinkel und hoher Impulsakzeptanz am Elektronenbeschleuniger S-DALINAC*, Dissertation D17, TH Darmstadt (1991).

[117] A.W. Lenhardt, *Entwicklung eines Si-Mikrostreifendetektors für das 169°-Spektrometer am S-DALINAC*, Dissertation D17, TU Darmstadt (2004).

[118] A.W. Lenhardt, U. Bonnes, O. Burda, P. von Neumann-Cosel, M. Platz, A. Richter, S. Watzlawik, Nucl. Instr. Meth. A **562** (2006) 320.

[119] C. Lüttge, *Entwicklung und Aufbau eines Magnetsystems für Elektronenstreuung unter 180° und vollständige Bestimmung der magnetischen Dipol- und Quadrupolstärkeverteilung in* ^{28}Si, Dissertation D17, TH Darmstadt (1994).

[120] C. Lüttge, C. Hofmann, J. Horn, F. Neumeyer, A. Richter, G. Schrieder, E. Spamer, A. Stiller, D.I. Sober, S.K. Matthews, L.W. Fagg, Nucl. Instr. Meth. A **366** (1995) 325.

[121] K.-D. Hummel, *Entwicklung, Aufbau und Inbetriebnahme eines Vieldrahtdriftkammer-Detektorsystems für das QCLAM-Spektrometer am supraleitenden Darmstädter Elektronenbeschleuniger S-DALINAC*, Dissertation D17, TH Darmstadt (1992).

[122] D. Hoffmann, G. Sobotta, K. Becker, H. Genz, A. Richter and G. Schrieder, Nucl. Instr. Meth. **118** (1974) 321.

[123] F. Neumeyer, *Untersuchung magnetischer Kernanregungen in* ^{48}Ca *und* ^{90}Zr *mit hochauflösender Elektronenstreuung unter 180° am S-DALINAC*, Dissertation D17, TH Darmstadt (1997).

[124] F. Hofmann, P. von Neumann-Cosel, F. Neumeyer, C. Rangacharyulu, B. Reitz, A. Richter and G. Schrieder, Phys. Rev. C **65** (2002) 024311.

[125] J. Horn, *Entwicklung und Integration eines schnellen Kontrollsystems für den S-DALINAC und Weiterentwicklung der Vieldrahtdriftkammern in QCLAM-Spektrometer*, Dissertation D17, TH Darmstadt (1997).

[126] H. Überall, *Electron Scattering From Complex Nuclei - Part B*, (Academic Press, New York - London, 1971).

[127] R. Gilman and F. Gross, J. Phys. G: Nucl. Part. Phys. **28** (2002) R37 and references therein.

[128] Yung-Su Tsai, Phys. Rev. **122** (1961) 1898.

[129] L.W. Mo, Y.S. Tsai, Rev. Mod. Phys. **41** (1969) 205.

[130] Edith Borie, Phys. Rev. C **2** (1970) 770.

[131] H. Arenhövel, private communication.

[132] H. Arenhövel, W. Leidemann and E.L. Tomusiak, Eur. Phys. J. A **23** (2005) 147.

[133] Harald W. Grießhammer, Prog. Part. Nucl. Phys. **55** (2005) 215.

[134] S. Christlmeier, *Electrodisintegration of the Deuteron in Effective Field Theory*, Diploma thesis, Technische Universität München (2004).

[135] Harald W. Grießhammer, private communication.

[136] C Bäumer, D. Frekers, E.-W. Grewe, P. Haefner, S. Hollstein, B.C. Junk, A. Korff, S. Rakers, R. Schmidt, A.M. van den Berg, B. Davids, M.N. Harakeh, M. Hunyadi, M.A. de Huu, H.J. Wörtche, N. Blasi, D. De Frenne, E. Jacobs, A. Negret, L. Popescu, R. De Leo, F. Hofmann, P. von Neumann-Cosel, A. Richter, Phys. Rev. C **71** (2005) 044003.

[137] D Ganichot, B. Grossetête, D.B. Isabelle, Nucl. Phys. A **178** (1972) 545.

[138] Dieter Drechsel and Lothar Tiator, Annu. Rev. Nucl. Part. Sci. **54** (2004) 69.

[139] Henry R. Weller and Mohammad W. Ahmed, Mod. Phys. Lett. **18** (2003) 1569.

Danksagung

All jenen, die zum Entstehen und Gelingen dieser Arbeit beigetragen haben, möchte ich an dieser Stelle meinen Dank aussprechen.

Zuallererst möchte ich meinem Doktorvater Herrn Professor Dr. Dr. h. c. mult. Achim Richter danken für die Möglichkeit, diese interessante Arbeit in seiner Arbeitsgruppe an der Technischen Universität Darmstadt durchführen zu können, insbesondere für die Unterstützung während all dieser Jahre. Er hat mir zwei sehr faszinierende und anspruchsvolle Aufgaben gestellt. Durch seine wertvolle Beratung und Motivation hat er mich zur erfolgreiche Lösung dieser Aufgaben ständig geführt.

Herrn Professeor Dr. Jochen Wambach danke ich für die freundliche Übernahme des Korreferates.

Mein besonderer Dank gilt Herrn Professor Dr. Peter von Neumann-Cosel, der mich betreut hat und den Fortgang dieser Arbeit bei jeder Gelegenheit unterstützt. Auch für sein großes Interesse und viele fruchtbare Diskussionen und Anregungen danke ich ihm sehr herzlich.

Herrn Professor Dr. Freder Beck möchte ich für die R-Matrix Analyse der ^{7}Li(d,^{2}He) Daten danken. Er hat durch seine ausgezeichnete Zusammenarbeit und Diskussionsbereitschaft sehr zum Gelingen dieser Arbeit beigetragen.

Mein Dank gilt Herrn Professor Dr. Hartmuth Arenhövel für die Zurverfügungstellung theoretischer Rechnungen.

Bei Herrn Professor Dr. Joachim Enders möchte ich mich für das gründliche Korrekturlesen und die zahlreichen Ratschläge bedanken.

Many thanks go to Professor Dr. Chary Rangacharyulu for fruitful discussions and his permanent interest in the progress of the d(e,e$'$) data analysis.

I would like to express my gratitude to Dr. Leonid Chulkov for his permanent help in the interpretation of the ^{7}Li(d,^{2}He)^{7}He data as well as for sharing his tremendous knowledge and ability in physics of exotic nuclei. It was a great pleasure for me to work together with him these last two years.

Herrn Dr. Harald Genz danke ich besonderes für seine großartige Hilfe und Unterstützung in allen Fragen und Problemen.

Bei allen Mitarbeitern der EUROSUPERNOVA-Kollaboration möchte ich mich für die Hilfe bei der Durchführung des Experimentes am KVI und für die gute Zusammenarbeit bedanken. Für die Hilfe bei der Datenanalyse danke ich insbesondere Herrn Dr. Sven Rakers und Frau Dipl.-Phys. Petra Haefner.

Bei meinen Kollegen und Freunden aus der QCLAM-Gruppe bedanke ich mich für die Teilnahme an den Messschichten. Der Frau Iryna Poltoratska und den Herren Anatoliy Byelikov und Maksym Chernykh möchte ich meinen Dank aussprechen für ihren Einsatz bei der Vorbereitung des Experiments am S-DALINAC. Mein besonderer Dank für die freundliche Unterstützung und enorme Hilfe während der Vorbereitung und Durchfüchrung der beiden Experimente geht an die Herren Dr. Yaroslav Kalmykov und Dr. Artem Shevchenko.

Allen Mietgliedern der Beschleunigergruppe am S-DALINAC danke ich für die Bereitstellung eines exzellenten Strahls und wertvolle Hilfe während des Experiments.

Meine Familie möchte ich herzlich danken, die mich immer unterstüzt hat, wenn auch meistens aus größer geographische Distanz!

Die vorliegende Arbeit wurde gefördert durch Mittel aus dem DFG Graduiertenkolleg 410 ”*Physik und Technik von Beschleunigern*” und dem Sonderforschungsbereich SFB 634 ”*Kernstruktur, nukleare Astrophysik und fundamentale Experimente bei kleinen Impulsüberträgen am supraleitenden Darmstädter Elektronenbeschleuniger S-DALINAC*”.

Lebenslauf

Natalya Ryezayeva

12. August 1979	Geboren in Polyarny, Russland
1986 – 1994	Besuch der Sekundärschule Nr. 4, Kupyansk, Ukraine
1994 – 1996	Besuch des Gymnasiums Nr. 1, Kupyansk, Ukraine
1996 – 2002	Studium der Physik an der Fakultät für Physik und Technik der Kharkiver Staatsuniversität (jetzt *Karazin Kharkiv National University*), Ukraine. Vertiefungsrichtung - Kernphysik
Juli 2001 – Dez. 2001	Diplompraktika am Institut für Kernphysik der Technische Universität Darmstadt
Februar 2002	Abschluss des Studiums mit Diplom Thema: ”Investigation of dipole and quadrupole excitations near the neutron threshold in the doubly magic nucleus ^{208}Pb with the resonant photon scattering at the S-DALINAC”
2002 – 2005	Stipendiatin an der Technische Universität Darmstadt nach dem Hessischen Gesetz zur Förderung von Nachwuchswissenschaftlern
Seit 2005	Stipendiatin des Graduiertenkollegs ”Physik und Technik von Beschleunigern” an der Technische Universität Darmstadt

Erklärung:

Hiermit erkläre ich, dass ich die vorliegende Dissertation selbständig verfasst, keine anderen als die angegebenen Hilfsmittel verwendet und bisher noch keinen Promotionsversuch unternommen habe.

Darmstadt, im Juli 2006